2-1-2013

Particle-Collector Interactions In Nanoscale Heterogeneous Systems

Marina Bendersky
University of Massachusetts - Amherst, marina.bendersky@gmail.com

PARTICLE-COLLECTOR INTERACTIONS IN NANOSCALE HETEROGENEOUS SYSTEMS

A Dissertation Presented

by

MARINA BENDERSKY

Submitted to the Graduate School of the
University of Massachusetts Amherst in partial fulfillment
of the requirements for the degree of

DOCTOR OF PHILOSOPHY

FEBRUARY 2013

Chemical Engineering

PARTICLE-COLLECTOR INTERACTIONS IN NANOSCALE HETEROGENEOUS SYSTEMS

A Dissertation Presented

by

MARINA BENDERSKY

Approved as to style and content by:

Jeffrey M. Davis, Chair

Maria M. Santore, Member

David M. Ford, Member

T. J. Mountziaris, Department Chair
Chemical Engineering

To the memory of my grandfather Máximo Saúl Viner

ACKNOWLEDGMENTS

I thank my adviser, Prof. Jeffrey M. Davis, for his advice and help toward the completion of this work. I am grateful for his guidance and fruitful discussions that provided me with knowledge, which will hopefully be reflected in my future endeavors. I would also like to express my gratitude to Prof. Maria M. Santore, for teaching me about important experimental aspects of the current work, which led me to improve my computational results. I am also thankful for her wise and helpful parenting advice. I thank Prof. David M. Ford for his support, guidance and help, and for his insightful comments regarding this work.

I also sincerely thank my friends, with whom I shared memorable experiences in my *dear* Buenos Aires, in Israel and in Amherst, MA. I am especially grateful to my parents-in-law, Lora and Yakov, to my parents, Evelina and Mario, and my best friends: my brother Ale, and my sisters, Lau and Marce. Despite the physical distances, they are all right here, and I am truly thankful for that. And last but not least, I thank my husband Michael and my children, Sophie and her sibling underway. Without Mike's love, support, encouragement, patience, and wise advice, I would not have been able to complete this work. To Sophie and baby underway, I am thankful for the smiles, laughs, and joy they bring, and will bring, to our lives, and for teaching us that love is infinite.

ABSTRACT

PARTICLE-COLLECTOR INTERACTIONS IN NANOSCALE HETEROGENEOUS SYSTEMS

FEBRUARY 2013

MARINA BENDERSKY

B.Sc., TECHNION, ISRAEL INSTITUTE OF TECHNOLOGY

Ph.D., UNIVERSITY OF MASSACHUSETTS AMHERST

Directed by: Professor Jeffrey M. Davis

Particle-surface interactions govern a myriad of interface phenomena, that span from technological applications to naturally occurring biological processes.

In the present work, particle-collector DLVO interactions are computed with the grid-surface integration (GSI) technique, previously applied to the computation of particle colloidal interactions with anionic surfaces patterned with O(10 nm) cationic patches. The applicability of the GSI technique is extended to account for interactions with collectors covered with topographical and chemical nanoscale heterogeneity. Surface roughness is shown to have a significant role in the decrease of the energy barriers, in accordance with experimental deposition rates that are higher than those predicted by the DLVO theory for smooth surfaces. An energy- and force-averaging technique is presented as a reformulation of the GSI technique, to compute the mean particle interactions with random heterogeneous collectors. A statistical model based

on the averaging technique is also developed, to predict the variance of the interactions and the particle adhesion thresholds. An excellent agreement is shown between the models' predictions and results obtained from GSI calculations for large number of random heterogeneous collectors.

Brownian motion effects for particle-collector systems governed by nanoscale heterogeneity are analyzed by introducing stochastic Brownian displacements in particle trajectory equations. It is shown that for the systems under consideration and particle sizes usually used in experiments, it is reasonable to neglect the effects of Brownian motion entirely. Computation of appropriately defined Péclet numbers that quantify the relative importance of shear, colloidal and Brownian forces validate that conclusion.

An algorithm for the discretization of spherical surfaces into small equal-area elements is implemented in conjunction with the GSI technique and mobility matrix calculations of particle velocities, to obtain interactions and dynamic behaviors of patchy particles in the vicinity of uniform flat collectors. The patchy particle and patchy collector systems are compared in detail, through the computation of statistical measures that include adhesion probabilities and maximum residence times per patch. The lessened tendency of the patchy particle to adhere on the uniform collector is attributed to a larger maximum residence time per patch, which precludes interactions with multiple surface nano-features at a given simulated time.

Also briefly described are directions for future work, that involve the modeling of two heterogeneous surfaces, and of surfaces covered with many types of heterogeneity, such as patches, pillars and spring-like structures that resemble polymer brushes or cellular receptors.

TABLE OF CONTENTS

LIST OF TABLES

Table **Page**

LIST OF FIGURES

Figure **Page**

CHAPTER 1

INTRODUCTION

1.1 Motivation.

Among myriad physical and biological phenomena controlled by interactions between particles and macroscopically planar surfaces with nanoscale heterogeneity are colloidal adsorption,[7,59,88,110,118] separation and filtration,[15,107] coating and cleaning applications,[96,97] and the receptor-mediated adhesion and rolling of neutrophils on ligand-coated surfaces.[57] Surfaces patterned with pillars have recently been shown to control frictional adhesion in some biomimetic systems.[124] Furthermore, mechanisms that are governed by the recognition of surface features, which can be analyzed with measurements of surface-particle forces[36,76] or from deposition morphologies on heterogeneous surfaces,[2,9] underly the development of "lock and key" colloidal applications[19,77] that enable sensors at the nano- and micro-scales.

Colloidal interactions between spherical particles and patterned, planar surfaces with spatially varying charge have been studied extensively.[38,39,73,107] Particle deposition onto unfavorable collectors was predicted to increase significantly if the patches for favorable deposition are large, such that a particle interacts with only one patch on the collector surface.[107] In recent studies with nanoscale patches, which are orders of magnitude smaller than the depositing particles, it was also revealed that small amounts of randomly-distributed, attractive patches induce particle deposition onto net-repulsive surfaces.[37–39,71,81,103] The particle capture in this latter system is due to the interaction of a particle with many patches, the nonuniform distribution of which creates locally-attractive regions on the surface.[4,6,8,64,98,104]

The systems modeled throughout this work are inspired by experimental studies of colloidal silica particles that deposit on planar surfaces patterned with nanoscale heterogeneities. In experiments performed by Santore and Kozlova,[81,103] uniformly and negatively charged 460-nm diameter silica particles flowed in solution over planar negatively charged silica surfaces patterned with positively charged round patches. The planar surfaces are acid-washed microscope slides covered by controlled amounts of the cationic polyelectrolyte pDMAEMA (poly-dimethyl-aminoethyl methacrylate). The round 11-nm diameter pDMAEMA patches are relatively flat, and protrude over the surface only about 1 nm. Due to the shear flow (at rates varying from 10 to 50 sec^{-1}), the patches are randomly and irreversibly deposited on the surface. Varying patch densities are obtained by allowing the pDMAEMA solution to flow over the negatively charged surface for different periods of time. The pDMAEMA patches resist desorption and self-exchange with other pDMAEMA chains, and, most importantly, they remain adhered on the surface even while exposed to flowing silica particles. TIRF (total internal reflectance fluorescence) was used to measure the deposition of the fluorescent-core silica particles on the charge heterogeneous surface. Particle deposition was found to be controlled by the spacing between the positive patches. For surfaces densely covered by patches (small patch-patch spacing), adhesion is rapid and transport-limited. For larger patch-patch spacing, however, adhesion rates become slower and the amount of deposited particles also decreases. A critical patch-patch spacing above which silica particles do not adhere on the surface constitutes an adhesion threshold.

The existence of an adhesion threshold indicates that more than one surface heterogeneity (patch) is needed to capture a flowing silica sphere, thus suggesting that particles adhere on the surface due to the concerted action of many patches located within a specified area on the collector's surface. A "zone of influence" (ZOI)[81,103] on the planar collector is thus defined as the area for which the interaction per unit

area with the particle is significant. Assuming the overall interactions are dominated by the electrostatic double layer repulsions, the geometry of the ZOI depends on the Debye length and the particle size. A shell of one Debye length width around each of the interacting surfaces is chosen to define the spatial extent of the zone of influence. The radius of the zone of influence R_{ZOI} is indeed obtained from the right triangle that results from the intersection of the particle's and collector's one Debye length shells when the particle is in contact with the collector. As shown schematically in Fig. 1.1,

$$R_{ZOI}^2 = (a + \kappa^{-1})^2 - (a - \kappa^{-1})^2 = 4\kappa^{-1}a \quad \text{and} \quad R_{ZOI} = 2\sqrt{a\kappa^{-1}} \; .$$

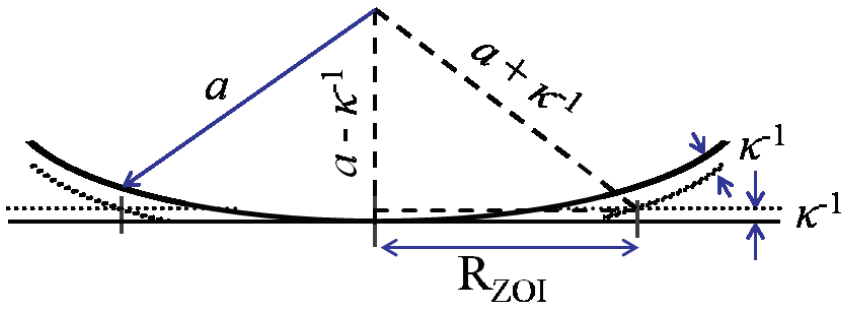

Figure 1.1. Schematic diagram of the particle-surface interface. The radius of the zone of influence is defined by the right triangle obtained by the intersection of one Debye length width shells surrounding the particle's and collector's surfaces.

The particle size (or curvature) and the Debye length are therefore combined into one single length scale that accurately describes the effects of surface heterogeneities on the overall character of the interactions. The spatial fluctuations of surface heterogeneities within the ZOI are thus of crucial importance to particle deposition and the corresponding adhesion thresholds.

The random distribution of adhesive patches on a collecting surface, that is also covered by poly(ethylene glycol) (PEG) brushes, is shown in Fig. 1.2 [52] by the similarities between a micrograph of roughly 500 PLL/μm^2 where about 1500 illuminated spots correspond to a trace amount of the PLL fluorescently labeled, and a MATLAB generated image of 1500 points randomly distributed throughout an area of the same size. It is the random distribution of nano-features on the collector that will determine the adhesive character of the particle (or protein)-collector interactions.

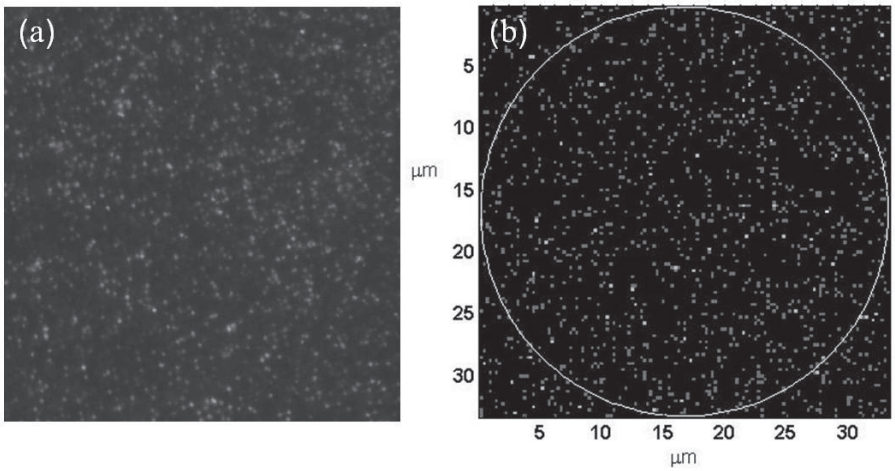

Figure 1.2. (a) Micrograph (33 x 33 μm^2) of roughly 500 PLL/μm^2. Approximately 1500 illuminated spots correspond to a trace amount of PLL fluorescently labeled.[52] (b) MATLAB generated image of 1500 points randomly distributed on an area of the same size.[52]

Computationally efficient models that can accurately predict the behavior of systems comprising heterogeneous particles and surfaces can effectively aid in experimental design. By providing insights that contribute to the understanding of the experimental findings, theoretical calculations reduce the number of parameters that would need to be empirically probed, in order to obtain, for instance, a desired (adhesive or non-adhesive) behavior. Accurate theoretical analysis can also provide insight on the forces and mechanisms that determine the specific adhesive and deposition behaviors of heterogeneous particle-collector experimental systems. The present study

is thus motivated by the need for computationally efficient modeling and simulation tools that will contribute not only to the efficient development of experimental set-ups specifically tailored for desired applications, but also shed some light on the physics underlying particle-heterogeneous collectors interactions.

Particle-surface interactions have been the subject of extensive theoretical and computational studies, which almost exclusively rely on the Derjaguin-Landau-Verwey-Overbeek (DLVO) theory of colloid stability. Within the framework of the DLVO theory, the total particle-surface interaction results from the assumed additive effects of attractive van der Waals (vdW) and repulsive Electrostatic Double Layer (EDL) interactions. Significant discrepancies between DLVO theoretical predictions and experimental findings, for example, in particle deposition studies, suggested that other types of colloidal interactions or interacting surfaces' roughness should be added to the computations, thus giving rise to the so-called "X-DLVO" models.[20,59,60]

Perhaps, the most computationally challenging component of DLVO interactions is the computation of the electrostatic surface potentials required in calculations of EDL forces and energies. Surface potentials are given by the Poisson-Boltzmann equation, the non-linearity of which does not allow for a straightforward, analytical solution. Numerous numerical techniques,[47,55,62,63] such as multi-grid and nonlinear conjugate gradient methods, have been developed and applied to the solution of the nonlinear form of the Poisson-Boltzmann equation. The solution domains are usually restricted to a box or a cell, such that the numerical solutions are only relevant for systems with membrane-like geometries.[47]

Accurate predictions of a particle's trajectory as it translates over a collecting surface requires, at every simulated time step, the computation of DLVO forces, which in turn determine the particle's location at the next simulated time step. The numerical solution of the nonlinear form (or even of the linear form) of the Poisson-Boltzmann equation at every time step would be extremely challenging not only

due to the complexity of the particle-surface system configuration but also in terms of computational costs. Simple analytical and approximate techniques, such as the Derjaguin integration method and the linear superposition approximation, make use of the linear form of the Poisson-Boltzmann equation and yield accurate predictions of colloidal interactions for simple system geometries. The validity of these approximate methods, however, is unfortunately limited to small particle-surface separations or large Debye lengths.

The development of the surface-element integration (SEI) technique constitutes a significant improvement over Derjaguin's integration method and the linear superposition approximation. The SEI technique yields accurate values of the colloidal forces and energies of interactions for sphere-plate system configurations and is not restricted with respect to particle-surface separation distances nor Debye lengths. The SEI technique requires, however, the numerical integration of colloidal energies or forces over the entire particle's surface or volume. The applicability of the SEI technique to the computation of particle trajectories thus presents, in practice, computational constraints that are similar to those imposed by the numerical solution of the Poisson-Boltzmann equation. Moreover, it is not clear how the SEI method could be modified in order to account for small chemical and topographical heterogeneities on the colloidal particle's surface, since an analytical expression that defines the particle's geometry is used to simplify the numerical integrations.

The grid-surface integration (GSI) technique, recently developed by Duffadar and Davis,[38,39] is a numerical method for computing particle-surface colloidal interactions that is based on the SEI technique but does not require numerical integrations nor the definition of the particle geometry by an analytical expression. The GSI technique involves the discretization of both the particle surface and the heterogeneous (planar) wall, and the total interaction (energy or force) between the particle and

the heterogeneous surface is obtained by summing the interactions for each pair of discrete areal elements.

Computations of many particle trajectories can ultimately lead to the prediction of particle adhesion thresholds and particle deposition behaviors, and thus define distinct regions in parameter space that distinguish between firm, no adhesion, and skipping and rolling motion regimes.

Most theoretical studies on colloid deposition on homogeneous and heterogeneous surfaces involve the formulation and numerical solution of rigorous transport equations,[1,70,106] resulting in model predictions that can be either limited by the validity of simplifying assumptions[1] or dependent on experimentally determined parameters.[70]

Estimates of particle deposition rates on heterogeneous surfaces based on a linear patch-wise model[70,107] are accurate for macroscopic patches because the patches are much larger than the depositing colloidal particles, and interactions between patch boundaries are negligible. For surface heterogeneities much smaller than the colloidal particles, however, the predictions of the patchwise model do not agree with experimentally determined deposition rates.[40]

Deposition kinetics and jamming concentrations of hard spheres adsorbing on striped surfaces and surfaces covered by smaller spherical asperities that behave as adhesion sites have been computed with random sequential adsorption (RSA) simulations.[2,3,6] Particle deposition modeled with RSA simulations do not include the effects of DLVO interactions, but instead depend on a series of attempts in which locations on the heterogeneous surface are randomly chosen. A particle will be considered to be irreversibly adhered at a specific location if an unoccupied adhesion site is present at such location, and if the additional particle would not overlap with previously adhered ones. The particles adhere with unity probability after an available adsorption site is selected, and a new adhesion trial, uncorrelated with previous ones, is attempted when deposition is not geometrically possible. The sequential adsorp-

tion attempts continue until the jamming state is reached. Adsorption probabilities predicted by RSA simulations, therefore, are mainly dependent on geometrical system parameters, such as the particle to adsorption site ratio, and do not account for particle flow effects nor colloidal interactions.

For the particle-collector nanoscale heterogeneous systems under consideration, Brownian motion effects have been typically neglected in previous computational studies.[37–39] The displacements of free particles due to Brownian motion, however, are often significant in time intervals characteristic of the imposed flow, and Brownian motion can enable particle deposition on both homogeneous and heterogeneous collecting surfaces, even in the presence of an energy barrier.[2,118]

While adhesive dynamic simulations[91] showed that bond dissociation dynamics are not significantly influenced by Brownian forces and recent studies on particle interactions with rough collectors[74] also indicated that Brownian motion effects are negligible, microchannel flow experiments of particle deposition[114] suggest that, for low-energy barrier systems, Brownian motion can indeed increase particles' tendency to adhere on heterogeneous collectors.

Previous work focused on the study of the dynamics and aggregate formation properties of many-particle systems,[12,44] on particle deposition on homogeneous collectors[74] or on particle behavior in parallel-plate microchannel flow.[114] A detailed study of Brownian motion effects on particle interactions with collectors covered with flat or protruding nano-features is, however, lacking.

Interest in the study of interactions of anisotropic particles has grown significantly, leading to the recent development of innovative particle synthesis techniques used to engineer nano- and colloidal particles with multiple surface features. "Patchy particles", as defined by Zhang and Glotzer,[127] are particles that exhibit strong directional interactions induced by distinct patches on the particle's surface. Highly anisotropic interactions between patchy particles and/or surfaces patterned with ef-

fectively "attractive" and "repulsive" interaction sites can lead to the assembly of otherwise neutral or repulsive surfaces into ordered arrays.

Anisotropic particles at the nano and colloidal scales of diverse shapes, sizes and electronic and optical properties were synthesized with chemical, physical and biologically-inspired ingenious techniques.[25,48,58,68,95,109] These patchy particles can be used as building blocks of target structures that can, in turn, be assembled in multiple emerging technologies, such as photonic crystals, sensors, and electronic, molecular imaging and drug-delivery devices.[11,28,95,123]

From the theoretical perspective, patchy particles were first classified by Glotzer and Solomon,[48] who developed a unifying framework to describe the classes of patchy particles already synthesized. In many recent computational studies, patchy particles are modeled as units composed of distinct "atoms", and specific attributes are assigned to each atom, depending on whether it belongs to the 'patch' or 'core' surface areas of the particle. The self assembly of ordered periodic structures is also predicted by Brownian dynamics simulations[65] and molecular dynamic computations that predict the assembly of nanoparticles and polyelectrolytes into charged, patchy colloids.[84]

While theoretical work on patchy particle interactions at the molecular scale is frequently found in the literature, only a handful of studies describe colloidal interactions of heterogeneous particles in close contact to a wall and the effects of such heterogeneities on particle deposition. Sphere-plate and sphere-sphere DLVO interactions for spheres patterned with topographical heterogeneity were computed numerically[18,108] and analytically,[110] and model predictions were found to agree with experimental measurements.[111] Spherical chemical heterogeneity, however, was not included. A recent study by Chatterjee et. al.[29] is focused on the deposition of micro-scale particles onto larger Janus and patchy spherical collectors. Chemical heterogeneity is modeled by patterning defined regions of the spherical collector with

adhesion-favorable and adhesion-unfavorable surface properties. The patterned areas of the spherical collectors were larger than the depositing colloidal particles.

The effect of nanoscale heterogeneity that patterns spherical particles and interactions between such heterogeneous particles and collectors has not been studied, however, in previous work. The study of patchy particles as depositing agents, in contrast to their behavior as collecting surfaces,[29] can aid toward the understanding of the physical processes that underlie a myriad of "smart" devices, and possibly further advance the development of computational and simulation techniques that can accurately model such processes.

1.2 Objectives and Outline.

A computational study of particle-surface interactions with nanoscale heterogeneity is presented in the pages that follow, to ultimately gain insight into the adhesive and dynamic system behaviors that bear importance from theoretical and practical perspectives.

Results presented throughout this work aim to:

- Investigate the effects of topographical heterogeneity on the system's energy-distance profile to elucidate possible reasons for discrepancies found between experimental and theoretical experimental rates.

- Develop further existing computational techniques to incorporate topographical and chemical heterogeneities, that have not been accounted for jointly in previous work, though their presence is ubiquitous in experimental systems

- Develop simple and computationally inexpensive models, not found in the literature, to predict mean and variance of interactions and adhesion thresholds for system configurations with collectors that are randomly patterned at the nanoscale.

- Analyze in detail the effects of Brownian motion on the behavior of particle-collector nanoscale heterogeneous systems, to verify the assumption found in the literature that such effects can be entirely neglected.

- Develop a new computational technique to simulate interactions of patchy particles that could be fabricated, for instance, by coating silica spheres with cationic patches or polymer brushes, and that could model cells covered with receptors.

- Establish the basis of a novel approach that allows for the modeling of interactions between heterogeneous particles and surfaces, to significantly increase the resemblance between simulated and real surfaces and to possibly model a number of physical processes that underlie surface scribing, cleaning, filtration, "lock and key", and protein recognition applications, among others.

Theoretical background that defines fundamental concepts and computational techniques developed in previous work, some of which are implemented to obtain the results presented in this work are described in Chap. 2. In Chap. 3, interactions between uniform spheres and heterogeneous collectors are studied in detail. Collector topography effects on particle adhesion are evaluated in Sec. 3.1. A force- and energy-averaging technique that predicts mean interactions for the systems considered is also developed. In Sec. 3.2, a statistical model based on the averaging technique is formulated as a computationally efficient tool that predicts variance of interactions and particle adhesion thresholds. The specific effects of Brownian motion in the dynamics of the heterogeneous systems considered are studied in Sec. 3.3 by introducing stochastic Brownian displacements in particle trajectory equations. Péclet numbers that quantify shear, Brownian and colloidal forces are also defined. In Chap. 4, the (patchy particle)-(collector) system is thoroughly characterized in terms of adhesion thresholds, spatial variations in the trajectories, and maximum residence times per patch. Detailed comparisons with the extensively studied (particle)-(patchy collec-

tor) system are also presented. In Chap. 5, the main findings and conclusions are summarized, and a number of possible directions for future work are delineated.

CHAPTER 2

BACKGROUND

2.1 The Gouy-Chapman double-layer model.

The surface charge of a particle in an electrolyte solution is balanced by oppositely charged counterions, such that the solution is electrically neutral. The counterion distribution is not uniform, since counterions tend to concentrate close to the particle surface due to electrostatic attractions but also diffuse randomly in the solution under the action of thermal forces. The region that contains the surface charge, referred to as the compact or Stern layer, and the region where the ions move freely due to their thermal energy, termed the diffuse layer, comprise the electric double layer. The nature and concentration of the salts in solution determine the surface charge and counterion distributions.[41,100]

Within the Gouy-Chapman model[27,54] of the diffuse layer that surrounds a charged particle, the interface is flat, infinite and impenetrable, the ions are point charges, and the solvent's properties (such as permittivity) do not depend on the distance from the surface.[100] It is also assumed that the surface charge and potential are uniformly distributed over the surface. Indeed, many surfaces can be considered as having an effectively uniform surface charge density because the rate of ions exchange between surface sites and the adjacent solution is faster than the rate of approach of colloidal particles toward the interface.[41,100]

The relationship between charge density, ρ (C/m^3), and potential, ψ(V), at any point in the solution is described by the Poisson equation,[41]

$$\nabla^2\psi = -\frac{\rho}{\epsilon}\,, \tag{2.1}$$

where ϵ is the absolute permittivity of the medium ($\mathrm{C^2/N\,m^2}$). The Poisson equation is accurate for electrolyte concentrations lower than 1 M and surface potentials less than 200 mV.[100]

The ions in the diffuse layer are in equilibrium, so the force, which is given by the gradient of the electrochemical potential,[100] must be zero, or,

$$k_\mathrm{B}T\nabla n_i + ez_i\nabla\psi = 0\,, \tag{2.2}$$

where k_B is the Boltzmann constant, T is the absolute temperature, n_i and z_i are the concentration and valence of ion i, respectively, and e is the fundamental electric charge, 1.6×10^{-19} C.

From Eq. (2.2), it is seen that the ions in solution follow a Boltzmann distribution,

$$n_i = n_{i\,0}\exp\left(-\frac{z_i e\psi}{k_\mathrm{B}T}\right) \tag{2.3}$$

where n_i denotes the number concentration of ion i at a point in the solution where the potential is ψ and $n_{i\,0}$ stands for the concentration in the bulk (where $\psi = 0$).

For symmetrical $(z-z)$ electrolytes, the charge density is given by:[41]

$$\rho = ze(n_+ - n_-) = -2zen_0\sinh\left(\frac{ze\psi}{k_\mathrm{B}T}\right) \tag{2.4}$$

where n_+ and n_- represent the concentrations of cations and anions and n_0 is the concentration of each ion in the bulk solution. In Eq. (2.4), z is the valence of the ions and does not include the charge sign.

The variation of the potential normal to a flat interface can be obtained by combining the one dimensional form of Eq. (2.1) with Eq. (2.4), to obtain the Poisson-Boltzmann equation,[41]

$$\frac{d^2\psi}{dx^2} = \frac{2zen_0}{\epsilon}\sinh\left(\frac{ze\psi}{k_{\mathrm{B}}T}\right) . \tag{2.5}$$

By introducing the dimensionless parameters $\Psi = ze\psi/k_{\mathrm{B}}T$ and $\kappa^2 = 2e^2n_0z^2/\epsilon k_{\mathrm{B}}T$ (for $z-z$ electrolytes), the Poisson-Boltzmann equation is simplified to

$$\frac{d^2\Psi}{dx^2} = \kappa^2\sinh\Psi\,, \tag{2.6}$$

where κ is the Debye-Hückel parameter, and has units of inverse length.

Applying the Debye-Hückel approximation, a linear form of the Poisson-Boltzmann equation can be obtained for low surface potentials (ψ less than about 25 mV in 1-1 electrolytes) by assuming $\sinh\psi \simeq \psi$, so that Eq. (2.6) can be further simplified to

$$\frac{d^2\Psi}{dx^2} = \kappa^2\,\Psi\,. \tag{2.7}$$

The solution of Eq. (2.7),

$$\Psi = \Psi_s\exp(-\kappa x), \tag{2.8}$$

where Ψ_s is the potential at the interface, reveals the exponential decay of the potential with increasing distance from the charged interface. For example, at a distance $1/\kappa$ from the surface, the potential decreases to 1/e of the surface potential. The Debye-Hückel parameter is thus also referred to as the Debye-Hückel length since it determines the thickness of the diffuse layer. In the general case of electrolyte solutions of different ions, κ is defined as

$$\kappa = \sqrt{\frac{e^2\sum n_{i0}z_i^2}{\epsilon k_{\mathrm{B}}T}}\,, \tag{2.9}$$

where the sum applies to all the ions in the solution.

2.2 Electrostatic double-layer interactions.

When two charged particles approach each other, their double-layers overlap and give rise to *double-layer interactions*. These interactions can either be repulsive or attractive, depending on whether the approaching particles bear charges with the same or opposite sign, respectively.[41]

Verwey and Overbeek[117] distinguished between interactions at *constant surface potential* and interactions at *constant surface charge*. As the particles come closer to each other, the double layer charge at the particles surfaces decreases and therefore some ions diffuse into the solution in order to maintain the thermodynamic equilibrium in the double layer. The Brownian motion of the relatively heavy colloidal particles as they approach each other is in general much slower than the thermal diffusion of the ions. The particles surface charge is thus adjusted rapidly, to maintain the thermodynamic equilibrium, and the surface potential is assumed to remain constant. For some systems, however, the transport of ions from the particle surface to the solution, and vice versa, is not a fast process since it is controlled by the presence of an energy barrier. In this case, the particles surface charge is adjusted slowly enough such that it can be assumed to remain constant. Unless otherwise indicated, the assumption of constant surface potential will be the assumption of choice in the computations presented within this work.[117]

The double layer interaction energy between two approaching surfaces can be found by solving the Poisson-Boltzmann equation (Eq. (2.6)) for the system of interest. Simple, analytical expressions cannot be usually obtained, however, by directly solving that equation. Alternatively, an expression for the energy of interaction for a given system can be constructed from expressions for each of the system surfaces in isolation. In this way, accurate approximations can be derived.[41]

A compromise between the Constant surface Potential Approximation (CPA) and Constant surface Charge Approximation (CCA) is given by the Linear Superposition

Approximation (LSA). Within the LSA, a region exists between the interacting surfaces where the potential is small and obeys the linear Poisson-Boltzmann equation (LPB, Eq. (2.7)). The total interaction is obtained by summing the contribution of each interacting surface. The LSA is found to be an accurate approximation only if the particles' separation distance (h) is large ($\kappa h \gg 1$).

2.2.1 Plate-plate interactions.

For symmetrical (z-z) electrolytes, a number of expressions for the energy of interaction between two infinite parallel flat plates have been derived by integrating the pressure (force per unit area) between two flat double layers over the distance between the plates. Approximate expressions can be obtained by using this integration method under various assumptions (CPA, CCA, and/or LSA). A comprehensive list of the numerous expressions is presented by Elimelech et al.[41]

In the present work, the electrostatic double-layer (EDL) interactions are computed on the basis of the exact, analytical expression derived by Hogg et al.[61] by solving the LPB equation (Eq. (2.7)) for the case of constant surface potential boundary conditions. The two dissimilar plates are separated by a distance h and charged with small potentials ($\psi < 25\,\mathrm{mV}$). The bottom plate (for which $x = 0$) is charged with a potential $\psi_{p,1}$, while the potential of the top plate (located at $x = h$) is denoted by $\psi_{p,2}$. The solution to Eq. (2.7) with these boundary conditions yields the dependence of the potential between the plates on the distance from the bottom plate,

$$\psi = \psi_{p,1}\cosh(\kappa x) + \left(\frac{\psi_{p,2} - \psi_{p,1}\cosh(\kappa h)}{\sinh(\kappa h)}\right)\sinh(\kappa x)\,. \tag{2.10}$$

The potential energy of interaction (U_{EDL}) is found from the change in free energy of the system caused by bringing the plates together from infinity,[61] that is,

$$U_{\mathrm{EDL}} = \Delta G = G_{\mathrm{h}} - G_{\infty}\,. \tag{2.11}$$

As shown by Verwey and Overbeek,[117] the free energy of a single double layer for the case of small and constant surface potential ψ_p can be computed from

$$G = -\frac{1}{2}\sigma\psi_p\,, \tag{2.12}$$

where σ (C/m^2) is the surface charge density. The total free energy of the system is obtained by adding the free energies of the separate double layers,

$$G_{\rm h} = -\frac{1}{2}(\sigma_1\psi_{p,1} + \sigma_2\psi_{p,2})\,, \tag{2.13}$$

where $\sigma_1\,, \sigma_2$ are the surface charge densities corresponding to each of the double layers.

The dependence of the surface charge density on the surface potential for a plate-plate system configuration is determined from[117]

$$\sigma = -\epsilon\left(\frac{d\psi}{dx}\right)\Big|_{x=0}\,, \tag{2.14}$$

such that

$$\sigma_1 = -\epsilon\kappa\left[\psi_{p,2}\,\mathrm{cosech}(\kappa h) - \psi_{p,1}\coth(\kappa h)\right] \tag{2.15}$$

and

$$\sigma_2 = \epsilon\kappa\left[\psi_{p,2}\coth(\kappa h) - \psi_{p,1}\,\mathrm{cosech}(\kappa h)\right], \tag{2.16}$$

where ϵ (C^2/N m^2) is the absolute permittivity of the medium. The free energy of the double layer system can thus be obtained by inserting Eqs. (2.15)-(2.16) in Eq. (2.13), to obtain

$$G_{\rm h} = \frac{\epsilon\kappa}{2}[2\,\psi_{p,1}\,\psi_{p,2}\,\mathrm{cosech}(\kappa h) - (\psi_{p,1}^2 + \psi_{p,2}^2)\coth(\kappa h)]\,. \tag{2.17}$$

For large separation distances, $\mathrm{cosech}(\kappa h) \to 0$ and $\coth(\kappa h) \to 1$ such that the free energy is given by

$$G_\infty = -\frac{\epsilon\kappa}{2}(\psi_{p,1}^2 + \psi_{p,2}^2)\,. \tag{2.18}$$

Finally, the total energy of interaction per unit area between two infinite, parallel, flat double layers is obtained by substituting Eqs. (2.17) and (2.18) in Eq. (2.11); namely,

$$U_{\mathrm{EDL}}^{\mathrm{A}} = \frac{\epsilon\kappa}{2}\left[(\psi_{p,1}^2 + \psi_{p,2}^2)(1 - \coth(\kappa h)) + 2\,\psi_{p,1}\,\psi_{p,2}\,\mathrm{cosech}(\kappa h)\right]\,. \tag{2.19}$$

Eq. (2.19) is an analytical, exact solution of the LPB equation for the case of two infinite, parallel, flat plates, and will be used extensively throughout this work.

As shown, Eq. (2.19) is derived from the solution of the LPB equation under the assumption of constant potential boundary conditions. It is noted that the assumption of constant surface charge could undermine the validity of the LPB equation which is accurate only for small surface potentials. When the separation distance between two surfaces at constant charge decreases, the surface potentials will increase, and possibly become large enough ($\psi > 25\,\mathrm{mV}$) so that the LPB is no longer valid for small separations. Constant potential boundary conditions, however, allow the use of the LPB equation for the whole range of particle-surface separations, as long as the potentials are relatively small.

2.2.2 Sphere-sphere interactions.

The dependence of the surface potential around a sphere on the distance from its center can be found by solving the Poisson-Boltzmann equation, expressed in spherical coordinates. Due to the particle's curvature, however, an analytical solution does not exist, and instead, the sphere's surface potential is obtained from numerical or asymptotic solutions that usually depend on the specific system of interest.[100] It is

expected, therefore, that the two-sphere problem will lack closed-form solutions and rely on approximating assumptions.

Many double layer interactions expressions for the sphere-sphere system result from solving either the linear or the non-linear form of the Poisson-Boltzmann equation with the aid of the Derjaguin approximation (discussed in detail in Sec. 2.5) and in combination with either the constant charge (CCA) or constant surface potential (CPA) assumptions. A few expressions were derived, however, by implementing an integral approach for the distribution of electric dipoles or on the basis of the LSA.

McCartney and Levine[90] solved the LPB equation for a system composed of two identical spheres, by expressing the potentials in terms of the surface distribution of electric dipoles.[13,90] This method yields accurate results for $\kappa a \geq 5$, where a is the spheres' radius, and predicts the correct dependence of the potential on the distance for large sphere-sphere separation distances. Even though this technique represents an improvement over the results predicted with the Derjaguin approximation, the integral equation that governs the distribution of the electrical dipoles cannot be easily modified to obtain higher approximations nor extended to analytically solve the non-linear Poisson-Boltzmann equation for higher potentials.

The McCartney-Levine model is extended by Bell et al.[13] for the case of unequal spheres charged with small, dissimilar potentials, for large values of κa_1, κa_2, where a_1 and a_2 denote the particle radii. A solution for the case of larger potentials is also presented, and found to be in agreement with numerical results for $\kappa a \sim 5$. Bell et al.[13] ultimately suggest that accurate force and energy predictions of the double layer interactions for the sphere-sphere system, for all separations and potentials, could be obtained by combining the LSA with the Derjaguin approximation, which yield correct results at large and small separation distances, respectively.

An expression derived by Bell et al.[13] on the basis of the LSA for the case of unequal spheres charged with dissimilar potentials can be extended, in principle, to

describe interactions between particles of arbitrary shape, size, potential (as long as they are uniform and constant), and electrolyte type. This method, however, makes use of the asymptotic form of the potential distribution at large separations in the diffuse layer. Even though the asymptotic form for a spherical particle is well known, it depends on a parameter that can be determined only numerically, thus precluding the extensive use of the LSA expression.

A comprehensive list of approximate expressions that describe electrostatic double layer interactions for the sphere-sphere system is presented by Elimelech et al.[41]

2.2.3 Sphere-plate interactions.

Expressions for the sphere-plate system can be obtained by modifying the sphere-sphere interactions obtained by applying different assumptions (LSA, CCA, CPA, Derjaguin approximation) and assuming the radius of one of the spheres tends to infinity.[41] Analytical expressions for sphere-plate interactions, that, in contrast, are not derived by modifying the sphere-sphere expressions, but instead make use of the plate-plate expressions, were recently derived.

Zypman[128] derived a closed-form, exact expression of the force for the sphere-plate system that depends on the energy per unit area between two flat plates. The force can be integrated analytically for the sphere-plate configuration to obtain the respective energy of interaction. Even though the expressions are valid for both van der Waals (vdW) and EDL interactions, they can only be analytically obtained for a few simple geometries. Moreover, the expressions obtained with this method are lengthy and cumbersome, such that their wide practical use is somewhat limited.

Another closed-form expression for sphere-plate double layer interactions was recently derived by Lin and Weisner.[85] By making use of the Derjaguin geometrical construction[34] (see Sec. 2.5), an expression for the sphere-plate EDL interaction energy is obtained by integrating the plate-plate interaction energy over the front and

back hemispheres of the particle. The method is applicable to the cases of constant surface potential, constant surface charge and to the intermediate case as defined by the LSA. The expressions derived by Lin and Weisner[85] are considered to be exact since they rely on exact plate-plate expressions. Their validity is therefore not restricted in terms of particle sizes and separation distances. It is not clear, however, whether such expressions are applicable to particle-collector systems with nanoscale heterogeneities or in systems that include particles lacking a spherical geometry.

2.3 van der Waals forces.

The London-van der Waals forces, or more simply, the van der Waals (vdW) forces, arise from spontaneous or permanent electric and magnetic polarizations of the interacting bodies. In Hamaker's microscopic approach,[56] the interaction between two macroscopic bodies can be obtained from the pairwise summation of all the intermolecular interactions between them. By integrating the energy per unit volume between two spherical particles over the particles' volumes, Hamaker[56] derived an expression for sphere-sphere van der Waals interactions that is dependent on the particle radii and on the separation distance only. In a similar fashion, relevant expressions are obtained for the sphere-plate and plate-plate system configurations.[56] In particular, the van der Waals interaction energy per unit area between two infinite and parallel flat plates is given by

$$U_{\mathrm{vdW}}^{\mathrm{A}} = -\frac{A_{\mathrm{H}}}{12\pi h^2}\,, \tag{2.20}$$

where h is the separation between the plates and A_{H} is the Hamaker constant, that depends on the particle and fluid properties and generally lies between $A_{\mathrm{H}} = 10 \times 10^{-21}$ J and $A_{\mathrm{H}} = 10 \times 10^{-19}$ J. Hamaker[56] showed that interactions between particles of the same material are always attractive, if the molecules of the fluid between the

particles do not present a marked orientation. The character of interactions between particles of different materials, however, can be either attractive or repulsive. Eq. (2.20) implies that the attraction between the interacting surfaces increases with decreasing separation distance, and it ultimately becomes infinite at the surfaces contact. In practice, the attraction remains finite at all separations because as the interacting surfaces come to a close approach, other forces arise, such as the Born repulsion.[41]

As mentioned, Hamaker's approach makes use of the additivity assumption, that can result in an overestimation of the interactions. Liftshitz[83] developed a new theory that does not require the use of such an assumption. Liftshitz's method, however, is difficult to implement due to the lack of experimental data on the particles and medium permittivities, in particular for system geometries other than the plate-plate configuration. Differences between the approaches were shown to be negligible and in practice, Hamaker's approach is often the method of choice. Hamaker's expressions are also improved by the addition of correction factors that account for retardation effects.[41,66]

Attractions are meaningfully reduced due to retardation effects when the separation distance between the interacting surfaces becomes comparable to the characteristic wavelength of $\lambda \simeq 100\,\mathrm{nm}$.[41] In the results presented throughout this work, the van der Waals interactions between two infinite parallel flat plates do not account for retardation effects, and are obtained from Eq. (2.20). The separation distances considered are much smaller than 100 nm, and moreover, at large separations the van der Waals interactions are weak, such that the inclusion of retardation effects becomes unnecessary.

2.4 The DLVO theory.

Derjaguin and Landau[35] and Verwey and Overbeek[117] developed independently a theory of colloid stability, presently widely known as the DLVO theory. According to this theory, van der Waals (vdW) attractions and electrostatic double layer (EDL) repulsions can be added to yield the total energy of interaction between particles and/or surfaces, as a function of the separation distance. The energy-distance profile usually shows an infinitely deep minimum (at small separations), a local maximum (the energy barrier), and another minimum (the secondary minimum, at larger separations). The specific shape of the energy-distance profile depends on interaction parameters (such as particle size, Debye length, zeta potentials and Hamaker constants) and, as will be shown, determines colloidal deposition.

It should be noted that an infinitely deep primary minimum is physically unrealistic. Therefore, for practical purposes, a finite potential at the primary minimum is often obtained by imposing an arbitrary distance of closest approach (of 0.1 - 0.2 nm),[41] or by explicitly adding short-range Born repulsions to the total energy of interaction. Other short-range effects,[41] such as ion hydration or surface roughness, limit the minimum separation distance and define an effective contact area, such that the surfaces are prevented from coming into physical contact.

While the DLVO theory successfully explains the stability of lyophobic colloids, for some systems discrepancies have been found between the theoretical predictions and experimental measurements of particle deposition, stability and adhesion. Experimental particle deposition rates are often found to be considerably larger than those predicted by the DLVO theory. The discrepancies between the theory and the experimental data are usually accounted for by adding "non-DLVO" forces to the van der Waals (vdW) attractions and the electrostatic double layer (EDL) repulsions, and the resulting model is usually termed the "extended-DLVO" or "X-DLVO" model.

Hoek and Agarwal[59] recently computed interactions between rough surfaces using an extended-DLVO model that included, in addition to vdW and EDL interactions, Lewis acid-base interactions, and steric and hydrodynamic forces. Surface roughness was indeed found to decrease the energy of interaction, and particle deposition on relatively repulsive surfaces was predicted due to the presence of locally attractive sites.

In aqueous systems, other attractive and repulsive forces could be responsible for the differences between experimental measurements and theoretical predictions. The hydration of ions at either interacting surface, for example, can introduce additional repulsive interactions, while hydrophobic effects increase the attraction between the surfaces.[41] As described in Sec. 5.2.1.2, the presence of adsorbed polymers can also affect the total interactions by either increasing the repulsions or the attractions, through steric interactions and polymer bridging, respectively.

2.5 The Derjaguin approximation.

Derjaguin[34] developed a technique that provides analytical expressions for the interactions between two curved surfaces, which are discretized into concentric rings of differential width. The total interaction is obtained by integrating the ring-ring interactions over the area of the curved surfaces in the vicinity of the region of closest approach. Assuming each ring can be treated as a flat plate, the ring-ring interactions are computed from the expressions derived for two infinite, parallel flat plates.[34,120] The Derjaguin approximation is also applicable to systems that include both curved and flat surfaces, such as the sphere-plate system.

The interaction energy predicted by Derjaguin's integration (DI) method can be generally expressed as

$$U_{DI} = f(a) \int_D^\infty U(h) dh \,, \tag{2.21}$$

where $f(a)$ is a geometric factor that represents the local curvature of the surface at the point of closest approach, D is the minimum separation distance between the interacting surfaces, $U(h)$ is the interaction energy, and h is the local separation distance between corresponding parallel flat rings. The geometric factor equals $f(a) = \frac{2\pi a_1 a_2}{(a_1+a_2)}$ for the case of two interacting spheres of radii a_1 and a_2, and $f(a) = 2\pi a$ for the sphere-plate system, where a represents the particle radius.

The Derjaguin approximation can be used to calculate both van der Waals and electrostatic double layer forces and energies. As shown by White,[120] it also provides a first order approximation for forces and torques in systems composed of particles with arbitrary curvature, such as cylinders and ellipsoids.

The Derjaguin method has, however, a number of limitations. The assumption that the flat rings can be treated as parallel flat plates is only valid when large particles interact at small separation distances ($h \ll a$),[41] such that curvature effects are minimal. The interacting double layers should be thin ($\kappa a \gg 1$), so that the gap between the interacting curved (convex) surfaces can be assumed to be one-dimensional, and the surface potentials are assumed to be small ($\psi < 25\,\mathrm{mV}$).

Despite these restrictions, the Derjaguin approximation predicts accurate results for $\kappa a > 10$, and even for $\kappa a > 5$.[117] Its use, however, is mostly limited to systems with large particles interacting at small separation distances. The surface-element integration (SEI)[17] technique, described in the following section, is presented as a more accurate and versatile alternative to Derjaguin's integration method.

2.6 The SEI technique.

Developed by Bhattacharjee and Elimelech,[17] the surface-element integration (SEI) technique is an integral method that allows for the computation of colloidal interactions between a sphere and an infinite flat plate.

The approaching particle is discretized into differential surface elements, whose projected area on the plane of the flat plate is denoted by dA. The total particle-plate interaction energy is calculated by numerically integrating the interaction energy per unit area between two infinite flat plates over the projected area of the spherical particle, *i.e.*,

$$dU_{SEI} = U(h)\, dA\,. \tag{2.22}$$

$U(h)$ is the interaction energy between two infinite parallel flat plates as a function of the local separation distance h. It should be noted that Eq. (2.22) represents the interaction between one surface areal element of the first surface (in this case, the particle) with the entire second surface (in this case, the planar plate). The SEI technique involves the discretization of only *one* of the interacting surfaces.

In order to simplify the integration of Eq. (2.22), the local separation distance h between any point on the particle and the planar surface is obtained from an analytical expression that defines the surface of the approaching particle.

Since EDL interactions are a surface phenomenon, the integral in Eq. (2.22) is performed over the particle's surface. Van der Waals interactions, however, arise from the particle's volume, so the corresponding integration, also given by Eq. (2.22), is performed over the particle's volume. The validity of the SEI technique thus follows from the equivalence between surface and volume integrals, as established by Gauss's divergence theorem.

The SEI technique can be applied to compute both long and short range interactions for spheres of arbitrary size and flat plates, at all separation distances. The thickness of the interacting double layers is not limited either, such that the SEI technique is clearly an improvement over the Derjaguin method. Some limitations to the SEI technique, however, do exist. The SEI method can be extended, in principle, to particles of arbitrary shape. An asymmetrical surface might not be defined, however, by a simple analytical expression, such that the integral in Eq. (2.22) could become

too complicated for practical purposes. Moreover, the implementation of the SEI technique to compute interactions of particles in shear flow is not straightforward. Each time step would require one or two numerical integrations, that would yield the instantaneous EDL and vdW forces, such that the application of the SEI method would become, in this case, computationally prohibitive.

2.7 The GSI technique.

The grid-surface integration (GSI) technique[14,38,39] is a method for computing colloidal interactions between a particle of arbitrary shape, size, and surface properties and a heterogeneously patterned surface and is based on the surface element integration (SEI) method. The GSI technique, however, involves the discretization of both the particle surface and the heterogeneous (planar) wall, such that the total interaction (energy or force) between the particle and the heterogeneous surface is obtained by summing the interactions for each pair of discrete areal elements. The sum of pairwise interactions is thus given by[38]

$$F = \sum_{\text{particle}} \sum_{\text{wall}} P(h)\ \boldsymbol{e}_1 \cdot \boldsymbol{e}_z\ dS, \tag{2.23}$$

where $P(h)$ is the force or energy of interaction per unit area between a particle's areal element (dA) and a corresponding element on the substrate (dS). The unit vector $\boldsymbol{e}_z$ specifies the direction normal to the surface, and the unit vector $\boldsymbol{e}_1$ indicates the direction between areal elements on the particle and the substrate (see Fig.3.1). The summations in Eq. (2.23) are performed over all of the discretized elements on the particle and collector.

The interactions between each pair of areal elements are determined from analytical expressions for colloidal energies or forces between parallel plates. The EDL and vdW interaction energies per unit area between two infinite, parallel flat plates are

obtained from Eqs. (2.19) and (2.20), respectively. Both the EDL and vdW forces between a particle and a heterogeneous surface are computed by incorporating the force per unit area,

$$F^A(h) = -\frac{\partial U^A(h)}{\partial h}, \tag{2.24}$$

in the GSI technique with $P(h) = F^A(h)$.

The accuracy and validity of the GSI technique was shown elsewhere,[38] by comparing interactions computed by implementing the GSI method with those obtained from numerical solutions of the LPB equation and from exact expressions derived for simple system geometries. The GSI technique can easily accommodate surface heterogeneities, that can be randomly located on either one or both of the interacting surfaces. Thus, unless otherwise specified, the GSI technique will be applied in all of the results that follow, to compute DLVO interaction energies and forces.

2.8 Hydrodynamic Interactions. The mobility matrix.

The dynamic profiles of the moving particles are obtained using the method of Duffadar and Davis[38] in which GSI computations of colloidal interactions are incorporated into a mobility tensor formulation of the hydrodynamics problem. Applying this formulation, the particle's translational velocity $\mathbf{V} \equiv (V_x\ V_y\ V_z)^t$ and rotational velocity $\mathbf{\Omega} \equiv (\Omega_x\ \Omega_y\ \Omega_z)^t$, in a cartesian coordinate system in which the y-axis is normal to the xz-plane, are obtained from

$$\begin{pmatrix} \mathbf{V} \\ \Omega \end{pmatrix} = \begin{pmatrix} \mathbf{M}_{VF} & \mathbf{M}_{\Omega F} \\ \mathbf{M}_{VT} & \mathbf{M}_{\Omega T} \end{pmatrix} \begin{pmatrix} \mathbf{F} \\ \mathbf{T} \end{pmatrix} \tag{2.25}$$

where $\mathbf{F} \equiv (F_x\ F_y\ F_z)^t$ and $\mathbf{T} \equiv (T_x\ T_y\ T_z)^t$ are the components of the externally applied forces and torques on the sphere due to the shear flow and colloidal interactions with the heterogeneous surface. The mobility matrix elements $M_{\mathrm{i,j}}$, composed of dimensionless functions that model the fluid's resistance to particle motion, are:[26,38]

1. $\mathbf{M}_{VF}$

$$M_{VF}^{11} = M_{VF}^{33} = T_r/6\pi\mu a D_f \tag{2.26}$$

$$M_{VF}^{22} = 1/6\pi\mu a\lambda \tag{2.27}$$

$$M_{VF}^{ij} = 0 \quad \text{for} \quad i \neq j \tag{2.28}$$

2. $\mathbf{M}_{\Omega F}$

$$M_{\Omega F}^{31} = -M_{\Omega F}^{13} = T_t/(6\pi\mu a^2 D_f) \tag{2.29}$$

$$M_{\Omega F}^{ij} = 0 \quad \text{for} \quad (i,j) \neq (1,3) \neq (3,1) \tag{2.30}$$

3. $\mathbf{M}_{VT}$

$$M_{VT}^{31} = -M_{VT}^{13} = -F_r/8\pi\mu a^2 D_f) \tag{2.31}$$

$$M_{VT}^{ij} = 0 \quad \text{for} \quad (i,j) \neq (1,3) \neq (3,1) \tag{2.32}$$

4. $\mathbf{M}_{\Omega T}$

$$M_{\Omega T}^{11} = M_{\Omega T}^{33} = F_t/8\pi\mu a^3 D_f \tag{2.33}$$

$$M_{\Omega T}^{22} = 1/8\pi\mu a^3\chi \tag{2.34}$$

$$M_{\Omega T}^{ij} = 0 \quad \text{for} \quad i \neq j\ , \tag{2.35}$$

where $D_f = T_t F_r - F_t T_r$. The function λ is given by Brenner[21]

$$\lambda = \frac{4}{3}\sinh\alpha \sum_{n=1}^{\infty} \frac{n(n+1)}{(2n-1)(2n+3)} \left[\frac{2\sinh[(2n+1)\alpha] + (2n+1)\sinh(2\alpha)}{4\sinh^2[(n+0.5)\alpha] - (2n+1)^2\sinh^2\alpha} - 1 \right]\ , \tag{2.36}$$

with $\alpha = \ln[(a+D)/a + (((a+D)/a)^2 - 1)^{1/2}]$, where a is the particle radius and D is the minimum particle-planar surface separation distance. For $D/a < 1 \times 10^{-5}$, the asymptotic expression is $\lambda \to a/D$.[26] The function χ is defined by Jeffrey,[69]

$$\chi = \frac{\sum_{n=1}^{\infty} \text{cosech}^3 n\alpha}{\text{cosech}^3 \alpha}\,, \tag{2.37}$$

for all α.

The hydrodynamic functions F_x^t, T_y^t, F_x^r and T_y^r depend on the particle size (a), the fluid viscosity (μ), and the particle-surface separation distance only. The minimum particle-surface separation distance is denoted by D, while the separation distance between the particle's center and the plane surface is indicated by h, such that $h = D + a$.

For small particle-collector separation distances, the hydrodynamic functions are approximated by the asymptotic expressions derived by Goldman et. al.,[50] valid in the limit $D/a < 0.003202$,

$$F_x^t \sim \frac{8}{15}\ln(D/a) - 0.9588\,, \tag{2.38}$$

$$T_y^t \sim -\frac{1}{10}\ln(D/a) - 0.1895\,, \tag{2.39}$$

$$F_x^r \sim -\frac{2}{15}\ln(D/a) - 0.2526 \tag{2.40}$$

and

$$T_y^r \sim \frac{2}{5}\ln(D/a) - 0.3817\,. \tag{2.41}$$

For larger separation distances, the asymptotic expressions for F_x^t and T_y^t,

$$F_x^t \sim -\left[1 - \frac{9}{16}\left(\frac{a}{h}\right)\right]^{-1} \tag{2.42}$$

and

$$T_y^t \sim \frac{3}{32}\left(\frac{a}{h}\right)^4\,, \tag{2.43}$$

are given by Faxén.[46] The function F_x^r is found by Goldman et al.[50] from the reciprocity relation $F_x^r/T_y^t = 4/3$,[22] such that

$$F_x^r \sim \frac{1}{8}\left(\frac{a}{h}\right)^4 . \tag{2.44}$$

The expression for T_y^r valid at large separation distances is given by Maude,[89]

$$T_y^r \sim -\left[1 + \frac{5}{16}\left(\frac{a}{h}\right)^3\right] . \tag{2.45}$$

The asymptotic expressions obtained for the hydrodynamic resistance functions are well approximated by analytical expressions derived by Duffadar and Davis.[38] These expressions, obtained by fitting the data tabulated by Goldman et. al.,[50] read

$$F_x^t = \frac{-1}{0.14116 + 0.5967\,(D/a)^{0.2984}} , \tag{2.46}$$

$$T_y^t = \frac{0.04362 - 0.0459\,(D/a)^{0.557}}{0.06801 + (D/a)^{\,0.557}} , \tag{2.47}$$

$$F_x^r = \frac{0.05826 - 0.06126\,(D/a)^{0.557}}{0.06801 + (D/a)^{\,0.557}} \tag{2.48}$$

and

$$T_y^r = \frac{-0.312373 - 0.739\,(D/a)^{0.4906}}{0.0954 + (D/a)^{0.4906}} . \tag{2.49}$$

Comparisons between hydrodynamic resistances obtained from asymptotic expressions, tabulated data (where available) and Eqs. (2.46)-(2.49) are presented in Figs. 2.1 and 2.2 for small and large particle-surface separation distances D/a, respectively.

As seen in Fig. 2.1, the agreement between both approaches increases for separation distances closer to the limit $D/a = 0.003202$. For larger separation distances, in particular in the range $0.003202 < D/a < 1$, which is the most relevant to experiments and to the results presented throughout this work, it is shown in Fig. 2.2

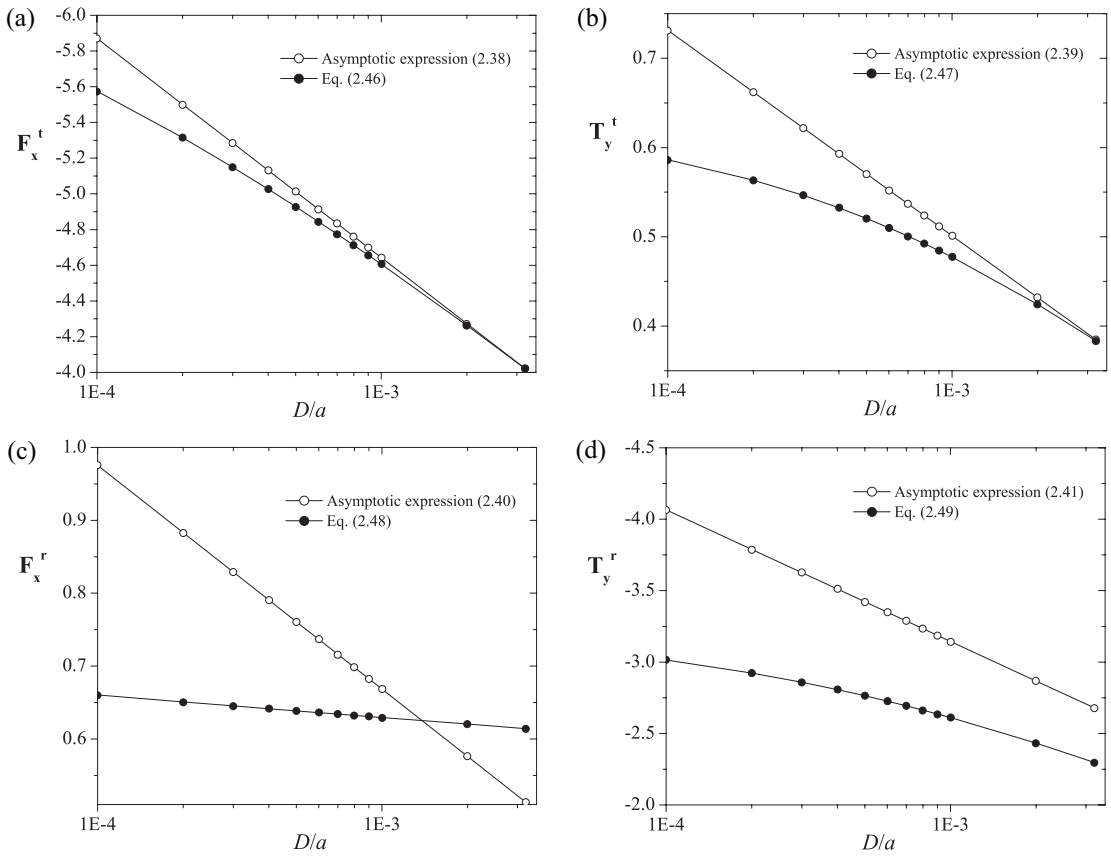

Figure 2.1. Hydrodynamic resistance functions in the separation distance range $1 \times 10^{-4} < D/a < 0.003202$ obtained from the asymptotic expressions (2.38)-(2.41) and from Eqs. (2.46)-(2.49). (a) F_x^t. (b) T_y^t. (c) F_x^r. (d) T_y^r.

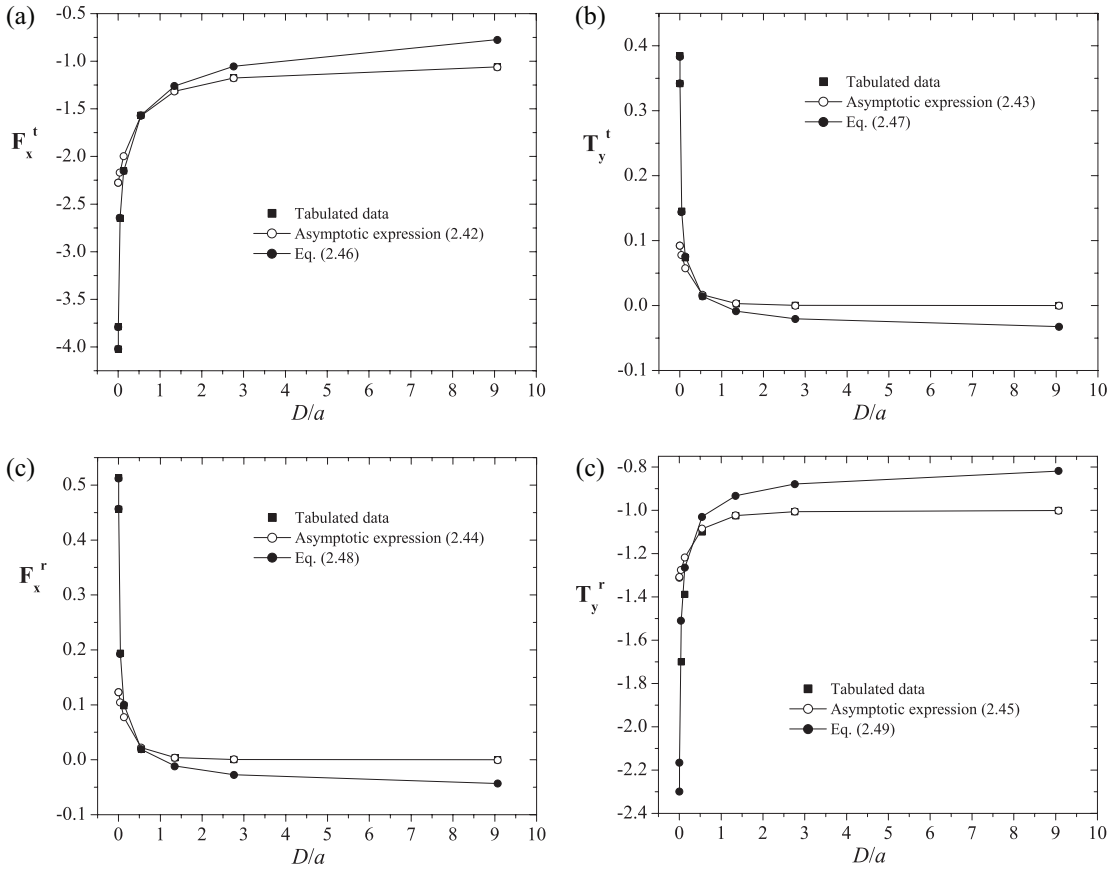

Figure 2.2. Hydrodynamic resistance functions for separation distances $D/a > 0.003202$ obtained from the asymptotic expressions (2.42)-(2.45) and from Eqs. (2.46)-(2.49). Results are compared to tabulated data of corrected calculations by Goldman et al.[50] of O'Neill's[93] bipolar coordinate solution of the translating sphere problem (F_x^t and T_y^t tabulated data), and of Dean and O'Neill's[32] solution of the rotating sphere problem (F_x^r and T_y^r tabulated data) . (a) F_x^t. (b) T_y^t. (c) F_x^r. (d) T_y^r.

that results predicted by Eqs. (2.46)-(2.49) agree almost perfectly with those obtained from the asymptotic expressions (2.42)-(2.45) and tabulated data presented by Goldman et al.[50]

In a simple linear shear flow, the particle not only translates in the direction of flow parallel to the collector surface but it also rotates about an axis parallel to the heterogeneous surface. Solving the Stokes equation ($Re \ll 1$) and the continuity equation for the fluid velocity and pressure, within the lubrication approximation, Goldman et al. developed closed form expressions for the normalized, dimensionless shear-induced (S) forces and torques[49,51]

$$F_x^{S*} = F_x^S/6\pi\mu a h\dot{\gamma} \text{ and } T_y^{S*} = T_y^S/4\pi\mu a^3\dot{\gamma}\,, \tag{2.50}$$

where $*$ symbolizes a dimensionless expression. In the limiting case of a sphere touching the planar surface ($h/a = 1$), the resulting shear-induced force and torque are $F_x^{S*} = 1.7005$ and $T_y^{S*} = 0.9440$.

For the case of larger values of h/a, for which the "method of reflections" is valid, Goldman et al.[51] derived the asymptotic expressions

$$F_x^{S*} \sim 1 + \frac{9}{16}\frac{a}{h} \tag{2.51}$$

and

$$T_y^{S*} \sim 1 - \frac{3}{16}\left(\frac{a}{h}\right)^3\,, \tag{2.52}$$

which approximate well the data obtained with the closed-form expressions presented by Goldman.[49]

On the basis of the data tabulated by Goldman et al.,[51] Duffadar and Davis[38] also developed expressions for the dimensionless shear-induced force and torque;

$$F_x^{S*} = \frac{1.7007337 + 1.0221606\,(D/a)}{1 + 1.0458291\,(D/a) - 0.0014884706\,(D/a)^2} \tag{2.53}$$

and

$$T_y^{S*} = 0.054651334(18.276952 - \exp(-1.422943(D/a))) \,. \tag{2.54}$$

In Fig. 2.3, the shear-induced forces and torques obtained from the asymptotic expressions (2.51)-(2.52) and from Eqs. (2.53)-(2.54) are compared to the tabulated data presented by Goldman et al.[51] It is seen that results obtained with Eqs. (2.53)-(2.54) agree perfectly with the tabulated data.

Unless otherwise specified, all results presented throughout this work are obtained by approximating the hydrodynamic resistance functions with Eqs. (2.46)-(2.49) and the normalized dimensionless shear-induced forces and torques with Eqs. (2.53)-(2.54).

To obtain the particle's dynamic profile as it translates and rotates in shear flow in parallel to a collecting surface, the particle's center position at every simulated time-step is updated with the velocities computed from Eq. (2.25). Particle trajectories are thus presented as plots of the minimum particle-surface separation distance D as a function of the particle's horizontal displacement in parallel to the collector.

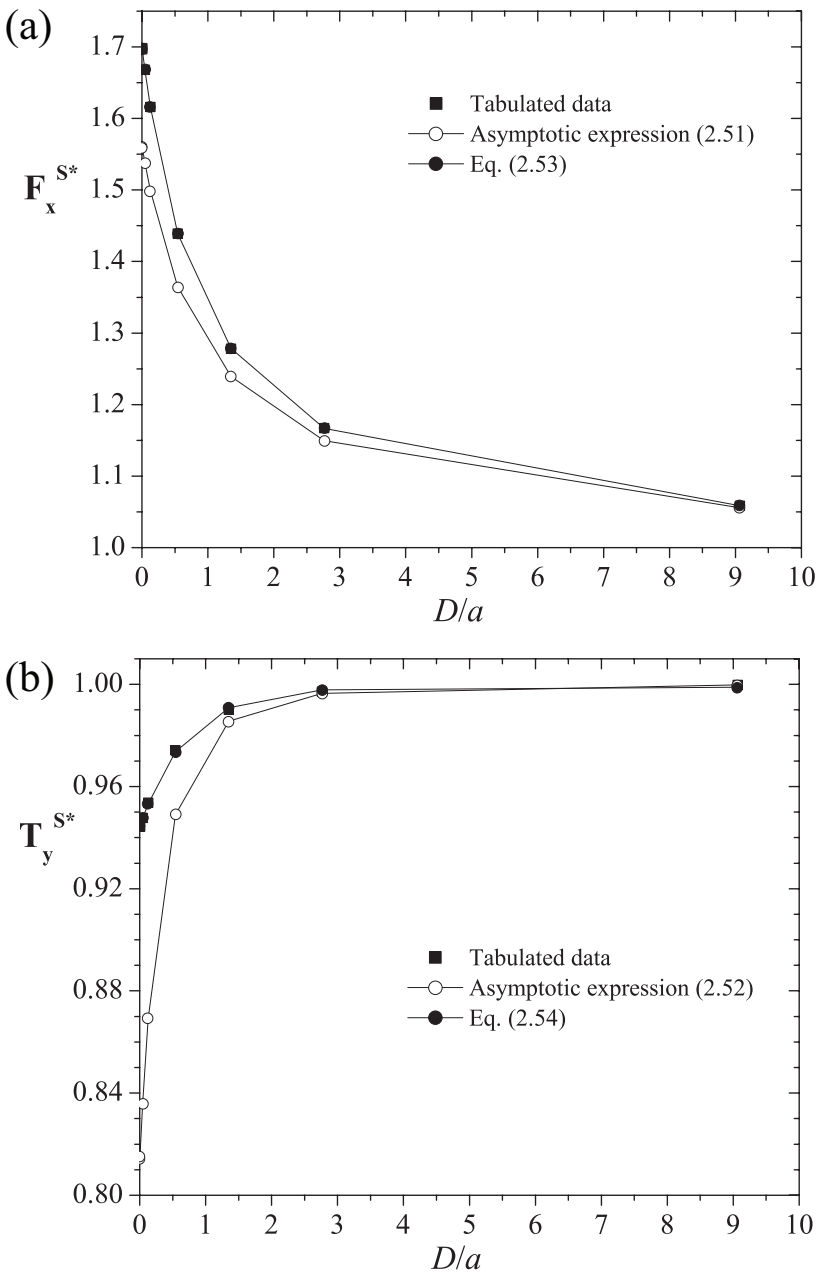

Figure 2.3. Comparison of the dimensionless shear-induced forces (a) and torques (b) obtained from the asymptotic expressions[51] (2.51)-(2.52), from tabulated data calculated with closed-form expressions[49,51] and from Eqs. (2.53)-(2.54) derived to accurately approximate such data.[38]

CHAPTER 3

PARTICLE INTERACTIONS WITH NANOSCALE-HETEROGENEOUS COLLECTORS

3.1 The GSI technique applied to chemically and topographically heterogeneous surfaces. A force- and energy-averaging model.

3.1.1 Introduction.

The effect of topographical heterogeneity on DLVO[35,117] interactions has been the focus of many studies. Discrepancies between experimental particle deposition rates and (often considerably smaller) theoretical values predicted by the DLVO model using the Derjaguin approximation have frequently been ascribed to the roughness of both the particles and collecting surfaces,[42,64,87,110,113] as asperities on both interacting surfaces were shown to decrease the total interaction energy and the height of the energy barrier. This conclusion is supported by direct measurements of the interaction energy[111] between a rough spherical particle and a smooth flat surface and by an analytical model that was developed for the same system.[110] Similar results were found from application of the surface element integration (SEI) technique,[17] described in Sec. 2.6, to rough (rippled) surfaces[18] and smooth particles interacting with collectors patterned with hemispherical[59,60,88] and cylindrical[88] pillars and pits. In all cases, a decrease in the repulsive particle-surface interaction energy barrier was attributed to surface roughness (because part of the surface is further away from the particle), which should correspond to larger deposition rates than predicted by the DLVO theory for smooth surfaces.[88]

In this section, the combined effect of topographical and electrostatic surface heterogeneity is examined by extending the applicability of the GSI technique[38,39] to a nano-pillared surface for which the surface potential on the top of the pillars differs from the potential of the underlying surface. The physical system and model formulation are described in Sec. 3.1.2. The choice of an appropriate surface discretization scheme is described in Sec. 3.1.3. In Sec. 3.1.4, interaction energies and forces are presented for particles interacting with surfaces covered with ordered arrays of pillars. The particle size and pillar height, spacing, and surface potential are varied. In Sec. 3.1.5, the computations are extended to surfaces with randomly distributed pillars and spatially varying potential, which are idealized models of surfaces that could be fabricated by the deposition of cationic patches onto pillared surfaces. A new model based on energy- and force-averaging is introduced as a simple method to compute the mean interaction energy or force between the heterogeneous surfaces. Conclusions are presented in Sec. 3.1.6.

3.1.2 Description of the model.

The model system is schematically illustrated in Fig. 3.1. A negatively-charged particle interacts with a heterogeneous substrate, which is patterned with nano-pillars of varying height (h_p), diameter (d_p), and electrostatic potential. The distance of closest approach between the sphere and the top of the pillars is D, while h represents the local separation distance (normal to the plane of the substrate) between the sphere's surface and either a pillar or the underlying portion of the surface between the pillars. For surface configurations in which the nano-pillars are arranged in an ordered fashion, the center-to-center distance between pillars is L_p. The ordered configuration is considered 'centered' (c) if a pillar or patch corresponds to the surface areal element located directly below the sphere's center. The configuration is referred

to as 'not-centered' (nc) if the surface element below the sphere's center is halfway between pillars.

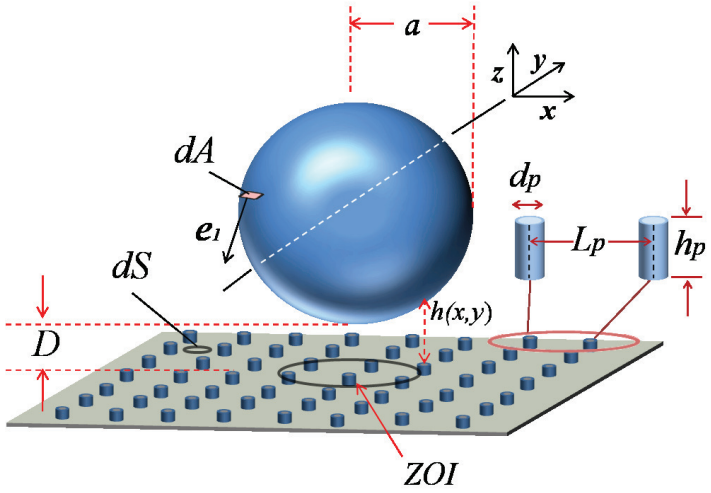

Figure 3.1. Schematic diagram of a spherical particle of radius a interacting with a topographically heterogeneous surface. The nano-pillars of diameter d_p and height h_p are separated by a center-to-center distance of L_p. The local separation distance between the sphere and the surface element vertically below it is $h(x, y)$, and D is the distance of closest approach between the sphere and the plane defined by the tops of the pillars. Areal elements on the particle and on the heterogeneous surface are indicated by dA and dS respectively. The electrostatic zone of influence (ZOI) is also indicated.

For the computations of the forces and energies, the spherical particle is located at a fixed separation distance D from the collector. The electrostatic 'zone of influence' (ZOI), defined as the area of the surface for which the interaction per unit area with the particle is significant,[38] is indicated schematically in Fig. 3.1. As described in Chapter 1, the radius of the ZOI (R_{ZOI})[81,103] is an effective length scale over which variations in the local patch density are significant. It scales to first order as[39]

$$R_{\mathrm{ZOI}} \sim \sqrt{4\kappa^{-1}a} \tag{3.1}$$

for a particle in contact with (or very close to) the surface. The size of the ZOI is also found to be an important factor affecting the interactions between colloidal par-

ticles and nano-pillared, electrostatically heterogeneous surfaces and can be used to characterize the local variations in surfaces with randomly distributed heterogeneity.

As noted in Sec. 2.7, particle-surface DLVO interactions are computed by implementing the GSI technique. In the expressions that define the colloidal energies of interaction, Eqs. (2.19) and (2.20), appropriate modifications are required in order to account for surface heterogeneities. Topographical heterogeneity is incorporated into the local separation distance $h(x, y)$ between elements on the particle and substrate. Chemical heterogeneity is incorporated by assigning different values of the Hamaker constant A_H, and of the particle and collector surface potentials $\psi_{p,1}$ and $\psi_{p,2}$, respectively, to appropriate surface elements. In the present study, $\psi_{p,2} = \psi_{p,2}(x, y)$ for the heterogeneous substrate, while $\psi_{p,1}$ is independent of position because the particle is assumed to have a uniform surface potential. A range of surface potentials is used in the results that follow. The Hamaker constant is taken to be $\mathrm{A}_H = 5 \times 10^{-21}\,\mathrm{J}$, which is representative of silica-silica interactions in aqueous solution.

3.1.3 Surface discretization scheme.

The size of the grid elements in the GSI technique is chosen to provide accuracy and efficiency for extended calculations. To preserve the local nature of the interactions, the elemental areas on the surface should be no larger than the size of the heterogeneity and may need to be smaller to provide sufficient resolution. Conversely, a surface discretization that includes extremely small grid elements increases the computational cost of the simulations and may not provide a significant benefit over direct numerical solution of the Poisson-Boltzmann equation for the particular surface and geometry.

As an illustration of convergence, a heterogeneous surface is discretized by four different grids. In each discretization scheme, the circular patches of 10 nm diameter are approximated by different numbers of square grid elements, and the grids are

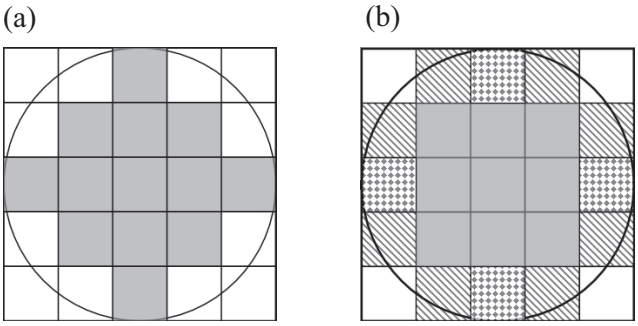

Figure 3.2. Schematic of the discretization scheme 'Grid 13'. (a) No correction factors. (b) Factors added to each grid element. Grid elements shaded with distinct patterns have different weighting factors.

named by the number of squares that represent a patch. Most simply, one patch on the surface could be modeled by one square grid element whose length equals the patch diameter. The respective force or energy computed for that element should be multiplied by the factor $\pi/4$ to account for the difference in area between the inscribed circular patch and the square grid element. Similarly, finer discretization schemes are improved by the inclusion of correction factors such that the error due to approximating a circle is minimized.

For example, in the discretization scheme Grid 13, the area of the circular patch is approximated by 13 grid elements, as shown in Fig. 3.2(a), and the particle-patch interactions result from the summation of the interactions with each of these elements. A more accurate approximation results from incorporating each of the 21 shaded squares in Fig. 3.2(b). To remove the error introduced from an inaccurate approximation of the area of a patch, the circle can be inscribed in a square whose length equals the patch diameter, and the areal contributions of each grid element can be corrected with appropriate weighting factors.

A heterogeneous surface patterned with 10 nm-diameter patches was discretized into several grids, and the DLVO interaction between a spherical particle and this surface were computed by implementing the GSI technique to test convergence. Shown in

Fig. 3.3(a) is the dimensionless electrostatic force ($F_{\mathrm{EDL}}\kappa^{-1}/(k_{\mathrm{B}}T)$) acting on a 2 μm diameter particle interacting with an electrostatically heterogeneous but flat surface as a function of the dimensionless particle-surface separation distance, κD. Similarly, shown in Fig. 3.3(b) is the dimensionless total energy of interaction ($U/(k_{\mathrm{B}}T)$) between a 10 μm diameter particle and a heterogeneous, pillared surface vs. κD.

For both the flat and the pillared surfaces, the results from Grids 1 and 13 with the correction factors are indistinguishable. As each grid incorporates the exact area of the circular patch, this agreement indicates convergence, and the coarse grid with one element per patch is sufficiently accurate in this instance. Other grid sizes that model the patch with an integer number of squares yield inaccurate results because of the error in approximating the area of a circular patch, especially for smaller particle-surface separation distances where the interactions are most sensitive to the relevant length scales. In general, the size of the surface element must be much smaller than the ZOI to incorporate the local heterogeneities accurately, $d_p/2 \ll R_{\mathrm{ZOI}} \sim \sqrt{4\kappa^{-1}a}$. Similar convergence studies were performed for the other cases considered in the remainder of this work, and the presented results were obtained using the coarsest grid that provides accurate results. For each grid element containing a circular patch, the interactions with the remaining portion of that element outside the circular patch were computed as interactions with the underlying (flat) surface. If the length scale of the heterogeneity is significantly larger than 10 nm or not small relative to R_{ZOI}, a finer grid is used such that each patch or pillar is the composite of at least 4 areal elements.

In a recent study,[88] surfaces patterned with cylindrical or hemispherical nano-asperities were modeled by a mesh composed of grid elements of 10 nm length, and it was noted that smaller grid elements could yield even more accurate results. The contribution from each grid element was not corrected by a geometric factor, so the results have some grid-dependence, as the area of the nominally circular surface of

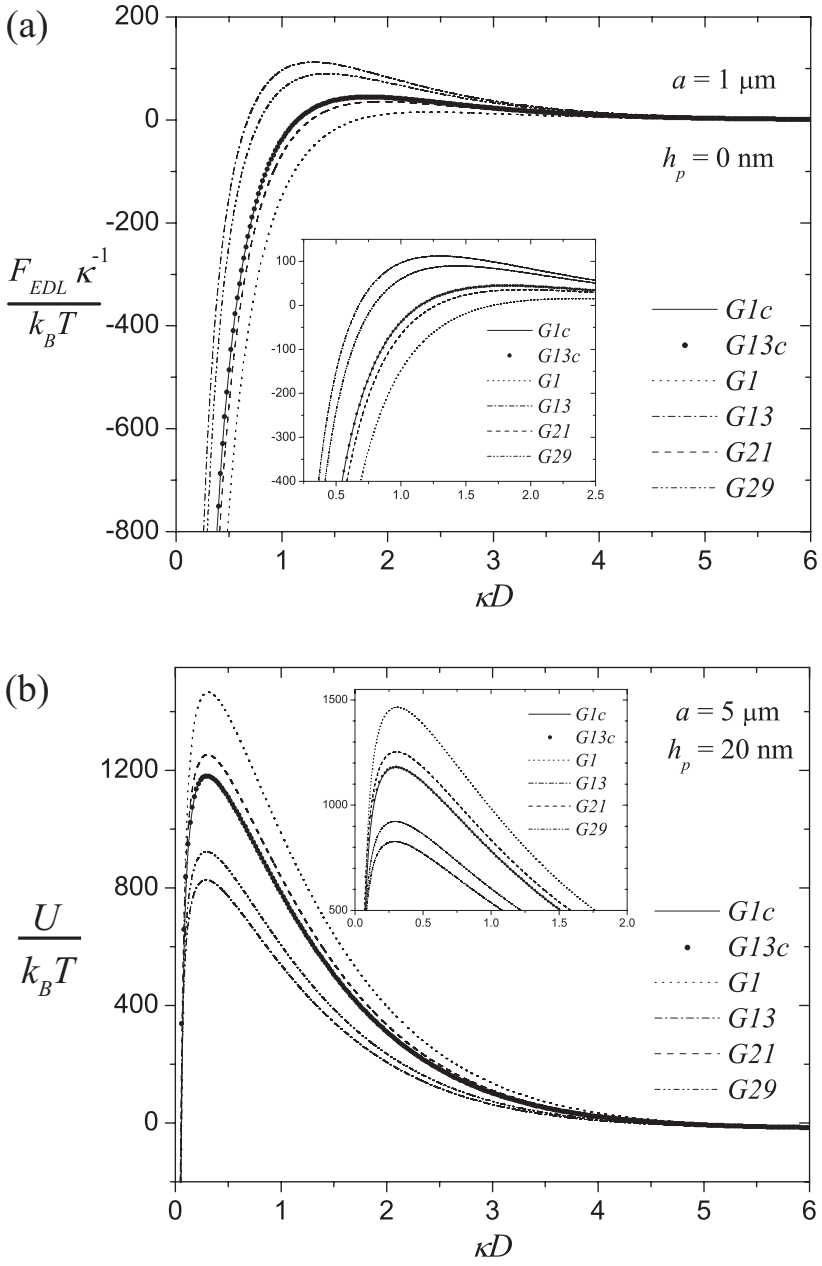

Figure 3.3. Electrostatic force and total energy for a spherical particle interacting with a heterogeneous surface for $\kappa^{-1} = 5$ nm and $A_H = 5 \times 10^{-21}$ J. The absolute temperature is $T = 298.15$ K. The heterogeneities are located on the surface in an ordered-centered configuration. (a) Dimensionless electrostatic force for a patchy surface ($h_p = 0$ nm) for $d_p = 10\,\text{nm}$, $L_p = 20\,\text{nm}$, $\psi_{\text{sphere}} = \psi_{\text{surface}} = -25$ mV, and $\psi_{\text{patches}} = 50$ mV. (b) Total energy of interaction vs. κD for a nano-pillared surface with $h_p = 20$ nm, $d_p = 50\,\text{nm}$, $L_p = 100\,\text{nm}$, $\psi_{\text{surface}} = \psi_{\text{pillars}} = -50$ mV, and $\psi_{\text{sphere}} = -25$ mV.

a pillar depends on the number of square grid elements used to represent it. This dependence becomes small as the number of elements per cylinder increases, and a hemispherical asperity is not easily modeled with a coarse grid and a correction factor, which explains the comparatively large number of elements used in that study.

3.1.4 Interaction energy between a particle and heterogeneous surface.

3.1.4.0.1 Effect of pillar height on particle-surface interactions. The results in this subsection are for the interactions between $2a = 2\,\mu$m diameter particles and surfaces patterned with nano-protrusions ("pillars") in a centered configuration. The spherical particle (ψ_{sphere}) and the underlying surface (ψ_{surface}) between the pillars are assigned the same electrostatic potential, which is typically different from that of the pillar tops (ψ_{pillars}). For surfaces patterned with nano-pillars in a centered configuration, the total energy of interaction as a function of the normalized particle-surface separation distance κD is shown in Fig. 3.4(a) for the surface potentials $\psi_{\text{sphere}} = \psi_{\text{surface}} = -27$ mV and $\psi_{\text{pillars}} = 27$ mV. Increasing the pillar height h_p reduces the potential energy barrier, which would favor particle adhesion on the surface. For fixed D, it is seen in Fig. 3.4(b) that increasing h_p decreases the vdW attraction between the sphere and heterogeneous surface. The pillars force the particle further away from the underlying surface (increasing h for the regions between the pillars), which decreases the contribution of these regions to the vdW attraction.

The EDL energy barrier is greatly reduced by the addition of the nano-pillars, which in this case are assigned an electrostatic surface potential of opposite sign to that of the spherical particle. In particular, and as shown in Fig. 3.4(c), the energy barrier observed for a flat surface is eliminated when the pillar height is increased to 10 nm. The particle-surface interactions are increasingly dominated by particle-pillar interactions as h_p is increased, while the influence of the regions of the surface without pillars is almost negligible because U_{EDL} decays strongly over a distance $D \approx 2\kappa^{-1}$.

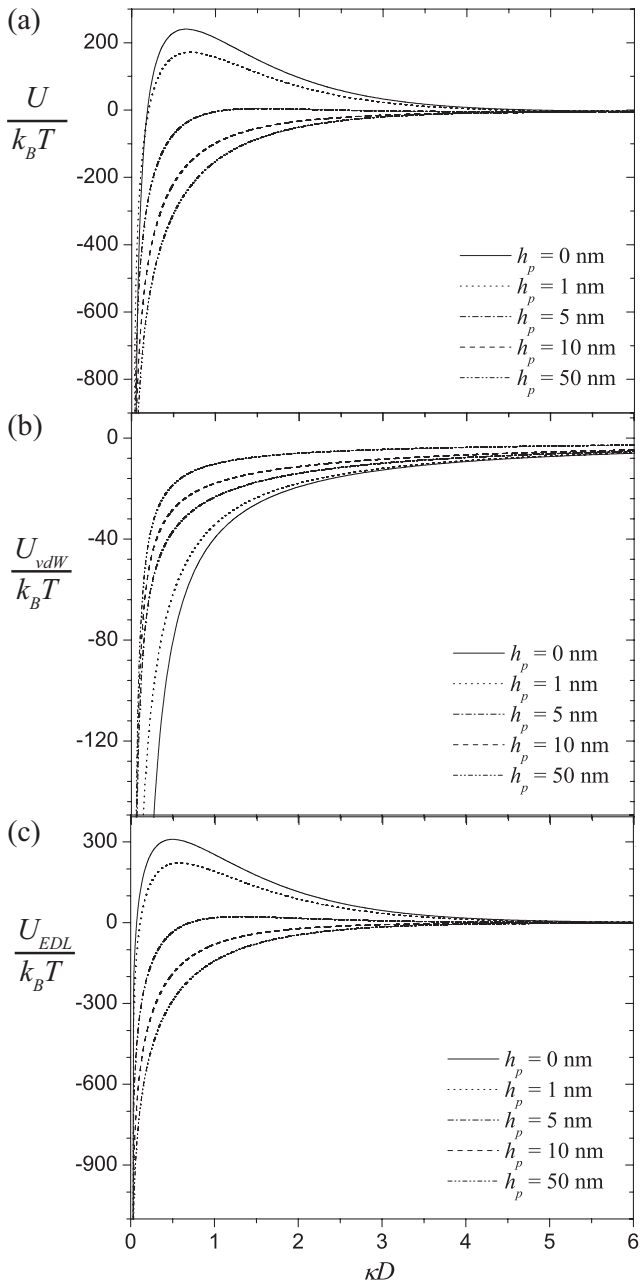

Figure 3.4. Interaction between a spherical particle of radius $a = 1\,\mu$m and a centered, nano-pillared surface with $d_p = 10$ nm, $L_p = 20$ nm, and varied h_p for $\psi_{\text{sphere}} = \psi_{\text{surface}} = -27$ mV, $\psi_{\text{pillars}} = 27$ mV, $\kappa^{-1} = 5\,$nm, and $A_H = 5 \times 10^{-21}$ J. The fraction of the surface area covered by pillars is $\Theta = 0.25$. (a) Total potential energy U vs. κD. (b) VdW energy vs. κD. (c) EDL energy vs. κD.

For the system parameters considered, *i.e.*, particle and pillar surface potentials of opposite sign, the interactions between a particle and a smooth, homogeneous surface with the same potential as the pillars are attractive. The particle-pillar interactions therefore decrease the energy barrier to adhesion because the pillars limit the minimum separation distance between the particle and the repulsive underlying surface. The reduction in the total potential energy barrier with increasing h_p in Fig. 3.4(a) is thus due to the reduction in the EDL energy barrier, which outweighs the decrease in the vdW attraction.

The total energy of interaction as a function of the dimensionless distance κD for this system is shown in Fig. 3.5(a) for $\psi_{\text{pillars}} = 54$ mV, which corresponds to a stronger attraction between the tops of the pillars and the particle. These results qualitatively resemble those shown for $\psi_{\text{pillars}} = 27$ mV, as a decrease in the total energy barrier is observed when the surface is patterned with nano-pillars with an opposite potential to that of an interacting spherical particle. In Fig. 3.5(b), the contributions of the EDL and the vdW energies are plotted separately as a function of the pillar height for fixed $D = 5\,\text{nm}$. For $\kappa^{-1} = 5$ nm, the strong decay of U with increasing h_p is due to a strong decay of U_{EDL}. The decrease of U_{vdW} with increasing h_p has a much less significant influence on the total particle-surface interactions.

For $\kappa^{-1} = 2$ nm, the decrease in both U and U_{EDL} with h_p is much less pronounced than for $\kappa^{-1} = 5\,\text{nm}$ because the magnitude of the EDL interactions is smaller for smaller κ^{-1}. Furthermore, for $h_p\kappa \gg 1$ the EDL interactions are dominated by interactions between the particle and the tops of the pillars that are in the ZOI, as the interactions with the regions of the surface between the pillars are negligible. Because $R_{ZOI} \propto \kappa^{-1/2}$, there are fewer pillars in the ZOI for smaller κ^{-1}, which reinforces the diminished decrease in U and U_{EDL} with h_p. The decrease in U with increasing h_p is not monotonic for $\kappa^{-1} = 2$ nm, as U vs. h_p has a shallow well with a minimum that corresponds to $h_p = 10$ nm. The appearance of this well indicates that

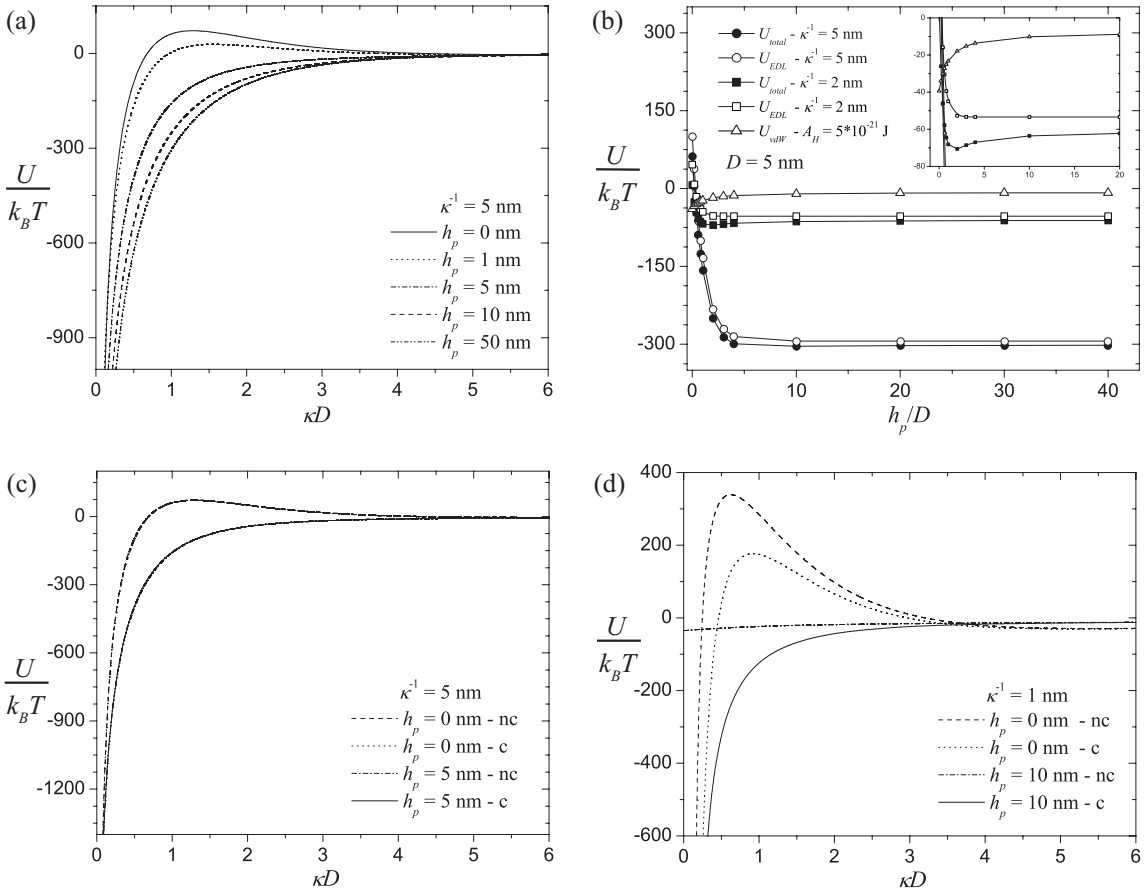

Figure 3.5. Potential energy of interaction between a $2a = 2\,\mu$m spherical particle and a nano-pillared surface with $\Theta = 0.25$, $d_p = 10$ nm, $L_p = 20$ nm, $\psi_{\text{sphere}} = \psi_{\text{surface}} = -27$ mV, and $\psi_{\text{pillars}} = 54$ mV. (a) U vs. κD for a centered configuration with varying h_p. (b) U vs. h_p/D for $D = 5$ nm. (c) U vs. κD for different h_p and surface configurations. (d) U vs. κD for different h_p and centered and not-centered surface configurations for $d_p = 20$ nm and $L_p = 160$ nm.

the competing effects of the attractive vdW forces are not always negligible, though they can be controlled by tuning the relevant parameters.

In all cases shown, U is essentially independent of the pillar height for $h_p \geq 30$ nm. For sufficiently large h_p, therefore, the overall particle-surface interactions are dominated by particle-pillar interactions because the distance between the particle and the flat portions of the surface is relatively large. Moreover, the significant decay in U as the pillar height is increased from $h_p = 0$ nm to $h_p = 1$ nm indicates that the addition of relatively short pillars or patches that protrude slightly above the surrounding surface can be sufficient to change the energetic balance of the system and possibly lead to particle deposition even if a flat surface is significantly repulsive. This strong influence of surface topography is illustrated, for example, in recent experiments involving the deposition of 1 μm silica particles from a flowing suspension onto heterogeneous, patchy surfaces. For 10 nm cationic patches that lie flat on the surface, there is a nonzero adhesion threshold, indicating that particles are captured by groups of several patches that create locally-attractive regions on the surface.[37] With 10 nm surface-immobilized nanoparticles that have a comparable charge to the patches but protrude above the underlying surface, the adhesion threshold vanishes, indicating that one nanoparticle is sufficient to capture a microparticle.[126]

3.1.4.0.2 Centered vs. Not-Centered Configurations. In the results shown in Figs. 3.5(a)-(b), the topographical heterogeneities were distributed on the surface in an ordered fashion, where the center-to-center distance between two pillars is fixed at 20 nm, the diameter of each pillar is 10 nm, and a pillar lies directly below the sphere's center. The results predicted using this *centered* surface configuration can be compared to those obtained using the *not-centered* surface configuration, for which the surface areal element located below the sphere's center is halfway between pillars. In Fig. 3.5(c), U is plotted against κD for the same parameters as in Fig. 3.5(a) for a flat surface and for $h_p = 5$ nm for both centered and not-centered configurations.

For these small and closely-spaced pillars and $\kappa^{-1} = 5\,\text{nm}$, both configurations yield nearly identical results that are indistinguishable on the plot. Results presented by Martines et al.[88] for pillars with the same potential as the flat surface show a difference between centered and not-centered configurations only for large pillar spacings ($L_p = 300\,\text{nm}$), small separation distances ($D/a < 8 \times 10^{-4}$), and small Debye lengths ($\kappa^{-1} \approx 1\,\text{nm}$). As seen in Fig. 3.5(d), the difference between the centered and not-centered configuration is much more pronounced in the present system for the parameters $L_p = 160\,\text{nm}$, $\kappa^{-1} = 1\,\text{nm}$, $d_p = 20\,\text{nm}$, and $h_p = 0$ nm and 10 nm, which is consistent with the results of Martines et al.[88]

Because the interaction energy for on-center interactions is significantly lower than for off-center interactions, lateral forces induced by the heterogeneity will bias the particles position toward on-center interactions, and off-center configurations would be very unlikely. Computations of the expected particle-surface interaction energy for such ordered surfaces should therefore use a weighted average of lateral positions. This consideration of lateral forces is particularly significant for surfaces with large asperities and under conditions of no net suspension flow. For heterogeneous features that are small with respect to the zone of influence and randomly distributed on the surface, the effects of the lateral forces are less pronounced. If the particles are transported over the (randomly) heterogeneous surface by hydrodynamic interactions in flow, the influence of the lateral forces is diminished, and the particles will more evenly sample the patchy collector.

3.1.4.0.3 Effect of particle size. Particle-surface interactions are determined not only by the height and potential of the pillars but also by the spatial extent of the ZOI, which increases in size as a increases, as seen from Eq. (3.1). Shown in Fig. 3.6 is U vs. κD for particles of varying sizes interacting with surfaces with different h_p. As shown in Fig. 3.6(a), particles with $a = 0.5\,\mu\text{m}$ and $a = 5\,\mu\text{m}$ are more strongly attracted to the patterned surface with $h_p = 1\,\text{nm}$ than to the flat surface,

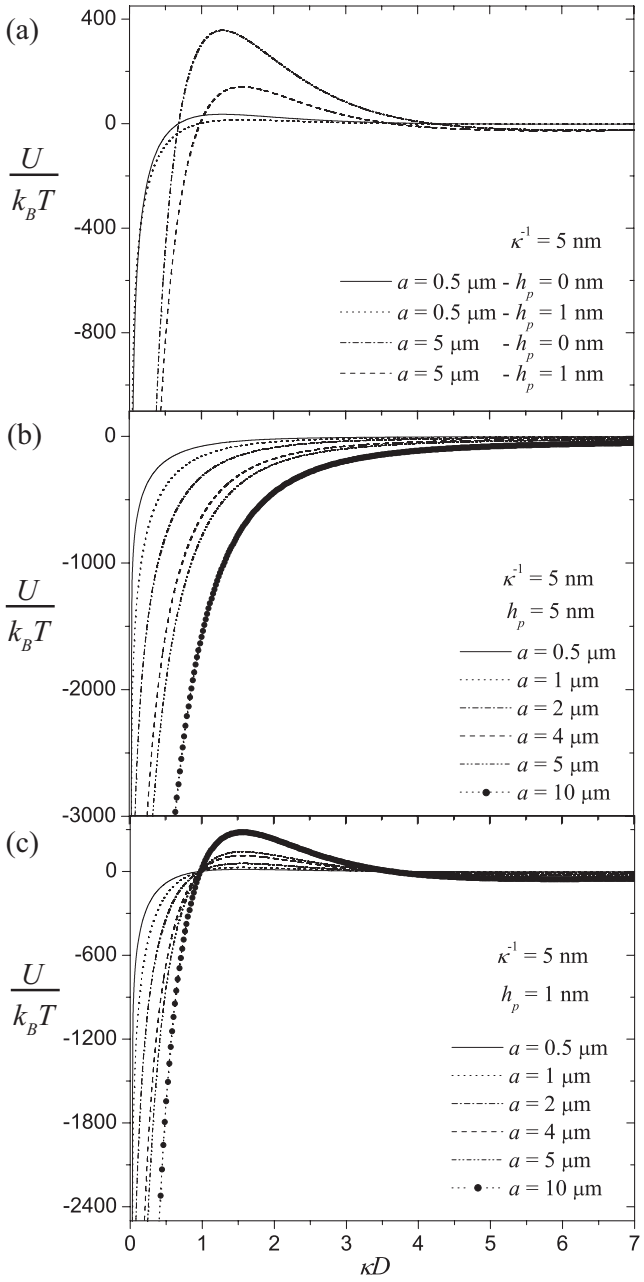

Figure 3.6. Potential energy for particles of varying size interacting with nano-pillared surfaces with $d_p = 10$ nm ordered in a centered configuration with $L_p = 20$ nm, $A_H = 5 \times 10^{-21}$ J, $\psi_{\text{sphere}} = \psi_{\text{surface}} = -27$ mV and $\psi_{\text{pillars}} = 54$ mV. (a) U vs. κD for varying a and h_p. U vs. κD for (b) $h_p = 5$ nm and (c) $h_p = 1$ nm.

which is consistent with results presented earlier. The reduction of the energy barrier relative to its maximum value for flat surfaces is about 60% for both particle sizes.

Shown in Figs. 3.6(b) and 3.6(c) is U vs. κD with $0.5\,\mu\text{m} \leq a \leq 10\,\mu\text{m}$ for surfaces patterned with pillars of heights $h_p = 5\,\text{nm}$ and $h_p = 1\,\text{nm}$, respectively. For taller pillars ($h_p = 5\,\text{nm}$), the repulsive interactions between the sphere and underlying surface between the pillars are less significant than interactions with the top of the pillars. Larger particles are therefore more strongly attracted to the surface because of their larger ZOI and a larger number of interacting pillars. As shown in Fig. 3.6(c), surfaces with shorter pillars attract larger particles more strongly at particle-surface separation distances D such that $\kappa D \leq 1$ or $\kappa D \geq 3.5$. For intermediate values of D ($1 \leq \kappa D \leq 3.5$), however, the surface is more attractive towards smaller particles. For shorter pillars, the attractive sphere-pillar interactions are opposed by significant, repulsive interactions with the underlying surface. If this repulsive interaction dominates, smaller particles are more strongly attracted to the surface because the smaller ZOI includes fewer flat surface areal elements. Each competing effect dominates the interactions for different D, as also seen in Fig. 3.6(a).

3.1.4.0.4 Interactions with both topographical and chemical heterogeneity. The GSI technique can also be applied to surfaces with chemical heterogeneity that is independent of topographical heterogeneity. Consider a surface with square nanopillars[122] of width $d_p = 20$ nm in an ordered array with $L_p = 40$ nm (corresponding to a surface coverage $\Theta_{\text{pillars}} = 0.253$) and cationic patches of diameter 10 nm that are randomly distributed on the tops of the pillars and on the surface between the pillars to yield a surface coverage of $\Theta_{\text{patches}} = 0.25$. These surfaces are highly idealized versions of surfaces that could be fabricated by depositing polyelectrolyte patches onto surfaces with topographical heterogeneity. While such surfaces might be used to control particle-surface interactions in separations and sensing applications, the idealized surfaces are introduced here primarily to illustrate the extension of the

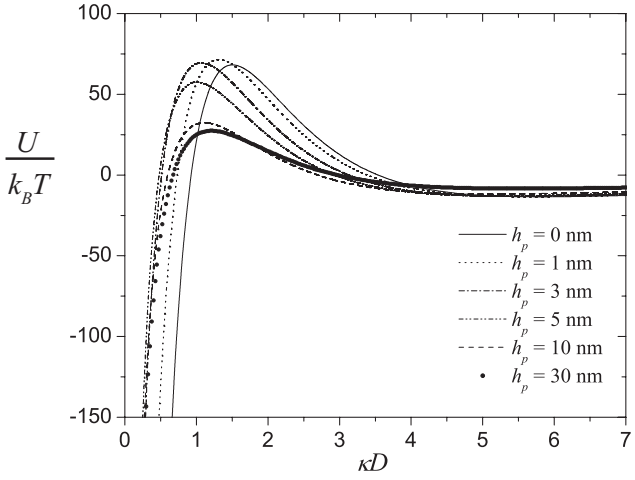

Figure 3.7. Potential energy of interaction U vs. κD between $2a = 4\,\mu$m particles and ordered surfaces with centered pillars and randomly located patches for $d_p = 20$ nm, $L_p = 40$ nm, $d_{\text{patch}} = 10$ nm, and varying h_p. Other parameters are $\Theta_{\text{pillars}} = 0.253$, $\Theta_{\text{patches}} = 0.25$, $\kappa^{-1} = 4$ nm, $A_H = 5{\times}10^{-21}$ J, $\psi_{\text{sphere}} = \psi_{\text{surface}} = \psi_{\text{pillars}} = -25$ mV, and $\psi_{patch} = 50$ mV.

GSI approach to surfaces with both types of heterogeneity. Shown in Fig. 3.7 is U vs. κD for a sphere of radius $a = 2\,\mu$m interacting with a topographically and electrostatically heterogeneous surface. It is seen that increasing h_p reduces the energy barrier even though the sphere-pillar interactions are repulsive. This reduction occurs partly from the interaction of the particle with the patches on the tops of the pillars, the competing effects of vdW interactions, and because the underlying surface is net-repulsive.

3.1.5 Force and energy-averaging model for heterogeneous surfaces with randomly distributed patches.

Computational[38,39] and experimental[37,81,103,126] studies have shown that unfavorable surfaces with electrostatic heterogeneity at the 10 nm length scale are more attractive towards the adhesion of colloidal particles than would be expected from uniform surfaces with the same net charge. While much of this behavior can be attributed to spatial fluctuations in the local density of patches, which create 'hot-spots'

that adhere particles on a net repulsive surface, computations[38] have shown that the patchy surfaces are still more attractive overall than predicted from the classical DLVO theory that treats the surface charge as uniformly smeared out over the surface. This classical DLVO approach, which is labeled the "mean field" (MF) approach in what follows, proceeds by averaging the surface potential over the heterogeneous collector,

$$\psi_{\text{avg}} = \Theta\,\psi_{\text{patch}} + (1-\Theta)\,\psi_{\text{surface}}\,, \tag{3.2}$$

where Θ is the fraction of the surface covered by patches or pillars, and then computing the mean-field interaction potential U_{EDL}^{MF} or force F_{EDL}^{MF} using the average potential ψ_{avg}. The GSI technique is applied, and the potential of each grid element on the heterogeneous surface is equal to the constant ψ_{avg} in place of $\psi_{p,2}(x,y)$ in Eq. (2.19).

The computed EDL forces on a spherical particle with $a = 0.5\,\mu$m located at a fixed separation distance $D = 5$ nm from a flat, electrostatically patchy surface are shown in Fig. 3.8(a) for varying κ^{-1}. Results are shown for the mean-field model described above and for the GSI technique averaged over 1500 surfaces with patch locations specified "randomly" to generate Poisson statistics. The fluctuation in the number of patches in the ZOI as the particle samples different locations makes some surface regions more attractive than the average, as expected. More significantly, the mean force computed from the GSI technique is considerably more attractive (or less repulsive) than that predicted from the MF model because of the nonlinearity inherent to Eq. (2.19), which does not allow a simple averaging of ψ over the surface. Indeed, Song et al.[107] assigned a *nominal surface potential* ψ_{nom} to a heterogeneous surface to calculate the EDL interaction energy, which they defined as the potential of a homogeneous surface that would produce the same EDL interaction with a particle as the heterogeneous surface (at an identical separation distance). They recognized that ψ_{nom} is not intended to describe the actual potential of the heterogeneously charged surface. Shown in Figs. 3.9(a) and 3.9(b) are U_{EDL} vs. κD calculated from

the average of the GSI technique applied to many random surfaces and the nominal surface potential ψ_{nom} that yields the same value of U_{EDL} at each D, respectively. Unfortunately, ψ_{nom} varies with separation distance D and even changes sign, which greatly limits its applicability for computing EDL interactions between particles and heterogeneous surfaces. For large particle-surface separation distances, the nominal surface potential converges to the average surface potential, $\psi_{\text{avg}} = -10.27$ mV, computed with the appropriate weighting factor Θ' for the system parameters indicated in Fig. 3.9(b).

Furthermore, as seen in Fig. 3.8(a), there is very strong agreement between the average of the GSI calculations for many randomly heterogeneous surfaces and surfaces with the same Θ but with the patches distributed in an ordered manner with constant L_p. This agreement suggests that the total interaction between the particle and surface could be determined much more accurately from a linear combination (with a suitable weighting factor) of the interactions between the particle and the repulsive and attractive elements of the surface rather than from interactions with a uniform surface bearing an average (ψ_{avg}) or even nominal (ψ_{nom}) potential.

An effective method of calculating DLVO interactions between a particle and a heterogeneous surface with (ordered or random) nanoscale variations in charge or topography begins with the GSI technique expressed in Eq. (2.23) for some local interaction $P(h(x,y))$ (force or energy) between grid elements on the particle and surface. Summing over the grid elements on the (uniform) particle, let P_i be the interaction between one of the N grid elements on the heterogeneous surface and the entire particle, such that the total interaction P_{GSI} is

$$P_{\text{GSI}} = \sum_{i=1}^{N} P_i. \tag{3.3}$$

If a collector grid element corresponds to a patch (the procedure is analogous for pillars even if the potential of the top surface is not favorable), $P_i = P_i^{att}$. If the collector

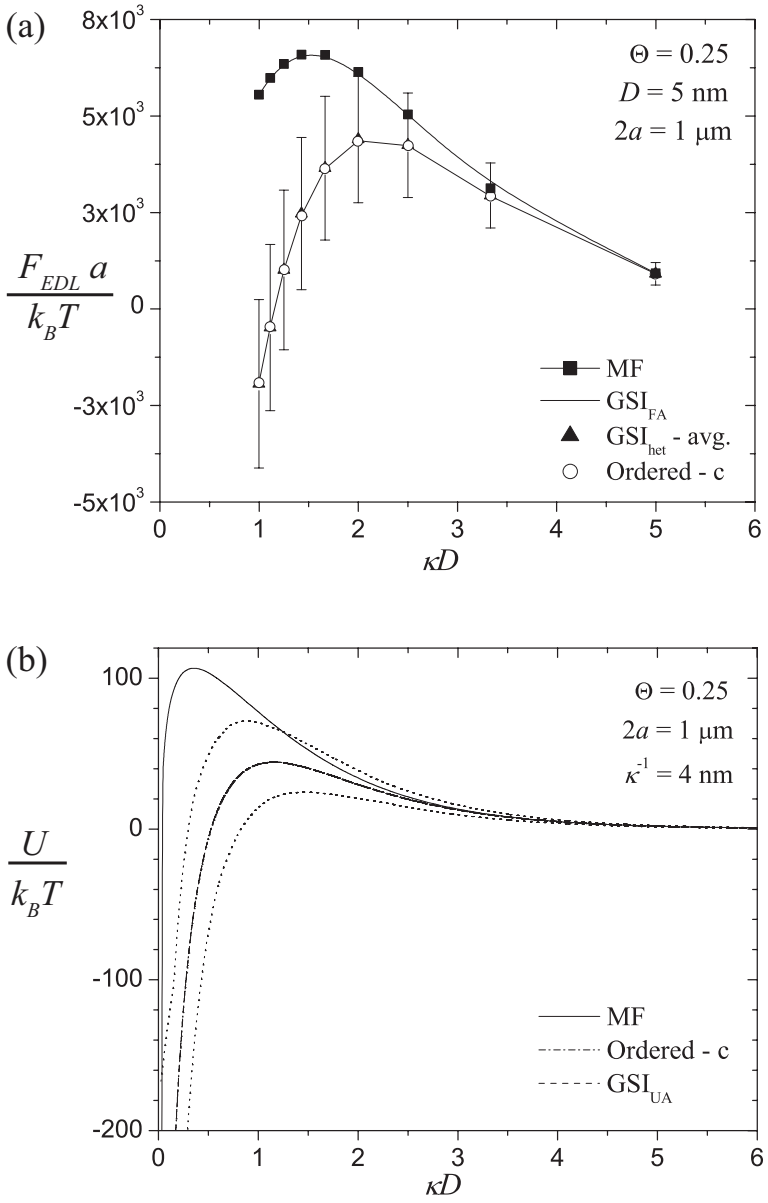

Figure 3.8. Comparison of direct GSI computations with simplified MF, $\mathrm{GSI_{UA}}$, and $\mathrm{GSI_{FA}}$ models for $2a = 1\,\mu$m particles interacting with flat, patchy surfaces with $d_p = 10$ nm, $\Theta = 0.25$, and $\psi_{\mathrm{sphere}} = \psi_{\mathrm{surface}} = -25$ mV, and $\psi_{\mathrm{patch}} = 50$ mV. $\mathrm{GSI_{het}}$ represents the average of calculations for 1500 locations on surfaces with randomly located patches. (a) F_{EDL} vs. κD for $D = 5$ nm. Error bars represent one standard deviation. (b) U_{EDL} vs. κD for $\kappa^{-1} = 4$ nm. Computations for the ordered centered configuration (dash-dotted line) coincide perfectly with predictions of the $\mathrm{GSI_{UA}}$ model (dashed line). Both dotted lines (not labeled) denote $\mathrm{GSI_{UA}}$ averages $\pm$ 1.5 standard deviations of calculations for ~ 200 surfaces with randomly located heterogeneity. Results obtained by the MF model are denoted by the solid line.

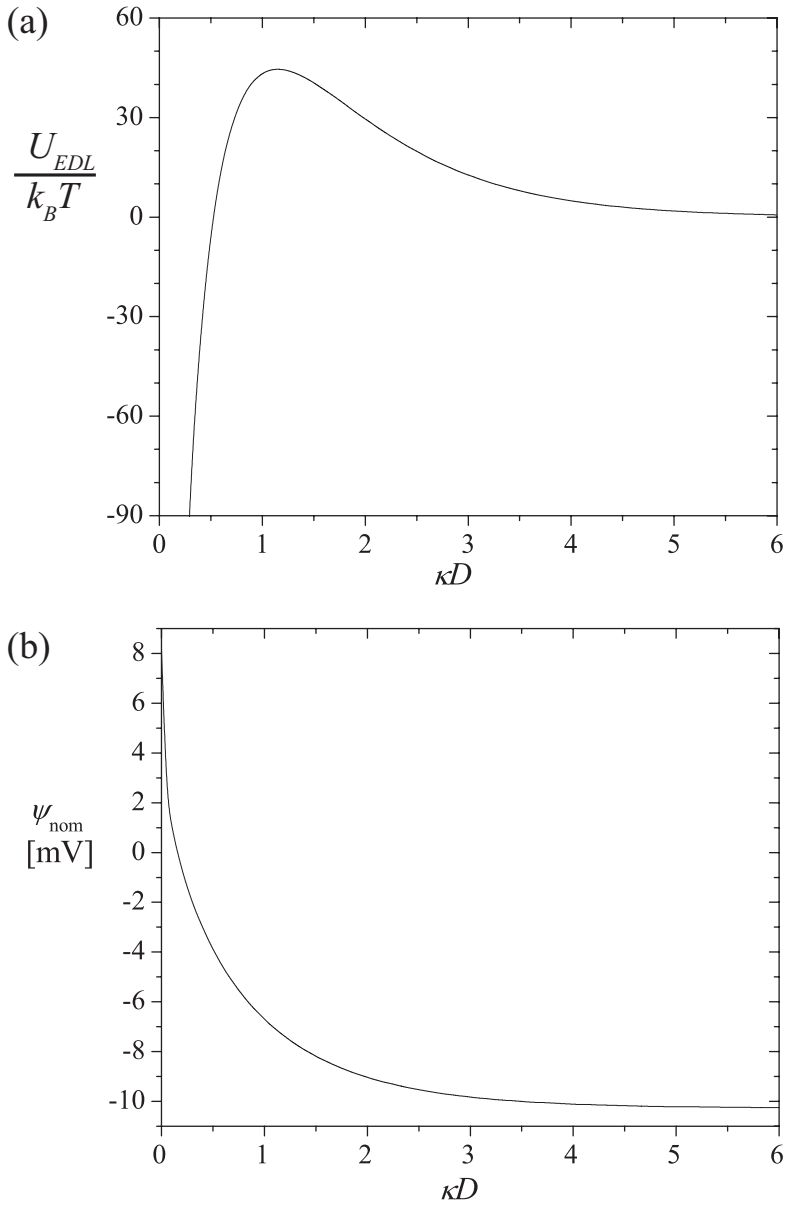

Figure 3.9. (a) $\mathrm{GSI_{UA}}$ results for U_{EDL} vs. κD for a $2a = 1\mu$m particle interacting with a flat surface with $\Theta' = 0.25\,(\pi/4)$, $\kappa^{-1} = 2\,\mathrm{nm}$, $\psi_{\mathrm{sphere}} = \psi_{\mathrm{surface}} = -25\,\mathrm{mV}$, and $\psi_{\mathrm{patch}} = 50\,\mathrm{mV}$. (b) Nominal surface potential ψ_{nom} vs. κD for the same parameters as in (a).

grid element corresponds to a repulsive region without heterogeneity, $P_i = P_i^{rep}$. The expected value of the interaction between surface element i and the particle is therefore

$$\begin{aligned} P_i &= \text{prob}(i = \text{patch}) P_i^{att} + \text{prob}(i = \text{no patch}) P_i^{rep} \\ &= \Theta P_i^{att} + (1 - \Theta) P_i^{rep}, \end{aligned} \tag{3.4}$$

where it has been implicitly assumed that each patch corresponds to one grid element. In practice, a geometrical factor is introduced to account for the circular patch, which requires replacing Θ with Θ', where $\Theta' = G\,\Theta$ for some geometrical factor G. (For a circular patch modeled by one square grid element, $G = \pi/4$.)

Substituting Eq. (3.4) into Eq. (3.3) yields

$$\begin{aligned} P_{\text{GSI}} &= \sum_{i=1}^{N} \left\{ \Theta' P_i^{att} + (1 - \Theta') P_i^{rep} \right\} \\ &= \Theta' \sum_{i=1}^{N} P_i^{att} + (1 - \Theta') \sum_{i=1}^{N} P_i^{rep} \\ &= \Theta' P^{att} + (1 - \Theta') P^{rep}, \end{aligned} \tag{3.5}$$

where P^{att} is the interaction (force or energy) between a particle and a homogeneous surface with the same potential as the patches (or pillar tops) and P^{rep} is the interaction between a particle and a homogeneous surface with the same potential as the (repulsive) surface between the patches or pillars. At a given separation distance, the average interaction between a particle and a heterogeneous surface with randomly-distributed, nanoscale charge heterogeneity can therefore be determined from Eq. (3.5) for any Θ'. This approach requires only two GSI computations: one for a homogeneous surface with $\Theta = 0$ and one for a homogeneous surface with $\Theta = 1$. Eq. (3.5) is, therefore, a powerful result.

Equation (3.5) can be applied to surfaces with patches of different Hamaker constant or for surfaces with nano-pillars or nano-pits that replace the patches, and Θ' is the fraction of the surface covered by patches or pillars. When applied to pillared surfaces, the GSI computation of P^{att} is performed with $D = D_p$, the separation distance between the particle and the plane determined by the tops of the pillars, and the computation of P^{rep} is performed with $D = D_s$, the separation distance between the particle and the underlying surface, such that $D_s - D_p = h_p$. The method based on Eq. (3.5) is termed the *force-averaging* ($\mathrm{GSI_{FA}}$) model if $P = F_{\mathrm{EDL}}$ and the *energy-averaging* ($\mathrm{GSI_{UA}}$) if $P = U_{\mathrm{EDL}}$. This approach is based on a linear combination of forces or energies computed between the particle and homogeneous surfaces corresponding to $\Theta = 0$ and $\Theta = 1$, rather than a linear combination of surface potentials that is subsequently used to compute the EDL force or energy. By contrast, net surface potentials determined for $0 < \Theta < 1$ correspond more closely to ψ_{avg} and cannot be used directly to compute accurate DLVO interactions. For example, it has been noted that the apparent zeta potential of heterogeneous particles or heterogeneous collecting surfaces determined from electrophoresis[115,116] or streaming potential measurements[9] does not yield accurate predictions of colloidal forces or stability.

For systems with well-defined heterogeneity, such as silica particle deposition onto surfaces with adsorbed polyelectrolyte patches,[81] it is typically straightforward to determine the surface potentials corresponding to $\Theta = 0$ and $\Theta = 1$. The potential corresponding to $\Theta = 0$ can be determined from zeta potential or streaming potential measurements for the bare surface with no heterogeneity. The potential corresponding to $\Theta = 1$ can be determined by repeating this measurement for a surface saturated with patches. The determination of the relevant surface potentials for systems with heterogeneity that is not as well characterized or controlled, such as inherently rough surfaces for which the true surface potential may be obscured in measurements, requires the coupling of the measurements with a model for the

apparent surface potential of a surface with a particular roughness distribution to elucidate the true surface potential.

The $\mathrm{GSI_{FA}}$ and $\mathrm{GSI_{UA}}$ models are entirely different than the patchwise model[78, 79, 107] that was previously applied to determine particle deposition rates on heterogeneous surfaces with large patches. In that approach, the macroscopic patches of equal potential are treated as homogeneous surfaces, and the particle deposition rate is found from a linear combination of the deposition rates on homogeneous surfaces corresponding to the favorable and unfavorable regions of the patchy surface. Deposition rates predicted by the patch model did not agree with experimental rates[40] determined for systems with surface heterogeneities much smaller than the interacting spherical particle. As seen from Fig. 3.8, the $\mathrm{GSI_{FA}}$ and $\mathrm{GSI_{UA}}$ models yield results that are indistinguishable from the average of individual GSI computations performed for numerous surfaces with randomly distributed patches and have a much lower computational cost.

The GSI, $\mathrm{GSI_{UA}}$, and MF models are also applied to the computation of the electrostatic energy of interaction between a $1\,\mu$m diameter particle and a surface patterned with flat patches at a fixed Debye length of $\kappa^{-1} = 4$ nm, with results presented in Fig. 3.8(b). The profile based on the average of GSI calculations for many different surface locations converges to that predicted by the $\mathrm{GSI_{UA}}$ model as the number of surfaces (or surface locations) is increased. The results from the simple MF model based on the average surface potential $\psi_{\mathrm{avg}} = -10.27$ mV clearly provide little, if any, useful information about U_{EDL} for $\kappa D < 2$. The actual average interaction ($\mathrm{GSI_{UA}}$) has an energy barrier nearly $60\,k_BT$ lower, indicating that the surface is considerably less repulsive on average than predicted by the MF model. Furthermore, as indicated by the envelope of ± 1.5 standard deviations about the mean, there are surface regions that are much less repulsive than the average character of the surface.

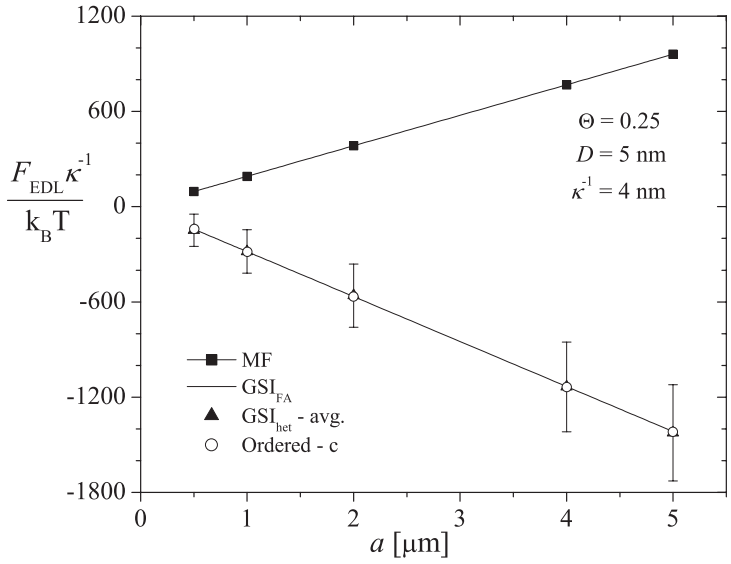

Figure 3.10. Comparison of different models to calculate average electrostatic forces F_{EDL} between particles of varying sizes and surfaces with randomly distributed nano-pillars for $d_p = 10$ nm, $h_p = 0$ nm, $\Theta = 0.25$, $\psi_{\mathrm{sphere}} = \psi_{\mathrm{surface}} = -54$ mV, and $\psi_{\mathrm{patches}} = 108$ mV.

For particles of varying sizes interacting with heterogeneous surfaces, a similar comparison of the models was performed for the computation of the electrostatic forces at a fixed Debye length of $\kappa^{-1} = 4$ nm, and results are shown in Fig. 3.10. For all particle sizes, the $\mathrm{GSI_{UA}}$ model yields results that are in excellent agreement with the average of forces computed by implementing the GSI technique for an ordered surface and for many surfaces with randomly located heterogeneities.

3.1.5.1 The $\mathrm{GSI_{UA}}$ and $\mathrm{GSI_{FA}}$ models extended to nano-pillared surfaces.

The $\mathrm{GSI_{FA}}$ model can also be used to compute electrostatic forces between a particle and a nano-pillared surface. In Fig. 3.11(a) the electrostatic force on a particle with $a = 0.5\,\mu$m is plotted vs. κD for surfaces with short pillars. The agreement between the results predicted by the force-averaging model and the average of GSI computations performed for about 1500 randomly patterned surfaces is excellent. For

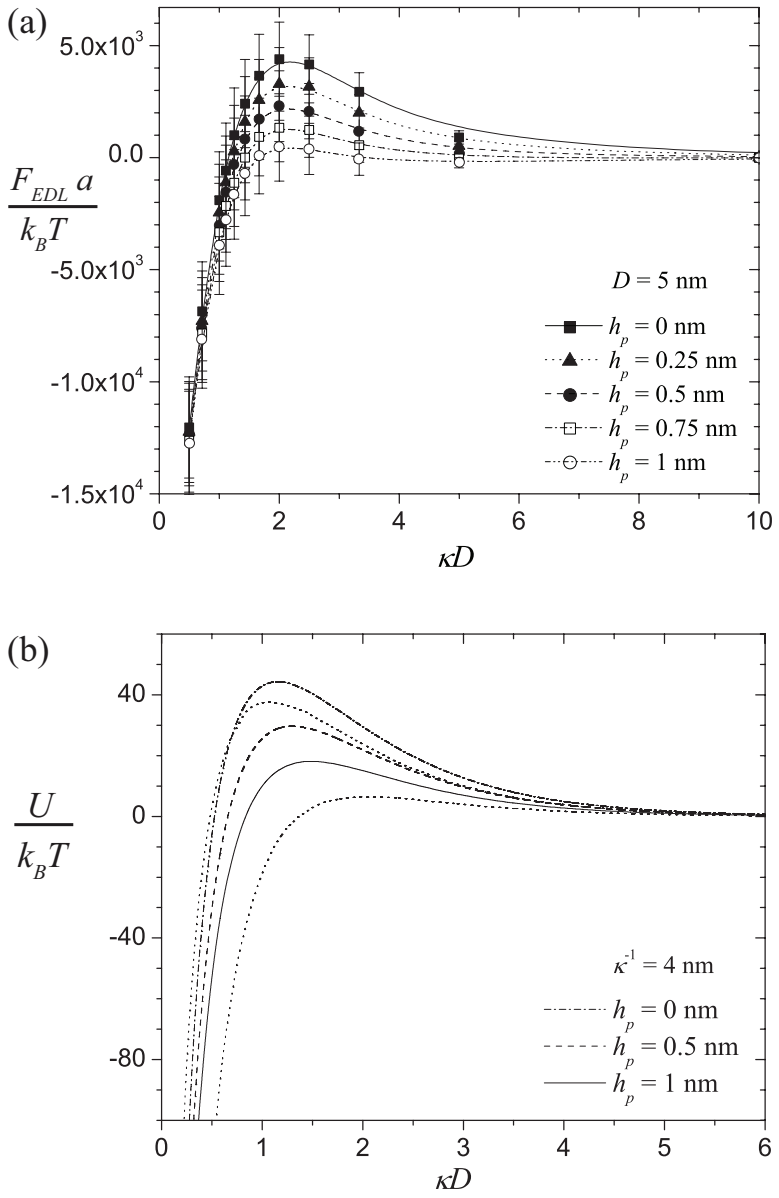

Figure 3.11. Comparison of different models to calculate average interactions between a particle with $a = 0.5\,\mu$m and surfaces with randomly distributed nano-pillars for $d_p = 10$ nm, $\Theta = 0.25$, $\psi_{\text{sphere}} = \psi_{\text{surface}} = -25$ mV, and $\psi_{\text{patches}} = 50$ mV. (a) F_{EDL} vs. κD for fixed $D = 5$ nm and various h_p. Results are shown from the GSI_{FA} model (curves) and from averaging 1500 individual GSI calculations (symbols) for different positions on surfaces with randomly distributed pillars. The error bars represent one standard deviation. (b) U_{EDL} vs. κD for $h_p = 0$ nm (dash-dotted line), 0.5 nm (dashed line), and 1 nm (solid line). Both dotted lines denote GSI_{UA} averages $\pm$ 1.5 standard deviations of calculations for 200 surfaces with randomly located heterogeneity for $h_p = 1\,$nm.

a range of κ^{-1}, F_{EDL} is significantly more attractive with the inclusion of pillars as short as 1 nm.

As seen in Fig. 3.11(a), the addition of pillars that extend only a nanometer above the surface is sufficient to transform a surface with reasonably strong repulsion towards particles into one that is attractive on average. This result has significant implications for colloidal deposition onto heterogeneous surfaces with adsorbed polyelectrolytes.[9,37,81,103] Not only are the surfaces more attractive than expected from a MF model, but fluctuations in the local patch density create locally attractive regions on net-repulsive surfaces (as noted previously), and polyelectrolyte patches that extend only a fraction of a nanometer above the surface create an even stronger attraction than anticipated if the surface is considered flat. Significant deposition of colloidal particles could therefore occur even for surfaces predicted to be repulsive, using refined techniques to account for electrostatic heterogeneity (e.g., GSI[38,39]), if nanoscale variations in the topography of the surface are not included.

Plotted in Fig. 3.11(b) is U vs. κD with $\kappa^{-1} = 4\,\mathrm{nm}$ computed from the $\mathrm{GSI_{UA}}$ model and from the mean of 200 heterogeneous surfaces with randomly distributed patches. For these parameters, an increase from $h_p = 0$ to $h_p = 0.5\,\mathrm{nm}$ decreases the mean energy barrier by $\sim 17\,k_BT$, and an increase to $h_p = 1\,\mathrm{nm}$ reduces the barrier by $\sim 26\,k_BT$.

In Fig. 3.12(a), U_{EDL} vs. D/h_p is plotted for various κ^{-1}. The energy barrier increases with increasing κ^{-1} and is reached at a larger D. The dependence of $\max(U_{\mathrm{EDL}})$ on κ^{-1} is shown in Fig. 3.12(b) for varying h_p. The energy barrier increases with κ^{-1} for $h_p > 0$. The energy barrier is smaller for larger h_p because the attractive sphere-pillar interactions become more significant as h_p is increased. By contrast, the energy barrier decreases slightly with increasing κ^{-1} when the interacting surface is patterned with flat patches. Moreover, the magnitude of the variations for patchy collectors is only $\sim 2.5\ k_BT$ for $0\,\mathrm{nm} < \kappa^{-1} < 20\,\mathrm{nm}$, while a much greater

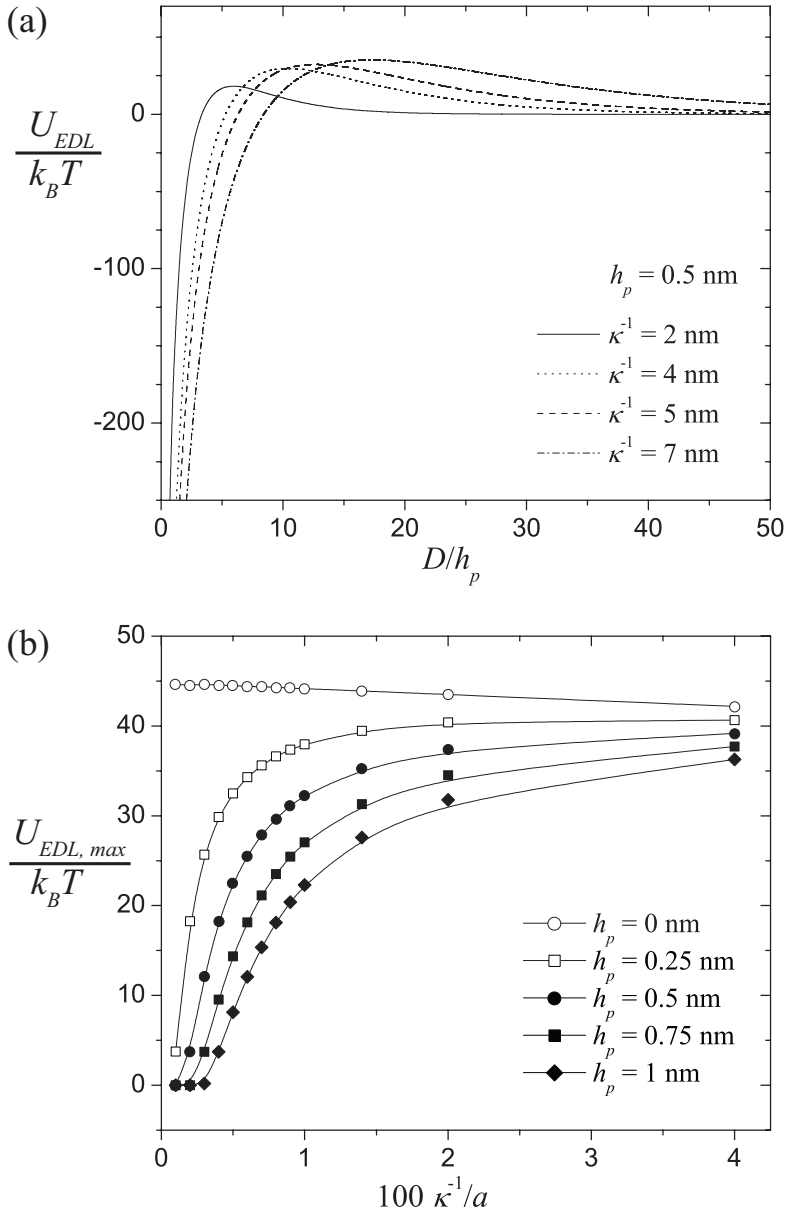

Figure 3.12. $\mathrm{GSI_{UA}}$ results for EDL energy for a particle with $a = 0.5\,\mu$m interacting with a pillared surface with $d_p = 10$ nm, $\Theta = 0.25$, $\psi_{\mathrm{sphere}} = \psi_{\mathrm{surface}} = -25$ mV, and $\psi_{\mathrm{patch}} = 50$ mV. (a) U_{EDL} vs. κD for $h_p = 0.5$ nm and several κ^{-1}. (b) $\max(U_{\mathrm{EDL}})$ vs. κ^{-1}/a for several h_p.

change is observed for nano-pillared surfaces ($\sim 37.5 k_B T$, in average) with pillars that are only a fraction of a nanometer high. For flat surfaces, both the attractive and repulsive components of the surface are similarly influenced by a variation of the Debye length, so that the overall variation of the electrostatic energy barrier is minimal. The results in Fig. 3.12(b) further suggest that small variations in topography can be sufficient to remove large EDL barriers to colloidal deposition on patchy surfaces.

3.1.6 Conclusion.

The GSI technique has been extended and used to compute the force and potential energy of interaction between a microsphere and patterned surfaces with both chemical and topographical variations at the nanoscale. The chemical heterogeneity is created by 10 nm-diameter patches distributed at random on the surface, and the patches are assigned a different potential than that of the underlying surface. The topographical heterogeneity arises from nanopillars of varying height, diameter, and arrangement. This nano-topography decreases the size of the potential energy barrier for unfavorable surfaces because the pillars limit the minimum separation distance between the interacting surfaces, and this effect is enhanced if the surface potential is not uniform. The topography has a significant influence on the interaction even for very short pillars, as a strongly unfavorable surface with chemically-heterogeneous patches can become net-attractive if the patches extend $O(1\,\text{nm})$ above the underlying surface. This result indicates that even refined techniques for electrostatically heterogeneous surfaces may underpredict colloidal deposition unless nanoscale variations in the surface topography are included.

A novel force- and energy- averaging model has also been introduced as a simple technique to compute the net interaction force or energy between a colloidal particle and a patchy heterogeneous surface. The results are identical to the arithmetic mean of many GSI computations for different locations on the patchy surface, or

equivalently, of many randomly heterogeneous surfaces, but require only two GSI computations for homogeneous surfaces: one with the potential of the patches and one with the potential of the underlying surface. This averaging technique is not restricted to the GSI approach but can also be applied with the SEI technique or the Derjaguin approximation used to compute the interactions between homogeneous surfaces. The net interactions with heterogeneous surfaces are significantly more attractive than estimated from a simple mean-field approach with an average surface potential. The GSI_{FA} and GSI_{UA} models are particularly relevant for computing interactions involved in colloidal deposition with adsorbed polyelectrolyte patches, as the apparent zeta potential[9,115] of heterogeneous particles or collecting surfaces does not yield accurate predictions of colloidal forces or stability, because the net surface potential corresponds more closely to the average (arithmetic mean) potential ψ_{avg} in a mean-field approach. These results also help explain the increased attraction towards colloidal particles (relative to standard DLVO calculations) of net-repulsive, patchy surfaces with randomly distributed, attractive nanoelements.

3.2 Mean and variance of DLVO interaction energies and particle adhesion thresholds. A statistically-based model.

3.2.1 Introduction.

Deposition morphologies and the dynamic adhesion of colloidal particles,[2,7,9,72,81,103] bacteria,[31,102] and cells[57,75] on heterogeneous substrates are typically controlled by chemical and topographical surface features. Estimates of particle deposition rates on heterogeneous surfaces based on a linear patchwise model[70,107] are accurate for patches much larger than the depositing colloidal particles. For surface heterogeneities much smaller than the colloidal particles, however, the predictions of the patchwise model do not agree with experimentally determined deposition rates,[40] as some deposition is always predicted if any region of the surface is favorable. By contrast, in exper-

iments with colloidal particles flowing over net-unfavorable surfaces with adsorbed polyelectrolyte chains or patches of $O(10\,\mathrm{nm})$,[9,37,81] deposition is observed only if the areal fraction of the surface covered by the patches, Θ, exceeds a nonzero adhesion threshold, Θ_{crit}. This nonzero threshold indicates that, for patches much smaller than the particles, a group of patches, creating a local "hot spot", is required to adhere a particle.

Recent computations based on the trajectories of individual particles have accurately reproduced measured deposition rates and adhesion thresholds.[37] While direct simulations of particle motion yield experimentally-validated phase space diagrams that delineate dynamic adhesion regimes of skipping, rolling, and arrest, this approach is computationally expensive. Many different trajectories must be generated to ensure a statistically meaningful sample of the heterogeneity, and each point in the trajectory of an individual particle requires the computation of DLVO interactions with a particular location on a heterogeneous surface.[38] There is thus a need to predict particle interactions with nanoscale, patchy surfaces without the details of many particle trajectories. Progress has been made through a statistically-based model within the framework of the random sequential adsorption (RSA) approach,[8,9] with the number of macro-ions that form a locally-attractive adsorption center a key parameter of the model.

In the present section, a statistical approach is introduced as an alternative method to quantify the effect of randomly-located surface heterogeneities on adhesion thresholds and spatial fluctuations in the potential energy of interaction, which replaces the need for lengthy computations of particle trajectories. This approach requires no assumption of the number of patches involved in particle capture, as the presence of locally attractive regions is determined from DLVO calculations for the patchy surface.

A description of the model is presented in Sec. 3.2.2, and trajectories of particles interacting with patchy surfaces are presented in Sec. 3.2.3. In Sec. 3.2.4, collection probability curves are constructed from the trajectories of particles flowing over the heterogeneous collector surface. In Sec. 3.2.5, a statistical model[14] is extended to characterize spatial fluctuations in the particle-collector interaction energy, which enables the identification of local hot spots on net-unfavorable, heterogeneous surfaces without explicit surface construction. This statistical model is then used to determine adhesion thresholds in Sec. 3.2.6 and applied to particle adhesion on nanopatterned surfaces. Excellent agreement is found with the trajectory-based approach of Sec. 3.2.4. Conclusions are presented in Sec. 3.2.7.

3.2.2 Description of the model. Computational method.

Presented in Fig. 3.13(a) is a schematic diagram of the model system, which resembles the system described in Sec. 3.1.2 and that used in experimental set-ups.[37,81,103] The flowing particles of radius a are negatively charged, and the collector substrate consists of a negatively charged flat surface patterned with positively charged cylindrical asperities of height h_p and diameter d_p, located at randomly selected locations. The electrostatic potentials of the spherical particle and bottom flat surface are $\psi_{\text{sphere}} = \psi_{\text{surface}}$ = -25 mV, and that of the nano-heterogeneities ("patches" or "pillars") is $\psi_{\text{patch/pillar}} = 50$ mV. The local particle-surface separation distance is denoted by h, while D is the minimum separation distance between the particle's surface and either the bottom flat surface or the top of the pillars. Due to the linear shear flow with shear rate $\dot{\gamma}$, the particle translates in the x-direction with a linear velocity V_x and rotates around an axis parallel to the collector surface with a rotational velocity Ω_y. The particle velocities are obtained from the mobility matrix formulation presented in Sec. 2.8, and it is assumed that the nano-protrusions on the collector surface have a negligible influence on the velocity field. The shear-induced

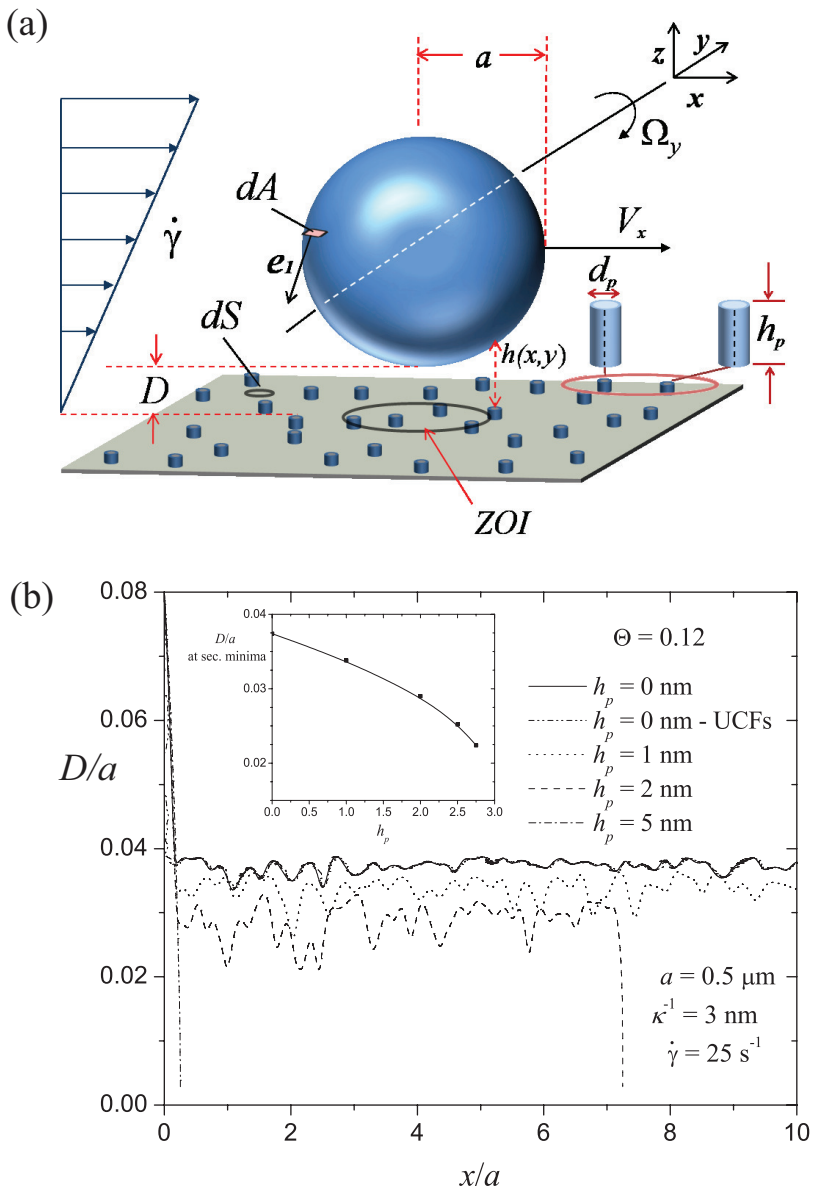

Figure 3.13. (a) Schematic diagram of a spherical particle of radius a interacting in shear flow with a heterogeneous surface with nano-pillars of diameter d_p and height h_p. The electrostatic zone of influence (ZOI) is indicated. (b) Trajectories of $1\,\mu$m diameter particles interacting in shear flow with heterogeneous surfaces with different h_p for randomly distributed pillars. The parameters are $A_H = 5\times10^{-21}$ J, $\psi_{\text{pillar}} = 50$ mV, $\psi_{\text{sphere}} = \psi_{\text{surface}} = -25$ mV, and $Pe = 6\pi\mu a^3\dot{\gamma}/k_BT = 14.31$, where $\mu \simeq 1\cdot10^{-3}$ Pa $\cdot$ sec is the water viscosity at T = 298.15 K. The decrease of D/a at the secondary minima with increasing h_p is shown in the inset. For $h_p = 0$, Brownian motion is computed from Brownian forces (solid line) and from Brownian displacements with UCFs (dash-dot-dot line).

force and torque on the particle are determined from Eqs. (2.50) and the dimensionless correction factors are given by Eqs. (2.53) and (2.54). The inertial lift force on the particle is negligible at these low Reynolds numbers,[38] so particle motion in the z-direction normal to the collector results only from DLVO interactions and Brownian motion. Brownian effects for the results presented in this section are incorporated from the stochastic expression[91]

$$F_{\mathrm{Br}} = \frac{k_B T}{a}\,\hat{\eta}\ , \tag{3.6}$$

where $\hat{\eta}$ is a random number of the normal standard distribution. The effects of Brownian motion on trajectories of particles interacting with nanoscale heterogeneous collectors is studied in detail in Sec. 3.3. The DLVO forces per unit area (EDL and vdW forces) between the particle and the heterogeneous surface are obtained from Eq. (2.24) and then incorporated into the GSI technique.

3.2.3 Particle trajectories.

In this section, the GSI technique is applied to compute trajectories as particles translate under shear flow and interact with a topographically and electrostatically heterogeneous surface.

For a given amount of surface charge, a model heterogeneous surface of $15\,\mu$m x $15\,\mu$m in size is generated by assigning patches or pillars at randomly selected locations. Once the collector surface is constructed, the centers of flowing particles are initially positioned on the left edge of the collector, at randomly sampled locations along the y-axis. The initial separation distance ($D = 40\,$nm) is sufficiently large that the particles must overcome an energy barrier closer to that of a net-repulsive surface. The particle trajectories (separation distance vs. distance translated in x) are determined by integrating $d\mathbf{x}/dt = \mathbf{V}$ in time, with $\mathbf{x} \equiv (x, y, z)$ the position of the particle. If the particle-surface separation distance falls below a certain threshold

($D \leq \delta = 1\,\text{nm}$), the particle is considered to be irreversibly adhered to the surface. This value of the limiting distance for adhesion is chosen so that the particle adheres close to the primary minimum (as seen, for example, in Fig. 3.16(a)). Additional calculations with smaller δ yielded the same results. A simulation is also stopped when a particle translates over the entire collector without adhering.

Trajectories for $1\,\mu$m diameter particles flowing over a heterogeneous surface with a fixed surface coverage of $\Theta = 0.12$ and varying pillar heights are shown in Fig. 3.13(b). For the set of chosen parameters and surfaces with relatively tall pillars, the flowing particles are arrested due to strong attractive interactions, either with the first few pillars the particle encounters ($h_p = 5\,\text{nm}$) or after translating an horizontal distance of $x \simeq 7a$ ($h_p = 2\,\text{nm}$). For shorter pillars ($h_p = 0, 1\,\text{nm}$), however, the particles flow over the collector without adhering.

The trajectories exhibit fluctuations independent of Brownian effects that instead arise from variations in the number of patches in the electrostatic zone of influence (ZOI). As $D/a \to 0$, the radius of the zone of influence at leading order is $R_{\text{ZOI}} = \sqrt{4\kappa^{-1}a}$.[38] The dynamic behavior is therefore determined by the fluctuating energy landscape as the particle samples the surface, which is induced by the competition between repulsive interactions with the underlying surface and attractive interactions with patches or pillars. Increasing the pillar height strengthens the attractive interactions, decreasing the average particle-surface separation distance D/a and increasing the magnitude of the profiles' fluctuations. The decrease in D/a at the secondary minimum (determined from the mean of U vs. D calculations at many surface locations) with increasing h_p is shown in the inset in Fig. 3.13(b). These D/a values are in excellent agreement with the arithmetic mean of the separation distance as particles translate with the trajectories shown in Fig. 3.13(b).

3.2.4 Collection probability.

The collection probability can be defined as[74]

$$\eta = \frac{N_D}{N_{\text{tot}}}, \tag{3.7}$$

where N_{D} is the total number of particles deposited on the electrostatically heterogeneous, rough surface and $N_{\text{tot}} = 2000$ is the total number of particles released.

Direct simulations of particles trajectories flowing over surfaces with randomly located asperities are used to determine N_D. Plotting η vs. Θ provides collection probability curves that resemble particle deposition rate curves,[37,71,103] but the probability curves do not contain any rate information. The particle adhesion threshold, Θ_{crit}, is defined as the minimum value of Θ for which the collection probability is greater than zero and can be readily found from the collection probability curves. In all collection probability computations shown in Figs. 3.14(a) and 3.14(b), for a given value of Θ, the locations of the patches or pillars on the surface and the N_{tot} initial particle positions are identical for different pillar heights to isolate the influence of h_p on η.

Collection probability curves for various pillar heights are shown in Fig. 3.14(a). The adhesion threshold is lower for taller pillars, in qualitative accordance with extensive studies[42,64,67,110,113] that attribute increased particle adhesion rates, or lower overall energies of interaction, to surface roughness. As the pillar height decreases, the collection probability curve broadens. Particle adhesion on surfaces patterned with short pillars depends largely on whether or not the particle encounters a sufficiently large, locally attractive region as it translates. A few tall pillars, however, are shown to arrest particles effectively (e.g., the particle trajectory for $h_p = 5$ nm in Fig. 3.13(b)).

In Fig. 3.14(b), collection probability curves are shown for varying κ^{-1} at constant $h_p = 2$ nm. The curves shift to the right and the adhesion threshold increases for

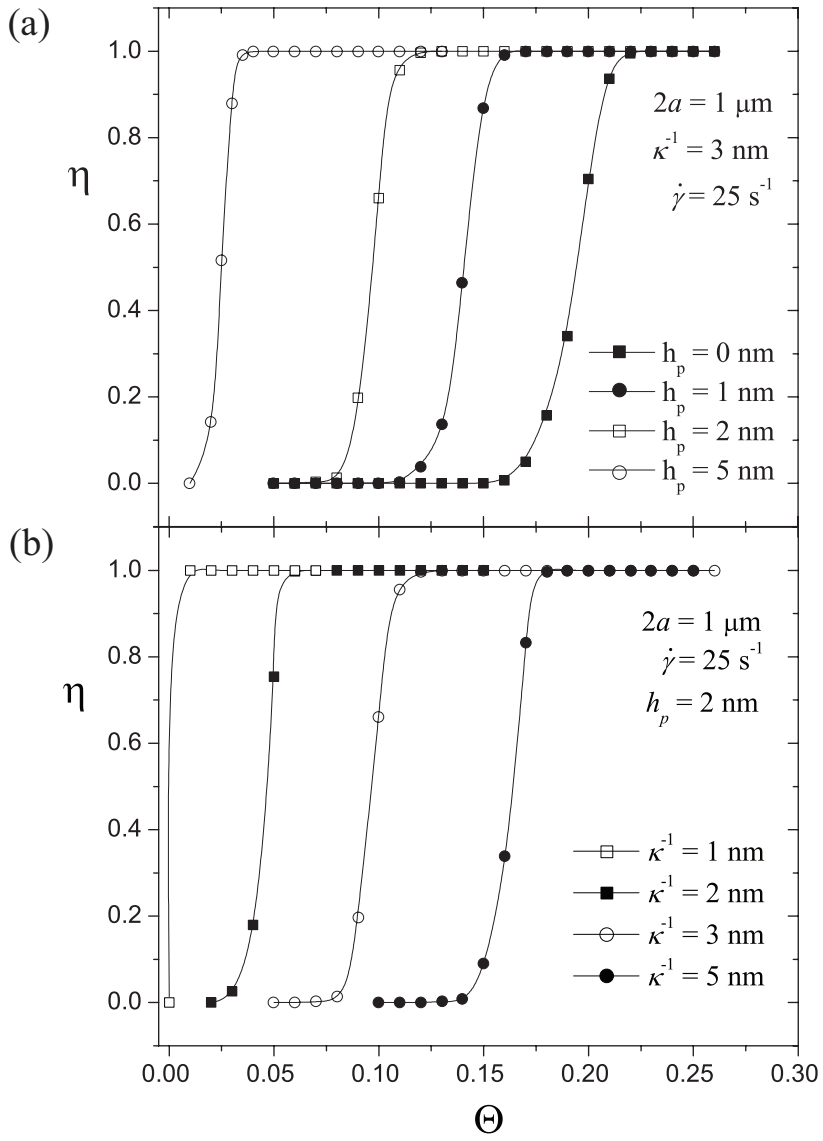

Figure 3.14. Collection probability curves for $1\,\mu m$ particles interacting with heterogeneous surfaces for (a) varying h_p and (b) varying κ^{-1}. The parameters are $\psi_{\text{pillar}} = 50$ mV, $\psi_{\text{surface}} = \psi_{\text{sphere}} = -25$ mV, $Pe = 14.31$, and $A_H = 5 \times 10^{-21}$ J.

larger values of κ^{-1}. As κ^{-1} is increased, the ZOI is larger, and the particles experience less localized interactions and more of the average (repulsive) surface charge. For $\kappa^{-1} = 1$ nm, all particles adhere for $\Theta = 0.01$ because the ZOI is small, corresponding to localized EDL interactions, and a few pillars are sufficient to adhere a particle.

3.2.5 Statistical model. Energy fluctuations.

From the $\mathrm{GSI_{UA}}$[14] model, derived in Sec. 3.1.5 as a mere reformulation of the GSI technique, the interaction energy between the particle and the heterogeneous collector is

$$U = \sum_{i=1}^{N} U_i = \sum_{i=1}^{N} \left[\mathrm{prob}(i = \mathrm{patch}) U_i^{\mathrm{att}} + \mathrm{prob}(i \neq \mathrm{patch}) U_i^{\mathrm{rep}} \right]. \tag{3.8}$$

This equation can be applied at any location on the surface (with the probability 1 or 0 for an ordered surface). The key step in the $\mathrm{GSI_{UA}}$ approach is recognizing that the probability that an element on the collector corresponds to a patch is identical to Θ, the fractional areal coverage of the collector by patches, and that each grid element on the collector is indistinguishable. This is true only for patches that are randomly distributed on the surface and small compared to the ZOI (so the analysis cannot proceed beyond Eq. (3.8) for ordered surfaces, such as stripes). For random surfaces,

$$\begin{aligned} U = \sum_{i=1}^{N} U_i &= \sum_{i=1}^{N} \left[\Theta U_i^{\mathrm{att}} + (1 - \Theta) U_i^{\mathrm{rep}} \right] \\ &= \Theta \sum_{i=1}^{N} U_i^{\mathrm{att}} + (1 - \Theta) \sum_{i=1}^{N} U_i^{\mathrm{rep}} \\ &= \Theta U^{\mathrm{att}} + (1 - \Theta) U_i^{\mathrm{rep}}. \end{aligned} \tag{3.9}$$

The mean particle-surface interaction can therefore be determined from a linear combination of two calculations involving uniform collectors: one with the surface poten-

tial of a patch (for U^{att}) and one with the potential of the underlying surface (for U^{rep}).

This model can be extended to predict the statistical variation of U over the heterogeneous collector by considering the statistical distribution of patches in the ZOI. The average number of patches (or pillars) in the ZOI is $N_{\text{avg}} = \Theta A_{\text{ZOI}}/A_{\text{patch}}$, where $A_{\text{ZOI}} = \pi R_{\text{ZOI}}^2$ and $A_{\text{patch}} = \pi d_p^2/4$. The number of patches in the ZOI is assumed to be randomly distributed following a Poisson distribution to model particle deposition experiments[81,103] in which the deposition of each new isolated patch is approximately independent of previously deposited patches. Although Θ can be small, the number of patches is sufficiently large ($N_{\text{patches, pillars}} > 1000$) that the Poisson distribution can be approximated by a normal distribution $N \sim (\mu = \sigma^2, \sigma)$. Within α standard deviations about the mean, the maximum (minimum) number of patches in the ZOI is given by

$$N_{\text{max/min}} = N_{\text{avg}} \pm \alpha\sqrt{N_{\text{avg}}}\,, \tag{3.10}$$

with $\Theta_{\text{max/min}} = \Theta N_{\text{max/min}}/N_{\text{avg}}$. The GSI_{UA} can then be used to calculate $U \pm \alpha$ standard deviations by replacing Θ by $\Theta_{\text{max/min}}$.

For a constant value of h_p, heterogeneous surfaces are generated with an appropriate statistical distribution of heterogeneities, and the standard GSI technique is used to compute U vs. D for $N_{\text{GSI}} = 1000$ distinct heterogeneous surfaces with $\Theta = 0.15$. A large number of surfaces (or surface locations) is required to ensure that the particle samples the statistical distribution of the patches. The arithmetic mean and standard deviation of the interaction energy is then computed for each separation distance D and plotted in Fig. 3.15. The mean of the N_{GSI} calculations is indistinguishable from the results of the simpler GSI_{UA} model, in agreement with previous results.[14] More significantly, there is excellent agreement between the results for $U \pm \sigma$ determined from the N_{GSI} calculations at different surface locations (for each κD) and the predictions of the statistical GSI_{UA} model with Θ replaced by $\Theta_{\text{max/min}}$. This simpler

statistical approach requires only 2 GSI calculations for homogeneous surfaces yet provides the same information as explicit computations with the N_{GSI} different locations on randomly heterogeneous surfaces. Furthermore, the computation of energy fluctuations for different values of the average surface coverage Θ does not require additional GSI energy-distance simulations. Instead, only the scaling factors Θ_{max} and Θ_{min} need to be recalculated.

3.2.6 Statistical model. Adhesion thresholds.

The prediction of adhesion thresholds is of considerable importance to experimental applications developed to control particle aggregation and deposition. In this section, the statistical model of Sec. 3.2.5 is used to predict adhesion thresholds, and excellent agreement is shown with the results of the particle trajectory simulations in Sec. 3.2.4.

To account for the most attractive regions on the surface, corresponding to the largest expected number of patches in the ZOI, Eq. (3.10) is applied with $\alpha = 3\sqrt{2}$ to determine N_{max}. The corresponding maximum surface coverage in a surface region the size of the ZOI is

$$\Theta_{\mathrm{max}} = \Theta \frac{N_{\mathrm{max}}}{N_{\mathrm{avg}}} = \Theta \left(1 + \alpha N_{\mathrm{avg}}^{-1/2}\right) . \tag{3.11}$$

The total interaction energy as a function of the distance D for $\Theta = \Theta_{\mathrm{max}}$ is then computed by applying the $\mathrm{GSI_{UA}}$ model. This calculation is simply a linear combination of interactions between the negatively charged sphere and homogeneous positively and negatively charged surfaces with weighting factor Θ_{max}. A representative energy-distance profile is shown in Fig. 3.16(a). The energy barrier (based on the maximum surface coverage Θ_{max}) is referred to as U_{max}. The maximum surface coverage Θ_{max} is then determined for other average coverages Θ, and U_{max} is determined for each Θ. These calculations simply require the interactions with homogenous surfaces (com-

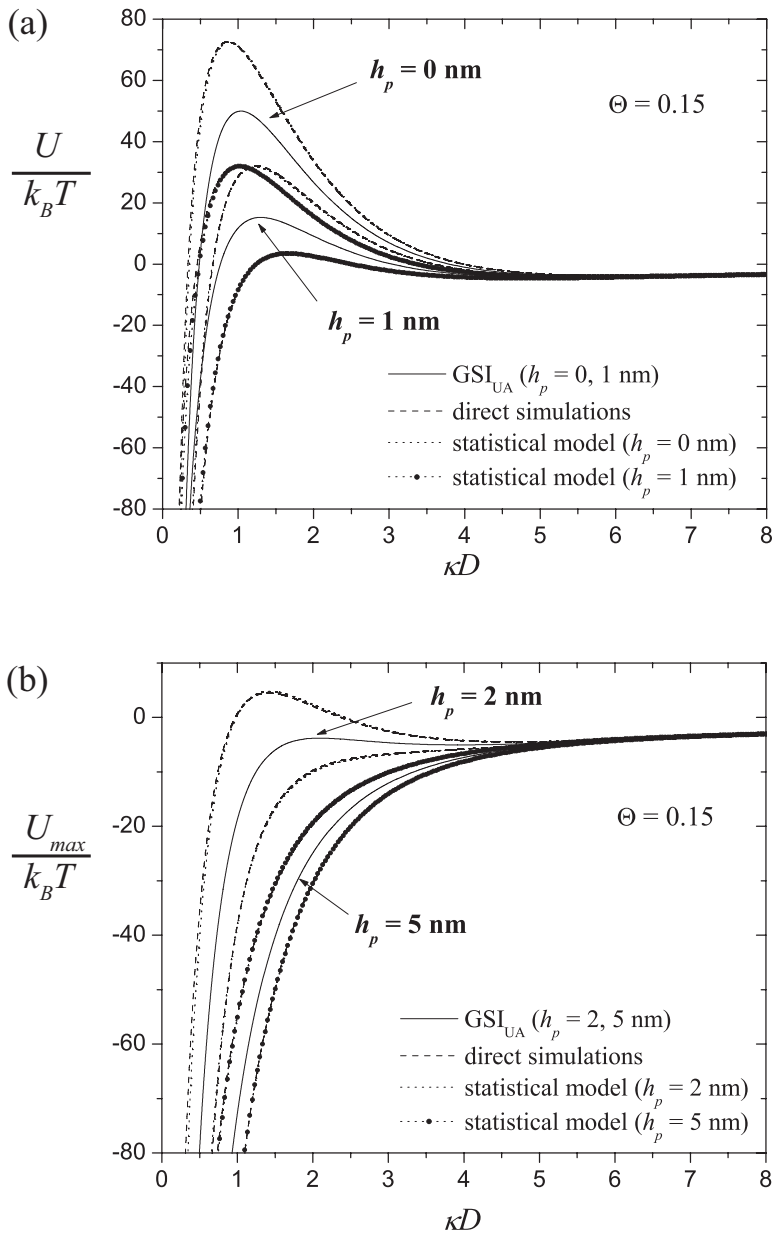

Figure 3.15. Mean potential energy of interaction (U) and its standard deviation ($U \pm \sigma$) vs. the normalized separation distance κD. Computed values for U from the $\mathrm{GSI_{UA}}$ model and the mean of 1,000 direct GSI calculations (for each κD) are indistinguishable (both marked with solid curves). Dashed lines indicate $U \pm \sigma$ determined from the 1,000 GSI calculations at different locations on the heterogeneous surface. Dotted lines are the $U \pm \sigma$ predictions of the $\mathrm{GSI_{UA}}$ model that requires only 2 GSI calculations for homogeneous surfaces (for each κD). The parameters are $a = 0.5\,\mu$m, $\kappa^{-1} = 3$ nm, $A_H = 5 \times 10^{-21}$ J, $\psi_{\mathrm{sphere}} = \psi_{\mathrm{surface}} = -25$ mV, and $\Psi_{\mathrm{patch/pillar}} = 50$ mV.

puted just once) to be scaled by the statistically determined $\Theta_{\max}$ values, each of which is determined for a specified Θ. The adhesion threshold Θ_{crit} is the value of Θ at which the energy barrier vanishes.

In Fig. 3.16(b), the decrease of $U_{\max}$ with increasing Θ is shown for various h_p. It is seen that the addition of pillars only a few nanometers high significantly reduces the energy barrier and the adhesion threshold (indicated by arrows).

The adhesion thresholds determined from this statistical approach are compared in Table 3.1 to the values obtained by direct simulations in Sec. 3.2.4. The agreement is excellent in all of the cases considered. For $h_p = 0\,\text{nm}$ and $\kappa^{-1} = 3\,\text{nm}$, the values of Θ limiting the adhesion threshold differ in less than 1%. The decrease of the adhesion threshold with increasing h_p is due to stronger attractive interactions with small numbers of tall pillars, which effectively enhance particles deposition.

(a) h_p [nm]	Sims.	GSI_{UA}	**(b)** κ^{-1} [nm]	Sims.	GSI_{UA}	**(c)** A_H [10^{-21} J]	Sims.	GSI_{UA}
0	0.16	0.15	1	0.01	0.01	1	0.10	0.10
1	0.10	0.10	2	0.03	0.03	5	0.07	0.07
2	0.07	0.07	3	0.07	0.07	8	0.06	0.06
5	0.02	0.02	5	0.13	0.13	12	0.04	0.04

Table 3.1. Agreement between direct simulations (Sims.) of particle trajectories for $2a = 1\,\mu\text{m}$ particles with $\psi_{\text{patch/pillar}} = 50$ mV, $\psi_{\text{sphere}} = \psi_{\text{surface}} = -25$ mV and $\dot{\gamma} = 25\,\text{sec}^{-1}$, and the GSI_{UA} statistical model. The values of the critical surface coverage required for particle adhesion (Θ_{crit}) are shown as a function of the (a) nano-pillar height, with $\kappa^{-1} = 3$ nm and $A_H = 5 \times 10^{-21}$J, (b) Debye length, with $h_p = 2\,\text{nm}$ and $A_H = 5 \times 10^{-21}$J, and (c) Hamaker constant, with $\kappa^{-1} = 3$ nm and $h_p = 2\,\text{nm}$.

The proposed statistical model can easily accommodate variations in the parameters that define the colloidal interactions, such as the Debye length κ^{-1} and the Hamaker constant A_{H}. The results presented in Table 3.1 show a complete agreement between the direct simulations and the predictions of the statistical model, for varying values of κ^{-1} and A_H. The adhesion threshold increases with larger κ^{-1} not only due to stronger electrostatic repulsions at a fixed separation distance but also

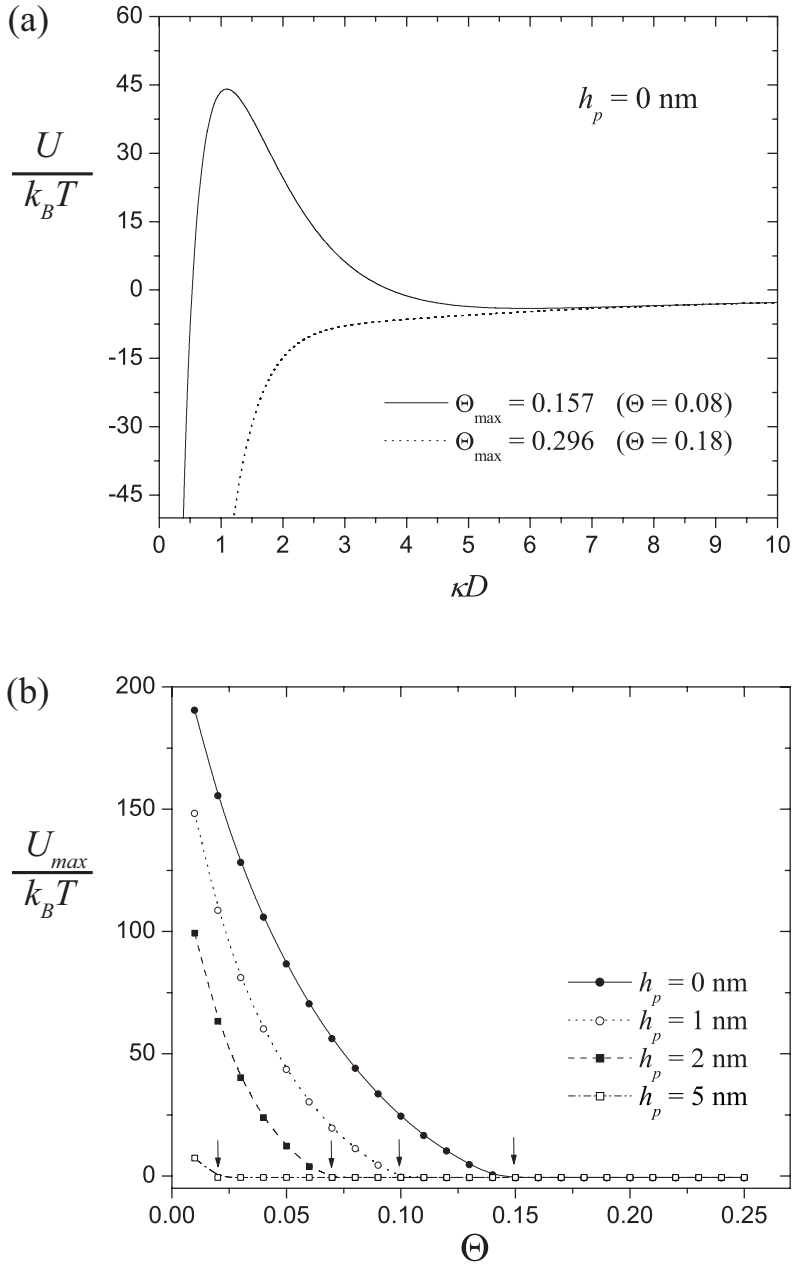

Figure 3.16. Energy-averaging statistical model for system parameters $a = 0.5\,\mu$m, $\kappa^{-1} = 3$ nm, $A_H = 5 \times 10^{-21}$ J, $\psi_{\text{sphere}} = \psi_{\text{surface}} = -25$ mV, and $\psi_{\text{patch/pillar}} = 50$ mV. (a) U vs. κD from the GSI_{UA} model for $\Theta_{\max} = 0.157$ and $\Theta_{\max} = 0.296$, which correspond to $\Theta = 0.08$ and $\Theta = 0.18$ respectively. (b) Dependence of $U_{\max}$ on Θ for various h_p. $U_{\max}$ is the energy barrier of energy-distance profiles, such as that shown in (a), obtained with the GSI_{UA} method and $\Theta_{\max}$. The adhesion threshold Θ_{crit}, determined by the value of the average surface coverage Θ for which $U_{\max}$ vanishes and marked by an arrow, increases as h_p decreases.

because the ZOI increases for larger κ^{-1}, such that the particle feels more of the average (repulsive) interaction from the heterogeneous surface. The adhesion threshold decreases for stronger van der Waals attractions, represented by larger values of A_H.

Some flow-rate dependence can be imbedded in the parameter α. For larger shear rates, corresponding to a reduced interaction time between a particle and surface feature, adhesion is governed by an effective zone of interaction that is larger than the ZOI and more elongated. The influence of shear rate could be incorporated into α. It is seen from Eqs. (3.10) and (3.11) that if the radius of the ZOI is increased by a factor a, $R'_{\mathrm{ZOI}} = aR_{\mathrm{ZOI}}$, then α is reduced: $\alpha' = \alpha/a$, which corresponds to a smaller value for $\Theta_{\max}$. A larger value of Θ is therefore required to attain the same value of $\Theta_{\max}$ for smaller α, which corresponds to an increase in the adhesion threshold with the shear rate, in qualitative agreement with experiments.[71]

The surface loading at which a heterogeneous surface becomes net-attractive is denoted by $\overline{\Theta}$ and defined as the average loading of patches for which the energy barrier towards adhesion vanishes. It is thus given implicitly by $U_{\max}(\Theta = \overline{\Theta}) = 0$ and can determined from Eq. (3.9). Plots of $\overline{\Theta}$ vs. κ^{-1} for representative particle sizes and surface potentials are included in Fig. 3.17. It is seen that the effective surface loading, $\overline{\Theta}$, increases monotonically with the Debye length but does not vary significantly with the particle size. The lower adhesion threshold observed for smaller particles[103] is therefore due primarily to the smaller ZOI, which makes the particles more sensitive to local hot spots on the surface.

For a patchy surface, the maximum number of patches that can be located within the ZOI is $N_{\mathrm{tot}} = A_{ZOI}/A_p$, where A_p is the area of one patch. The average number of patches within the ZOI is then defined as $N_{\mathrm{avg}} = \Theta\, A_{\mathrm{ZOI}}/A_{\mathrm{p}}$. In combination with Eq. (3.11), $\Theta_{\max}$ is expressed as

$$\Theta_{\max} = \Theta \left[1 + \alpha \left(\Theta \frac{A_{\mathrm{ZOI}}}{A_{\mathrm{p}}} \right)^{-1/2} \right] . \tag{3.12}$$

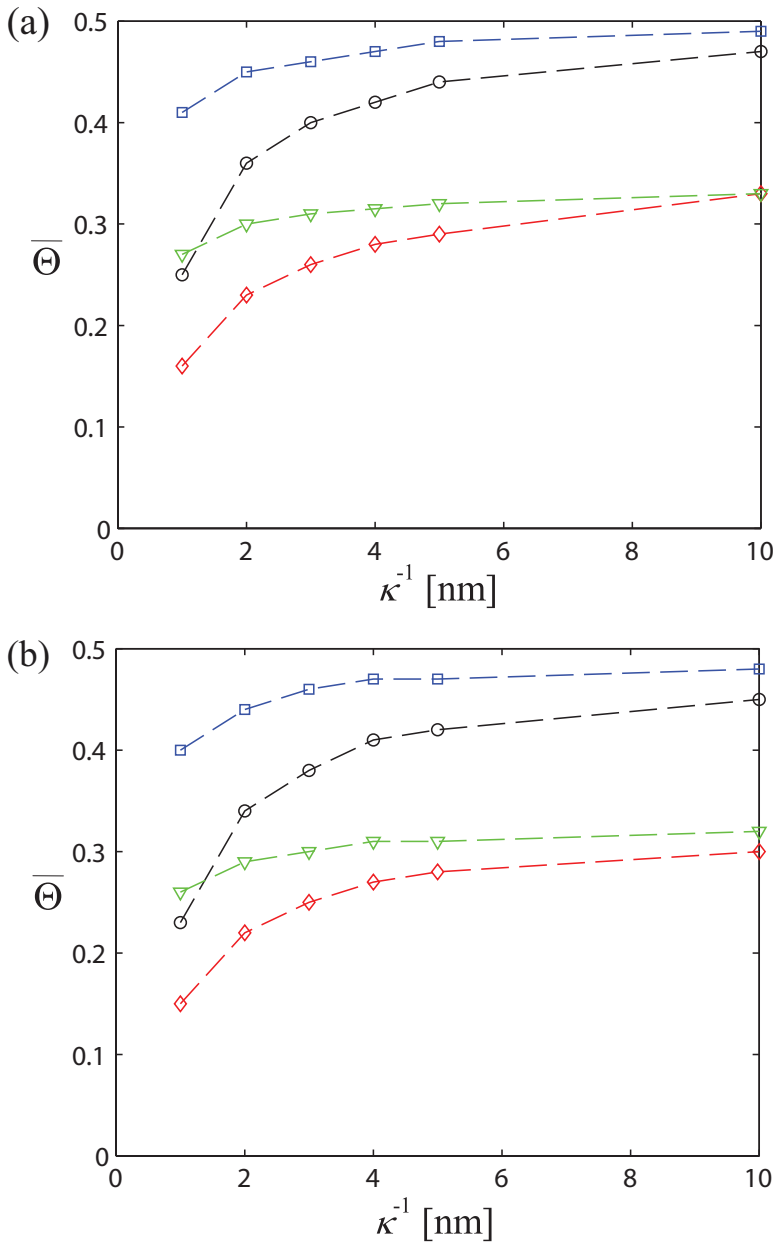

Figure 3.17. Effective surface loading $\overline{\Theta}$ when the energy barrier vanishes for a uniform surface plotted against the Debye length κ^{-1} for a particle of diameter (a) $2a = 100\,\text{nm}$ and (b) $2a = 1\,\mu\text{m}$ for ψ_p/ψ_s [mV] $= +25/-25$ (circles), $+50/-50$ (squares), $+50/-25$ (diamonds), and $+100/-50$ (triangles).

The limit in which the maximum surface loading of patches within the ZOI, $\Theta_{\max}$, can be approximated by the surface loading that defines a net attractive surface, $\overline{\Theta}$, is expressed as $\Theta_{\max} \simeq \overline{\Theta}$. In this case, $\Theta = \Theta_c$ because the adhesion threshold is defined as the surface loading at which the energy profile computed with Eq. (3.9) and $\Theta = \Theta_{\max}$ does not exhibit an energy barrier. Therefore,

$$\overline{\Theta} \approx \Theta_{\max} = \Theta_c + \alpha \sqrt{\frac{\Theta_c A_p}{A_{ZOI}}}\,, \tag{3.13}$$

where $\Theta_{\max}$ is given by Eq. (3.12). Solving for Θ_c provides an approximation for the adhesion threshold,

$$\Theta_c^{1/2} = -\frac{\alpha}{2}\sqrt{\frac{A_p}{A_{ZOI}}} + \sqrt{\frac{\alpha^2 A_p}{4A_{ZOI}} + \overline{\Theta}}\,. \tag{3.14}$$

For particles being transported over the surface in a shear flow, the effective zone of interaction can be approximated as

$$A_{ZOI} = A_{ZOI,0} + C_h\,\dot{\gamma}\,R_{ZOI}, \tag{3.15}$$

where $A_{ZOI,0}$ is the zone of influence in the absence of fluid flow and C_h is a hydrodynamic constant similar to the parameter introduced by Adamczyk et al.[5]

It is seen from Fig. 3.18 that Θ_c increases with A_{ZOI}, with $\Theta_c \to \overline{\Theta}$ as $A_{ZOI}/Z_{ZOI,0} \to \infty$. As the effective interaction area becomes large, the particle-wall interactions therefore asymptote to those for uniform surfaces, and the effects of heterogeneity are lost. As α is increased, Θ_c decreases for small A_{ZOI} because adhesion is sensitive to local fluctuations in the patch density.

Equations (3.14) and (3.15) can be applied for the parameters reported by Kalasin and Santore,[71] who studied the influence of shear rate on dynamic microparticle adhesion on electrostatically patchy surfaces. The constants α and C_h are treated as

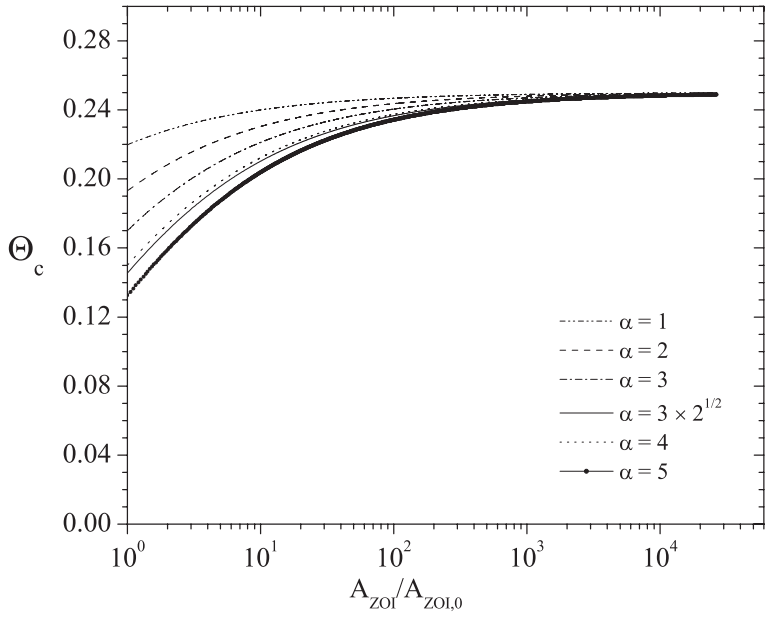

Figure 3.18. Adhesion threshold (Θ_c) for varying α as a function of the areas ratio $A_{\mathrm{ZOI}}/A_{\mathrm{ZOI},0}$. Other parameters are $a = 500\,\mathrm{nm}$, $d_p = 10\,\mathrm{nm}$, $h_p = 0\,\mathrm{nm}$, $\overline{\Theta} = 0.25$, $\kappa^{-1} = 3\,\mathrm{nm}$, $A_H = 5{\times}10^{-21}\,\mathrm{J}$.

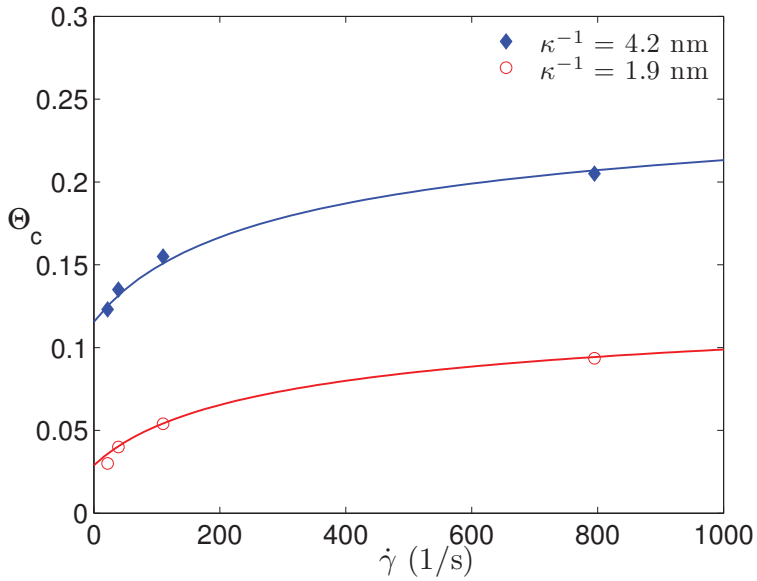

Figure 3.19. Adhesion threshold Θ_c plotted against the shear rate $\dot{\gamma}$. The lines are the theoretical predictions, and the symbols are the experimental data from Figure 3 of Kalasin and Santore.[71]

fitting parameters. As seen from Fig. 3.19, the predicted variation of the adhesion threshold with the shear rate is in good agreement with the experimental results. Such agreement is surprising given the simplicity of the model but supports the argument that an increase in the shear rate raises the adhesion threshold not only because of the enhanced hydrodynamic force and torque on a particle,[51] which could overcome local adhesive forces, but also because of the increased size of the zone of interaction for dynamic adhesion, which diminishes the influence of small-scale heterogeneity.

3.2.7 Conclusion.

A statistical model was introduced to calculate DLVO interactions between particles and patchy collectors with nanoscale electrostatic and topographical heterogeneity. The patches are randomly distributed on the collector and create localized attractive regions on an otherwise repulsive surface. In this approach, the statistical distribution of patches is combined with DLVO calculations between a particle and two homogeneous surfaces: one with the surface potential of the patches and one with the potential of the underlying collector surface. These surface potentials could be obtained in experiments from zeta potential measurements for the bare collector and for one that is saturated with polyelectrolyte patches. Predictions of the mean interaction energy and its variance as a particle samples the collector are in excellent agreement with the mean and variance of many DLVO calculations for interactions with a heterogeneous collector.

With an appropriately defined zone of influence for the electrostatic-double-layer interactions, the statistical model can predict adhesion thresholds corresponding to the critical surface loading of patches at which particles begin to adhere from flowing solution. These predictions are indistinguishable from the results of computed particle trajectories over heterogeneous surfaces but require only simple DLVO calculations involving homogeneous surfaces that are similar in complexity to a standard,

mean-field application of classical DLVO theory. This approach is relevant to studies of particle interaction and deposition onto heterogeneous collectors, particularly those with adsorbed polyelectrolyte patches, and the model successfully predicts the increase in the adhesion threshold with the shear rate of the flowing suspension observed in experiments.[71]

The results of the statistical model reveal several reasons that patchy surfaces are more attractive toward microparticles than expected. Classical DLVO theory is typically applied with calculations based on a mean (apparent) surface potential, such as the zeta potential measured from electrophoretic mobility or streaming potential experiments, which typically has the same sign as that of the particles when the patch coverage is sparse. A group of patches in close proximity can create a local hot spot capable of capturing a particle, as noted in many studies.[9,37,81,103] In addition, the mean interaction between the heterogeneous collector and microparticle is less repulsive than predicted by classical DLVO theory because of the random distribution of nanoscale, cationic patches (vs. treating the surface charge as uniformly smeared out over the surface). Furthermore, at moderate and large ionic strength, deposition is enhanced significantly if the patches protrude only slightly from the collector.

3.3 Brownian motion effects.

3.3.1 Introduction.

As described in previous sections, recent studies of particles flowing over collectors patterned with nanoscale patches, which are orders of magnitude smaller than the depositing particles, revealed that small amounts of randomly-distributed, attractive patches induce particle deposition onto net-repulsive surfaces.[37,39,71,81,103] Deposition rates for such systems are found to be larger than expected from a mean-field application of the classical DLVO theory.[14] The discrepancies between empirical and predicted results are attributed to particle interactions with many patches, which

create locally attractive regions ("hot spots")[38] on the collector as a result of their non-uniform distribution.

Therefore, particle deposition on collectors patterned with nano-scale heterogeneity is found to be controlled not only by the total amount of attractive charge on the collector, but also, by the spacing between the particle-attracting patches. For surfaces densely covered by patches (small patch-patch spacing), adhesion is rapid and transport-limited. For larger patch-patch spacing, however, adhesion rates become slower and the amount of deposited particles also decreases.[71] The dependence of the adhesion capability of the collector on the patch-patch spacing is thus better characterized by the system's adhesion threshold. The adhesion threshold is usually defined as the critical fraction of collector surface area covered with heterogeneity below which particles do not adhere on the collector. Alternatively, it can be defined as the critical patch-patch spacing above which silica particles do not deposit on the collector.[81,103]

In theoretical and computational studies[37–39] of such systems, comprising flat and spherical electrostatically non-uniform collectors in which particles deposit from a flowing solution, Brownian motion effects have typically been neglected. The displacements of free particles due to Brownian motion, however, are often significant in time intervals characteristic of the imposed flow. Brownian motion can enable particle deposition on both homogeneous and heterogeneous collecting surfaces, even in the presence of an energy barrier.[2,118]

While adhesive dynamic simulations[91] showed that bond dissociation dynamics are not significantly influenced by Brownian forces and recent studies on particle interactions with rough collectors[74] also indicated that Brownian motion effects are negligible, microchannel flow experiments of particle deposition[114] suggest that, for low-energy barrier systems, Brownian motion can indeed increase particles' tendency to adhere on heterogeneous collectors.

Brownian motion effects are modeled in this work through the introduction of stochastic *Brownian displacements* in the Langevin-type particle trajectory equations.[12,44,74,114,119] Alternatively, Brownian motion effects have also been modeled by computing *Brownian forces*.[24,91] This empirical approach is briefly described in the Appendix A.

Previous work focused on the study of the dynamics and aggregate formation properties of many-particle systems,[12,44] on particle deposition on homogeneous collectors[74] or on particle behavior in parallel-plate microchannel flow.[114] In this study, Brownian motion effects are investigated for the case of a spherical particle interacting with collectors patterned with nanoscale heterogeneity.

Results presented in this section intend, therefore, to elucidate the specific effects of Brownian motion on particle interactions with collectors patterned with flat circular patches or with cylindrical pillars that protrude a few nanometers from the collector. As described in Secs. 3.1 and 3.2, the model systems resemble experimental set-ups used to study deposition mechanisms of colloidal particles, such as latex spheres that deposit on substrates covered with disk-shaped or spherical adsorption sites,[2] or silica particles that adhere from flowing solution on patterned planar collectors.[81,103]

Particle trajectories are presented in Sec. 3.3.3 for particles that translate and rotate in shear flow over heterogeneous collectors, being subject not only to DLVO interactions with the nano-scale collector heterogeneity but also to Brownian motion effects. Electrostatic double layer (EDL) and van der Waals (vdW) forces and energies (DLVO interactions) are computed by implementing the GSI technique.[14,38] The shear-induced force and torque acting on the particle as it translates over a collector and the DLVO forces that result from particle interactions with it, are incorporated in the mobility matrix[26] formulation described in Sec. 2.8 to yield the particle's velocities. Brownian motion effects are modeled by updating the particle's position with stochastic Brownian displacements.[74] In Sec. 3.3.4, the relative importance of shear,

colloidal, and Brownian effects is evaluated through the computation of appropriate Péclet numbers, which are unique for this heterogeneous system. Conclusions are presented in Sec. 3.3.5.

3.3.2 Methods.

The model system, schematically illustrated in Fig. 3.20, depicts a colloidal particle of radius a translating in shear flow parallel to a chemically and topographically heterogeneous collector. The collector heterogeneities are located at randomly chosen positions, to satisfy Poisson statistics as a first approximation of distributions of patches attained in experiments.[37] The fraction of surface area of the collector covered with heterogeneities is denoted by Θ. The heterogeneities consist on either flat patches (with pillar height $h_{\mathrm{p}} = 0$ nm) or cylindrical pillars ($h_{\mathrm{p}} = 2$ nm) that are charged with an electrostatic surface potential of $\psi_{\mathrm{patch,\,pillar}} = 50$ mV. The surface potential of the bare collector and of the flowing particle are $\psi_{\mathrm{sphere}} = \psi_{\mathrm{collector}} = -25\,\mathrm{mV}$.

Brownian motion effects are modeled by introducing Brownian displacements[41,74,92] in the parallel and normal directions to the collector surface. This approach parallels the Brownian Dynamics method[12,44,119] and yields a Langevin-type equation for the particle trajectory.

In the results presented in this section, the general form of such equation reads

$$\mathbf{x}(t) = \mathbf{x}^{o}(t) + \mathbf{U}\Delta t + \mathbf{R}_{\mathrm{Br}}\,, \tag{3.16}$$

where $\mathbf{x}(t) = (x, y)^t$ is the particle position vector, and the superscript ^{o} refers to the initial or previous condition. The particle translational and rotational velocities vector $\mathbf{U} = (V_x\, V_y\, V_z\, \Omega_x\, \Omega_y\, \Omega_z)^t$ is calculated from a mobility matrix formulation of the hydrodynamics problem,[26,38]

$$\mathbf{U} = \mathbf{M}\,\mathbf{F}\,, \tag{3.17}$$

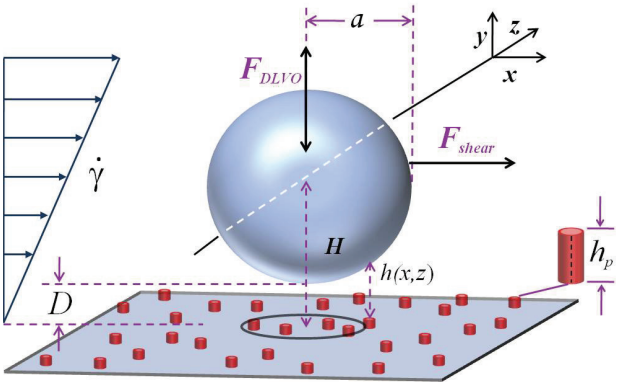

Figure 3.20. Schematic diagram of a spherical particle of radius a interacting with a heterogeneous surface patterned with randomly distributed nano-pillars of height h_{p}. The local separation distance between the sphere and the collector element vertically below is $h(x,z)$ and D is the minimum separation distance between the sphere and the plane defined by the top of the pillars. Shear-induced and colloidal forces act in the directions parallel and normal to the collector, respectively.

where $\mathbf{F} = (F_x\, F_y\, F_z\, T_x\, T_y\, T_z)^t$ is the vector of all external forces and torques acting on the spherical particle, and $\mathbf{M}$ is a 6 x 6 matrix comprising hydrodynamic functions.[21,38,50,51,69] Eq. (3.17) is mere a reformulation of Eq. (2.25).

The last term in the rhs in Eq. (3.16) is included to model Brownian motion effects. Non-zero Brownian displacements are defined as[41,74,92]

$$\mathbf{R}_{\mathrm{Br}} = \begin{pmatrix} R_{\mathrm{Br}_x} \\ R_{\mathrm{Br}_y} \end{pmatrix} = \begin{pmatrix} R_{\mathrm{Br}_\parallel} \\ R_{\mathrm{Br}_\perp} \end{pmatrix} = \sqrt{2D_\infty dt} \begin{pmatrix} \sqrt{f_4} \\ \sqrt{f_1} \end{pmatrix} \hat{\lambda}, \tag{3.18}$$

where the vector $\hat{\lambda}$ contains random numbers of the normal standard distribution, dt is the time step, $D_\infty = (k_{\mathrm{B}}T)/(6\pi\mu a)$ is the Stokes-Einstein diffusivity, and μ the fluid viscosity. The functions

$$f_1 = 1.0 - 0.3990\exp(-0.1487\,D) - 0.6010\exp[-1.202\,(D^{0.9267})] \tag{3.19}$$

and

$$f_4 = 1 - 2.6760\exp(-0.3581\,D) + 1.9990\exp[-0.2320\,(D^{1.2600})]\,, \qquad (3.20)$$

are universal correction functions (UCFs) that account for hydrodynamic effects and depend solely on the minimum particle-surface separation distance D.[74] The time step used in all the results that follow is $dt = 1 \times 10^{-5}$ sec.

3.3.3 Effects of particle size and pillar height.

The influence of Brownian motion on particle dynamics is expected to vary most significantly with system properties such as particle size and collector topography. Trajectories of small ($a = 0.1\,\mu$m) and large ($a = 1\,\mu$m) particles flowing over patchy ($h_{\rm p} = 0\,$nm) and pillared ($h_{\rm p} = 2\,$nm) collecting surfaces are shown in Fig. 3.21, as plots of the dimensionless separation distance κD^* vs the horizontal dimensionless displacement κx. D^* denotes the minimum particle-flat collector separation distance and is defined as $D^* = D + h_{\rm p}$. For both pillared and patchy collectors, the mobility matrix hydrodynamic functions in Eq. (3.17) were computed with Eqs. (2.46)-(2.49) at the separation distance $h^* = a + D^*$, while the UCFs $f1$ and $f4$ in Eqs. (3.19)-(3.20) were calculated at the separation distance $h^* = D^*$. Trajectories presented in Fig. 3.21 are computed by either neglecting Brownian motion effects or by including them as Brownian displacements.

The spatial fluctuations observed in the dynamic profiles of large particles interacting with patchy and pillared collectors (Figs. 3.21(a)-(b)) are due to interactions between the flowing particle and both the attractive and repulsive collector surface elements. The attractive interactions are not strong enough to capture the particle on the surface, and the particle continues to flow until it reaches the edge of the simulated collector, given by a horizontal distance of 24.2 μm. Interactions of small particles flowing over patchy and pillared collectors (Figs. 3.21(c)-(d)), however, depict in all cases trajectories of particles that adhere on the collector. For the case of a small particle interacting with a patchy collector (Fig. 3.21(c)), trajectories computed by

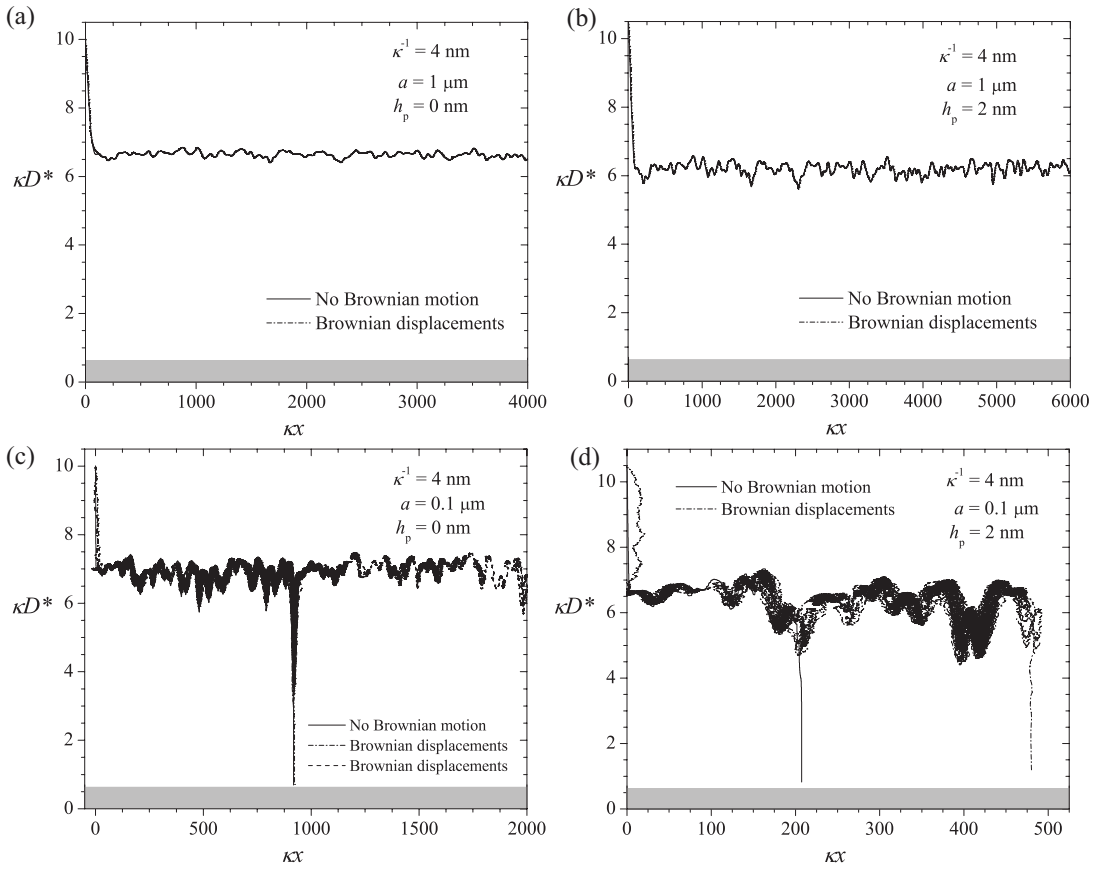

Figure 3.21. Trajectories of particles interacting in shear flow with surfaces patterned with randomly located flat patches or cylindrical pillars with a surface area coverage of $\Theta = 0.12$. Other simulation parameters are: $\dot{\gamma} = 25$ sec^{-1}, $A_H = 5 \times 10^{-21}$ J, $\psi_{\text{sphere}} = \psi_{\text{collector}} = -25$ mV, $\psi_{\text{patch}} = 50$ mV. In each plot, trajectories are obtained by either neglecting Brownian motion effects or by incorporating them in the computations as Brownian displacements. (a) $a = 1\,\mu$m particles interacting with patchy surfaces ($h_p = 0$ nm). (b) $a = 1\,\mu$m particles interacting with pillared surfaces ($h_p = 2$ nm). (c) $a = 0.1\,\mu$m particles interacting with patchy surfaces ($h_p = 0$ nm). Two trajectories are shown for the case of Brownian displacements (dashed and dash-dotted lines). (d) $a = 0.1\,\mu$m particles interacting with pillared surfaces ($h_p = 2$ nm).

including Brownian displacements can also describe non-adhering particles, which, instead, continue to flow and translate over the entire simulated collector.

The total DLVO energy of interaction for large ($a = 1\,\mu$m) and small ($a = 0.1\,\mu$m) particles interacting with collectors patterned with flat patches ($h_{\mathrm{p}} = 0\,$nm) or cylindrical pillars ($h_{\mathrm{p}} = 2\,$nm) at a fixed surface area coverage of $\Theta = 0.12$ is computed with the $\mathrm{GSI_{UA}}$ technique,[14] described in Sec. 3.1.5, and results are presented in Fig. 3.22(a).

As shown in Fig. 3.22(a), the total energy of interaction for large ($a = 1000$ nm) particles interacting with patchy ($h_{\mathrm{p}} = 0$ nm) and pillared ($h_{\mathrm{p}} = 2$ nm) collectors presents high energy barriers, of about 175 $k_{\mathrm{B}}T$ and 50 $k_{\mathrm{B}}T$, respectively. The small ($a = 100$ nm) particles' energy profiles, however, present much lower energy barriers, of about 5 $k_{\mathrm{B}}T$ for the case of the pillared ($h_{\mathrm{p}} = 2$ nm) collector and about 17 $k_{\mathrm{B}}T$ for the case of the patchy collector ($h_{\mathrm{p}} = 0$ nm). As previously noted, in the case of a small particle interacting with a patchy collector (Fig. 3.21(c)), trajectories obtained with Brownian displacements for a surface coverage of $\Theta = 0.12$ either indicate that the particle flows until it reaches the collector's edge or show particle adhesion. Results obtained when Brownian motion is neglected, however, only yield trajectories that denote particle adhesion. For the case of a small particle interacting with a patchy collector, therefore, Brownian effects become more prominent and influence the particle's tendency to adhere on the collector as a direct consequence of the intermediate magnitude of the energy barrier, of about 17 $k_{\mathrm{B}}T$.

Heterogeneous collectors can be characterized by energy contour plots, as those shown in Figs. 3.22(b)-(c), for $2a = 200$ nm and $2a = 2\,\mu$m diameter particles, respectively. An heterogeneous collector is sampled such that, at each collector areal element, the DLVO energy-distance profile is computed with the GSI technique when the particle's center projection on the xz-plane is positioned at the center of the discrete collector element. Thus, for each collecting surface element at which the particle

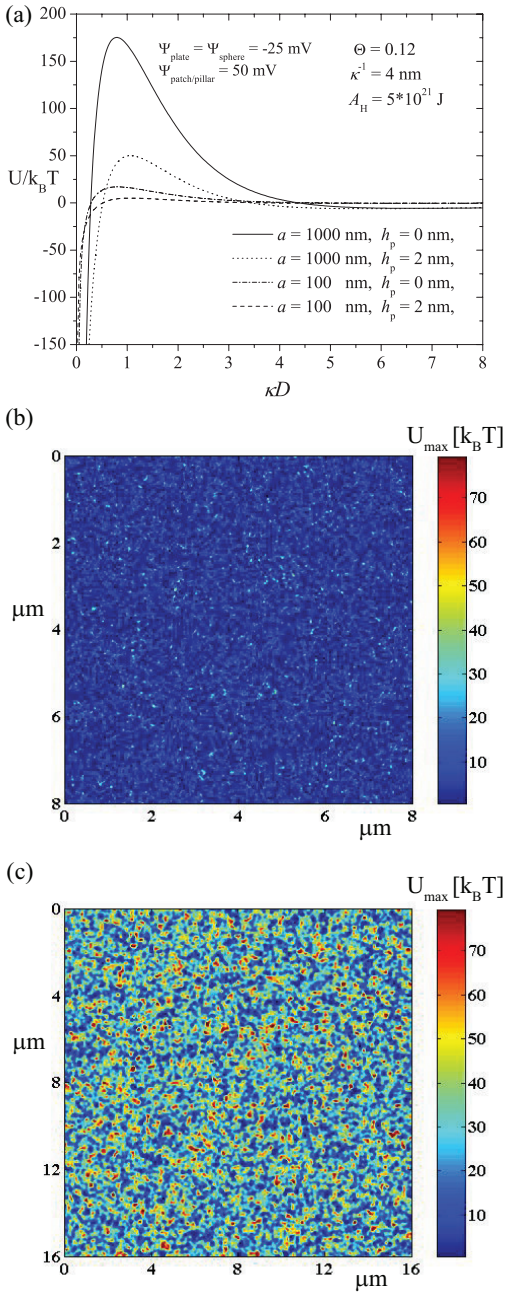

Figure 3.22. (a) Total DLVO energy of interaction obtained with the $\mathrm{GSI_{UA}}$[14] technique for large ($a = 1\,\mu$m) and small ($a = 0.1\,\mu$m) particles interacting with collectors patterned with flat patches ($h_\mathrm{p} = 0$ nm) or cylindrical pillars ($h_\mathrm{p} = 5$ nm) with a surface area coverage of $\Theta = 0.12$. (b)-(c) Energy profiles for $2a = 200$ nm (b) and $2a = 2\,\mu$m (c) particles interacting with a patchy collector ($h_\mathrm{p} = 0$ nm, $\Theta = 0.22$). The fractions of the collector that are favorable for adhesion (i.e. $U < k_\mathrm{B}T$) are 32% for the $2a = 200$ nm (b) particle and 2.8% in the case of the $2a = 2\,\mu$m (c) particle.

center is located, a different energy-distance profile is obtained due to interactions with different regions of the heterogeneous surface. The magnitude of the energy barrier (U_{MAX}) is stored for each heterogeneous surface element, and these values are color-scaled to yield an energy-contour plot that highlights the various attractive and repulsive regions within the collector. Surface elements for which there is no energy barrier are assigned the value $U_{MAX} = 0$. A dark blue color denotes the lowest values of the energy barrier (more attractive regions) while the regions with the highest values of the energy barrier (more repulsive areas) are marked with a dark red color. Intermediate values are scaled with other colors, as indicated in the color scale in Figs. 3.22(b)-(c).

To isolate the specific influence of Brownian displacements on the small particle's ($2a = 200$ nm) tendency to adhere on the patchy ($h_p = 0$ nm) collector, a few thousand simulations of particle trajectories were performed for a few values of the collector heterogeneity coverage Θ. At a fixed value of Θ, all trajectories are simulated with the same collector surface, and in all cases, the particles are released from the same initial height of $D = 40$ nm. The shear flow rate is $\dot{\gamma} = 25$ sec^{-1} and the colloidal interactions are defined by the Hamaker constant $A_H = 5 \times 10^{-21}$ J and the Debye screening length $\kappa^{-1} = 4$ nm.

From the direct simulation of particle trajectories, the probability of particle adhesion due to Brownian motion effects P_{Br} is defined as

$$P_{Br} = \frac{N_D}{N_{tot}}, \tag{3.21}$$

where N_D is the total number of particles deposited on the patchy collecting surface and N_{tot} is the total number of particles released.

Though defined in the same way as the particle deposition probability computed in recent studies[74] and described in Sec. 3.2.4, the particle adhesion probability defined in Eq. (3.21) differs qualitatively from previous definitions. For a fixed value of the

surface area coverage Θ, P_{Br} is obtained from trajectories of particles translating over *one* collecting surface, and the many trajectories differ only in the random numbers that characterize the Brownian effects. At each adhesion attempt, *one* particle is released and allowed to interact with the heterogeneous collector in shear flow. The simulation runs are independent, such that the collector is patterned with randomly distributed cationic patches only, and previously adhered colloidal particles are not considered.

For the case of a small particle ($2a = 200\,\mathrm{nm}$) interacting with a patchy ($h_{\mathrm{p}} = 0\,\mathrm{nm}$) collector, P_{Br} values were computed for a range of values of Θ, $0.10 \leq \Theta \leq 0.15$. To obtain more statistically relevant predictions, Wilson score intervals[121] that include the *actual* values of the adhesion probability are constructed based on the estimates given by Eq. (3.21). Wilson score intervals represent an improvement with respect to the normal approximation intervals and are used in this work due to their high accuracy even for a small number of trials and extreme probabilities. The Wilson score interval is defined as

$$\frac{\hat{p} + \frac{1}{2n} z_{1-\alpha/2}^2 \pm z_{1-\alpha/2} \sqrt{\frac{\hat{p}\,(1-\hat{p})}{n} + \frac{z_{1-\alpha/2}^2}{4n^2}}}{1 + \frac{1}{n} z_{1-\alpha/2}^2} \tag{3.22}$$

where $\hat{p}$ is the probability estimate, n is the sample size, and $z_{1-\alpha/2}$ is the $(1-\alpha/2)$ percentile of a standard normal distribution with an α error percentile.

Adhesion probability values are thus obtained as series of intervals computed from Eq. (3.22), with an arbitrarily chosen 95% confidence interval ($\alpha = 0.05$), such that $z_{1-\alpha/2} = 1.96$. The sample size is $n = N_{\mathrm{total}}$ and the probability estimate $\hat{p} = P_{\mathrm{Br}}$ is obtained from Eq. (3.21). The specific number of trajectory simulations for each P_{Br} data point therefore varied between $N_{\mathrm{tot}} = 6{,}200$ and $N_{\mathrm{tot}} = 10{,}000$, such that the difference between either end of the interval and the interval center is lower than 1.5%.

The spread of the Brownian motion-induced adhesion probabilities can be quantified by the difference

$$\Delta\Theta = \Theta_{P_{max}} - \Theta_{\mathrm{C}}\,, \tag{3.23}$$

where

$$\Theta_{P_{max}} = \Theta(P_{\mathrm{Br}_i} = 1), \quad \forall\ i \in [1, N_{\mathrm{tot}}], \tag{3.24}$$

and

$$\Theta_{\mathrm{C}} = \Theta(P_{\mathrm{Br}_i} = 1), \quad \exists\ i \in [1, N_{\mathrm{tot}}]. \tag{3.25}$$

$\Theta_{P_{max}}$ and Θ_{C} are the surface area heterogeneity coverages at which the adhesion probability P_{Br} is equal to 1, for either all of the N_{tot} particles released, or for at least one of them, respectively.

For a 200-nm diameter particle, the computed spread of the Brownian adhesion probability is

$$\Delta\Theta_{\mathrm{BD,\,2a\,=\,200\,nm}} = 0.15 - 0.11 = 0.04 \tag{3.26}$$

where the subscript BD denotes *Brownian displacements*. The non-zero spread indicates that, for the small particle considered, a range of values of Θ exist for which the adhesion probability $0 < P_{\mathrm{Br}} < 1$. For these Θ values, therefore, Brownian displacements introduce significant spatial variations that are not observed when Brownian motion effects are ignored. These fluctuations in the direction of flow can, indeed, become meaningful enough so as to yield smaller adhesion probabilities P_{Br} for larger values of the surface coverage Θ.

The binding capability of the collector, therefore, appears to be governed not only by the total amount of attractive heterogeneity but also by the magnitude of the spatial variations in the flow direction. Flowing particles can be translated due to Brownian displacements into more attractive or more repulsive areas of the collector, and irrespectively of the total amount of heterogeneity that patterns the collector surface.

The respective spread of the adhesion probabilities for large particles ($2a = 2\,\mu$m) is equal to zero,

$$\Delta\Theta_{\mathrm{BD},\,2a=2\,\mu\mathrm{m}} = 0.21 - 0.21 = 0\,. \tag{3.27}$$

A zero probability spread indicates that the probability of adhesion on a specific heterogeneous collector characterized by a given surface coverage Θ is either 0 or 1, in complete agreement with trajectory computations in which the effects of Brownian motion are not considered. The computed spread in Eq. (3.27) thus suggests that Brownian motion has a negligible effect on the trajectories of large particles translating over collectors patterned with nano-scale heterogeneity.

For a fixed surface coverage of $\Theta = 0.15$, a histogram of the horizontal displacements the particles translate in the direction parallel to the collector before adhering is shown in Fig. 3.23. The trajectories, which include the effects of Brownian displacements, not only predict adhesion at distances $x/a \simeq 398$ but also in the vicinity of $x/a = 1719$, 4478, 5250 and $x/a = 5800$, suggesting the existence of other "hot spots"[37] for particle adhesion in those regions of the collector.

3.3.4 Péclet numbers.

To provide quantitative insight on the relative importance of shear and Brownian effects acting in the direction of flow, a Péclet number is defined as

$$\mathrm{Pe}_{(\mathrm{B/S})} = \frac{D_{\parallel}(H,a)}{\dot{\gamma}a^2}, \tag{3.28}$$

where $D_{\parallel} = f_4\,D_{\infty}$ is the diffusion coefficient in the direction parallel to the collector and depends solely on the particle size and distance H between the particle's center and the collector.[41,74] To avoid the unrealistic case of the particle being in physical contact with the collector, an arbitrarily small distance of $\delta = 0.5$ nm is chosen as the distance at contact, such that $H = a + \delta$.

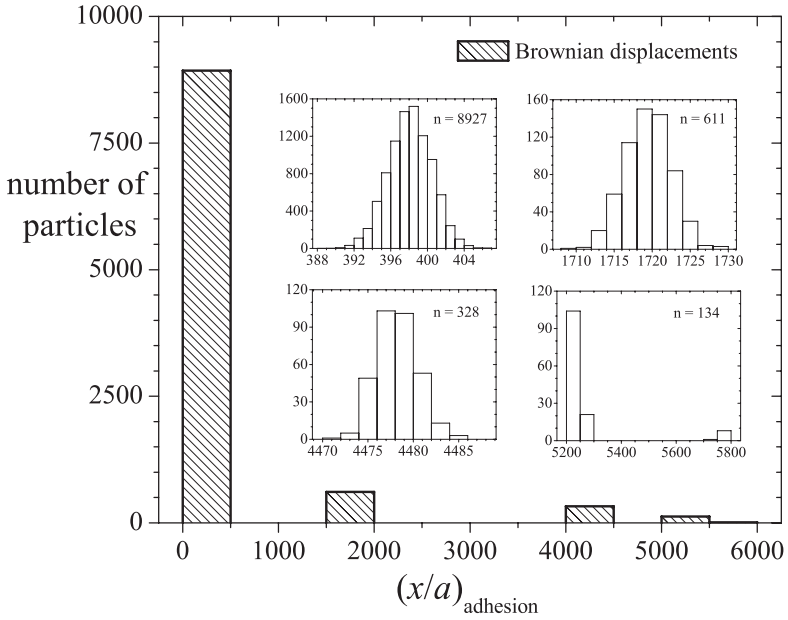

Figure 3.23. Statistical distribution of the locations of adhered particles obtained from simulations of particle trajectories in which Brownian motion is computed as Brownian displacements, for a collector patterned with a heterogeneity coverage of $\Theta = 0.15$. Other simulation parameters are: $2a = 200$ nm, $h_p = 0$ nm, $\kappa^{-1} = 4$ nm, $A_H = 5 \times 10^{-21}$ J, $\psi_{\text{sphere}} = \psi_{\text{collector}} = -25$ mV, $\psi_{\text{patch}} = 50$ mV.

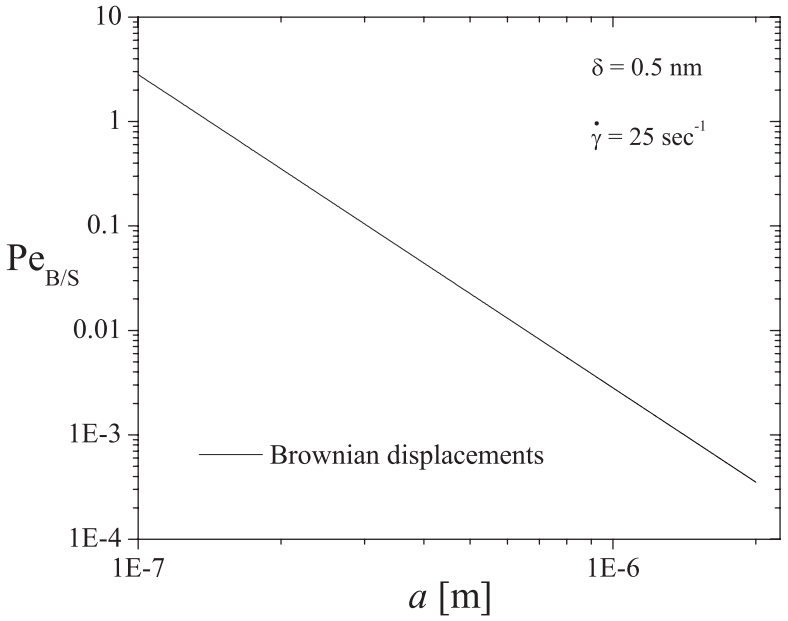

Figure 3.24. $Pe_{B/S}$ numbers as a function of the particle size.

Eq. (3.28) resembles the Péclet number defined by Kemps and Bhattacharjee[74] to describe the transport of colloidal particles in the proximity of surfaces patterned with spherical asperities. In that study, however, the Péclet number indicated a greater relative importance of the shear flow with respect to the particle diffusion, such that the diffusivity considered in the Péclet number definition was that of the bulk, or, the Stokes-Einstein diffusivity, and hydrodynamic effects were incorporated only in the computation of particle trajectories.

In the current work, the effects of Brownian motion on particles interacting with heterogeneous collectors are studied for small separation distances in particular, with relevance to the evaluation of Brownian effects on adhesion thresholds. It thus seems appropriate to consider the hydrodynamic effects that effectively reduce the particle diffusivity as the particle approaches the collector, and define the Péclet number in terms of $D_{\|}$ instead of D_{∞}.

As shown in Fig. 3.24, $\mathrm{Pe}_{(\mathrm{B/S})}$ values decrease exponentially with particle size, suggesting that Brownian motion dominates over shear forces only for small particles. While Brownian effects are prominent with respect to shear forces, or comparable to them, for small particles ($a \leq 200$ nm) in low-shear rate flows, for particle radii as small as $a = 500$ nm and larger, $\mathrm{Pe}_{\mathrm{B/S}}$ numbers fall below 0.05, suggesting that Brownian forces become negligible.

To quantify the relative importance of Brownian motion effects and DLVO interactions a Péclet number $\mathrm{Pe}_{\mathrm{B/C}}$ is defined as

$$\mathrm{Pe}_{\mathrm{B/C}} = \frac{k_{\mathrm{B}}T}{U_{\mathrm{GSI_{UA}}}(D = \kappa^{-1})}\,, \tag{3.29}$$

where $U_{\mathrm{GSI_{UA}}}(D = \kappa^{-1})$ denotes the average particle-flat collector total energy of interaction computed with the $\mathrm{GSI_{UA}}$ technique[14] at a fixed separation distance $D = \kappa^{-1}$.

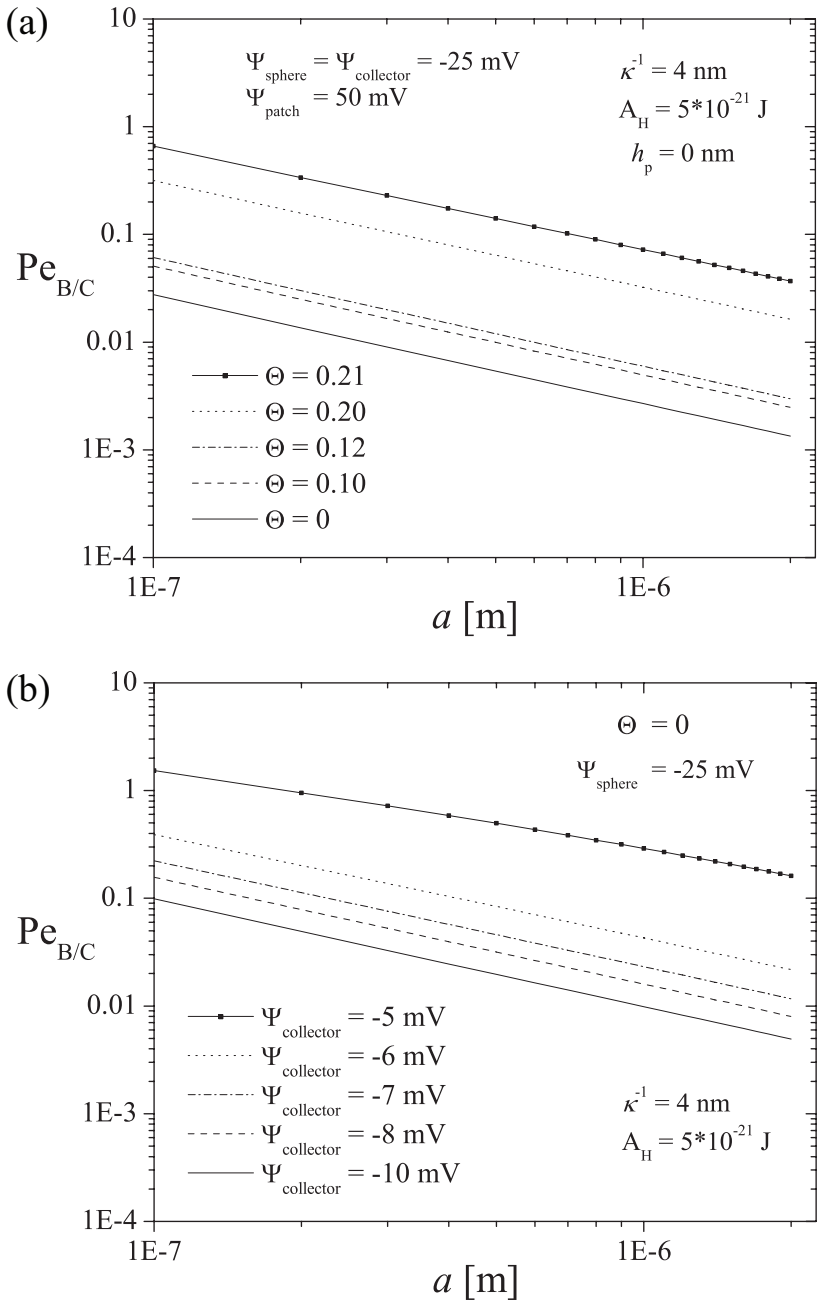

Figure 3.25. $\mathrm{Pe_{B/C}}$ numbers as a function of the particle size, for heterogeneous and homogeneous collectors. (a) $\mathrm{Pe_{B/C}}$ numbers for a range of surface loadings Θ, in the case of heterogeneous collectors. (b) $\mathrm{Pe_{B/C}}$ numbers computed for various collector surface potentials $\psi_{\mathrm{collector}}$, for uniformly charged, flat collectors.

Péclet numbers obtained from Eq. (3.29) are presented as a function of the particle size in Fig. 3.25, for a few values of the surface coverage Θ.

For particle sizes that are relevant for experimental purposes and a range of surface loadings for which the collector is net repulsive, particle-collector dynamics are dominated by DLVO interactions, rather than Brownian motion effects, as suggested by the numbers $\mathrm{Pe}_{\mathrm{B/C}} < 1$ shown in Fig. 3.25(a). The random distribution of patches on the collector surface creates both locally attractive and locally repulsive areas, such as those showed in Fig. 3.22(b) for a flat collector with a surface area heterogeneity coverage of $\Theta = 0.12$ sampled by a $2a = 400$ nm diameter particle. Brownian motion cannot overcome the high energy barriers that characterize the locally repulsive areas, such that particle deposition on patchy collectors is not due to Brownian motion, but instead, controlled by spatially-varying DLVO interactions.

Particle deposition on slightly net-repulsive homogeneous collectors, however, can be attributed to Brownian motion effects since these systems present energy barriers that are lower than those in the locally repulsive areas within the heterogeneous collectors. $\mathrm{Pe}_{\mathrm{B/C}}$ numbers for the case of interactions with electrostatically and topographically uniform collectors, obtained from Eq. (3.29) for a range of particle sizes and varying collector potentials are shown in Fig. 3.25(b). For small particles ($a \leq 250$ nm) and slightly repulsive uniform collectors ($\Psi_{\mathrm{collector}} = -5$ mV), $\mathrm{Pe}_{\mathrm{B/C}} > 1$ suggest that Brownian motion effects are indeed more significant than, or comparable to, DLVO interactions, and can therefore be responsible for increased deposition rates.

3.3.5 Conclusion.

The influence of Brownian motion on the dynamics of large and small colloidal particles flowing over patchy and pillared collectors was studied by modeling particle

trajectories that included the effects of Brownian displacements, in addition to those of shear and colloidal forces.

Brownian motion is expected to be meaningful only for particle-collector systems characterized by a relatively low energy barrier in the energy-distance profile. For large particles, interactions with both patchy and pillared collectors are found to be governed by high energy barriers, which prevent particle deposition. Small particles, however, are strongly attracted to pillared collectors, such that particle adhesion is controlled by DLVO interactions and not by Brownian motion. Brownian motion effects, therefore, could be significant only in the case of small particles flowing over patchy collectors because these systems present intermediate, or relatively-low energy barriers.

In the case of interactions between a small particle and a patchy collector, the addition of Brownian displacements introduces significant spatial variations in particle trajectories. These spatial variations of the adhesion sites translate into a non-zero spread of the adhesion probability, in contrast to the zero-probability spread obtained when Brownian motion effects are neglected.

A Péclet number that quantifies the relative importance of shear and Brownian effects decreases exponentially with particle size. For the low shear rate flow considered, Brownian effects are seen to become more significant than, or comparable to, the shear motion only for particle radii of up to $a \simeq 200$ nm. For larger particles, Brownian motion effects are negligible, as evidenced by Péclet numbers that fall below unity.

To quantify the relative importance of Brownian and colloidal (DLVO) effects, $\mathrm{Pe}_{\mathrm{B/C}}$ numbers were defined as the ratio of the thermal energy to the average particle-collector DLVO energy of interaction at a fixed separation distance $D = \kappa^{-1}$. $\mathrm{Pe}_{\mathrm{B/C}}$ numbers computed for varying particle sizes and for surface loadings Θ for which average interactions are repulsive, decrease exponentially with particle size and are

smaller than 1 for all the parameter ranges considered. Therefore, in the case of particles flowing over collectors patterned with nano-scale heterogeneity, Brownian motion effects are shown to be negligible also with respect to DLVO interactions.

The results presented in this section thus reveal that Brownian motion has a negligible influence on particle trajectories over collectors patterned with nano-scale heterogeneity, the non-uniform distribution of which creates locally attractive and repulsive areas within the collector. High energy barriers in strong locally repulsive areas cannot be overcome by Brownian motion ($\mathrm{Pe}_{\mathrm{B/C}} \ll 1$), such that particle deposition on patchy collectors is controlled by spatially varying DLVO interactions and not by Brownian motion. Even though Brownian effects become more significant than, or comparable to, shear forces for small particles in low shear rate flows, the overall adhesive behavior of the system, which is characterized by the adhesion threshold, remains unaffected by the introduction of Brownian motion effects in the simulations. For particle sizes that are usually used in experimental studies ($a = 0.5, 1\,\mu\mathrm{m}$), it is thus reasonable to neglect Brownian motion effects in studies of particle trajectories over collectors covered with nano-scale heterogeneity.

CHAPTER 4

INTERACTIONS BETWEEN NANOSCALE-HETEROGENEOUS PARTICLES AND CHEMICALLY UNIFORM FLAT COLLECTORS

4.1 Introduction.

Interest in the study of interactions of anisotropic particles has grown significantly, leading to the recent development of innovative particle synthesis techniques used to engineer nano- and colloidal particles with multiple surface features. "Patchy particles", as defined by Zhang and Glotzer,[127] are particles that exhibit strong directional interactions induced by the presence of a finite number of distinct patches on the particle's surface. Highly anisotropic interactions between patchy particles and/or surfaces patterned with effectively "attractive" and "repulsive" interaction sites can lead to the assembly of otherwise neutral or repulsive surfaces into ordered arrays. Surface-anisotropy in shape, size, patchiness, and chemical functionality can, in fact, be precisely tailored towards the design of specific target structures.[48]

Anisotropic particles at the nano and colloidal scales of diverse shapes, sizes and electronic and optical properties were synthesized with chemical, physical and biologically-inspired ingenious techniques.[48,95] Selective crystallization and deposition facilitated the fabrication of gold and silver 3D nano-structures, such as nanorods,[68] cubes and boxes.[109] Reductive synthesis of colloidal particles in solution is another chemical synthesis technique used to yield anisotropic nano-particles of controlled shape, such as platinum, gold, and copper structures of diverse morphologies, including tetrahedral, cubic, icosahedral, and also flat triangular and hexagonal.[10,53,86] Colloidal particles of controlled configuration are also obtained using

automated stepper lithography, and the resulting "LithoParticles",[58] produced in letter shapes, are released into a liquid solution to yield "a colloidal alphabet soup". Particles with dipolar charge distribution, particle-doublets, and "raspberry-like" microparticles were synthesized by microcontact printing of a monolayer of small (negatively charged) colloid particles onto a monolayer of larger (positively charged) particles.[25]

Current patchy particle synthesis techniques pose, however, either scalability difficulties, or, are limited in terms of achieving controlled numbers and chemical functionalization of patches that pattern particle surfaces.[95] New techniques that aim to overcome such challenges are constantly emerging. The newly-developed Particle Replication In Nonwetting Templates (PRINT ®)[99,125] method, for example, makes use of a non-wetting substrate to yield isolated nano-particles, eliminating the need to separate the desired particles from the template or mask.

Patchy particles can be used as building blocks of target structures that can be assembled in photonic crystals, sensors, and electronic, molecular imaging and drug-delivery devices.[11,28,95,123] Anisotropy-based particles can also be incorporated within self-healing materials, switching displays, which resemble nature-abundant camouflage techniques, and other "smart" materials, *i.e.*, materials capable of reacting to external stimuli.[123] Janus particles, whose surface is divided into two clearly-defined areas of equal size, and patchy particles, have also been recently used as autonomous swimmers, and such self-propelling microscale objects could potentially be developed into drug delivery, fluid mixing, and on-chip particle transport applications.[95] The exact propulsion mechanism of the micro-swimmers, however, is not yet fully understood and constitutes a subject of current research.

From the theoretical perspective, patchy particles were first classified by Glotzer and Solomon,[48] who developed a unifying framework to describe the classes of patchy particles already synthesized. Each anisotropy type of a colloidal building block is

assigned a 'dimension', such that the anisotropic characteristic increases when moving along a specific dimension. Some of such dimensions are anistropy attributes such as surface coverage or patchiness (A), aspect ratio (B), branching(E), and roughness (H). Anisotropic particles are then described by a dimensionality number that indicates the number of orthogonal dimensions that are necessary to characterize the particle. The particle complexity thus increases with increasing dimensionality number.

In many recent computational studies, patchy particles are modeled as units composed of distinct "atoms". Specific attributes are assigned to each atom, depending on whether it belongs to the 'patch' or 'core' surface areas of the particle. Zhang and Glotzer[127] performed Brownian dynamic simulations to model the self assembly of particles patterned with patches positioned at specific locations. The 'atoms' pair potentials were modeled with Lennard-Jones potentials to describe weak, long-range attractive interactions, and excluded-volume interactions are included through a soft sphere approach. A number of precise and ordered structures, such as chains, sheets, rings, icosahedra and other polyhedra, were obtained for varying configurations of the particle patches. The self assembly of ordered periodic structures is also predicted by Brownian dynamics simulations of tethered nanoparticles,[65] and star-branched and spherical polyelectrolytes are shown by molecular dynamic computations to assemble into charged, patchy colloids.[84] Other theoretical approaches model patchy particle interactions by including pair potential functions to investigate, for example, reversible gel formation,[101] and the interplay between self-assembly and condensation of patchy particles decorated with a few weakly attractive spots.[112] Anisotropic interactions between particles are also incorporated in models of globular proteins,[45,105] and in lattice density functional studies that characterize T-shaped equilibrium assemblies of patchy particles.[94]

While theoretical work on patchy particle interactions at the molecular scale abund, only a handful of studies describe colloidal interactions of heterogeneous par-

ticles in close contact to a wall and the effects of such heterogeneities on particle deposition. Sphere-plate and sphere-sphere DLVO interactions for spheres patterned with topographical heterogeneity were computed numerically[18,108] and analytically,[110] and model predictions were found to agree with experimental measurements.[111] Spherical chemical heterogeneity, however, was not included. A recent study by Chatterjee et. al.[29] is focused on the deposition of micro-scale particles onto larger Janus and patchy spherical collectors. Chemical heterogeneity is modeled by patterning the spherical collector with adhesion-favorable and adhesion-unfavorable surface properties, which are assigned to either each half of the sphere (Janus collectors) or to alternating stripes that cover the spherical surface (patchy collectors). The stripes width is larger than the depositing particle diameter. Deposition of colloidal particles onto the spherical heterogeneous collectors is analyzed as a function of system parameters, such as collector orientation, amount of collector heterogeneity and colloidal particle velocity.

By contrast, microscale particles flowing over heterogeneous collectors bearing nanoscale patches have been studied extensively, both experimentally[71,72,81,103] and computationally,[14,38,39,126] as described in previous sections.

Results presented in this section describe the effect of nanoscale spherical heterogeneity on particle-collector interactions, emphasizing the role of patchy particles as the depositing agents, in contrast to previous studies[29] in which the patchy particles modeled heterogeneous collectors much larger than the depositing colloidal particles. A sphere-partition algorithm that yields the discretization of spherical surfaces into equal-area elements is introduced in Sec. 4.2. Colloidal DLVO interactions, computed as the sum of attractive van der Waals (vdW) and repulsive electrostatic double layer (EDL) interactions, are computed first for the homogeneous particle-collector system in Sec. 4.3 to validate the algorithm used for the discretization of the sphere. In Sec. 4.4, particle trajectories of patchy particles patterned with ordered heterogeneity flowing over uniform flat collectors are presented for various heterogeneity

orientations. Dynamics of particle-collector systems involving patchy particles covered with randomly-distributed, nanoscale heterogeneity are analyzed in Sec. 4.5. Statistical measures such as the collection probability, number of local extrema in the particle trajectories, and effective residence time of a patch within the electrostatic zone of influence (ZOI) are introduced. Detailed comparisons are made with the corresponding patchy collector configuration that has been extensively studied in both experimental[81,103] and computational previous work.[38,39] Adhesion regime diagrams for each system are presented to quantify the average surface loading of patches at which particles begin to adhere. The main findings and conclusions are summarized in Sec. 4.6.

4.2 Sphere discretization.

In order to simulate collector interactions with heterogeneous spherical particles using the GSI technique,[38] the spherical surfaces must be discretized into differential areal elements, each of which can be assigned distinct properties. In the results presented in this section, spherical surfaces are discretized into regions of equal area using Leopardi's[82] recursive zonal EQual area Sphere Partitioning (EQSP) algorithm, which yields the discretization of higher dimensional spheres into regions of equal area and small diameter. A schematic diagram of a sphere discretized into $N_{\mathrm{p}} = 500$ regions (elements) is presented in Fig. 4.1(a).

The accuracy of the EQSP algorithm is firstly verified by discretizing a $2a = 1\,\mu m$ diameter sphere into $N_{\mathrm{p}} = 25963$ elements, such that the individual element area is $\mathrm{d}A_i \simeq 121$ nm^2. For each sphere surface element, the absolute value of its projected area on an horizontal plane is computed from

$$dS_i = |\mathbf{n} \cdot \mathbf{e}_{\perp}|\, dA_i\,, \tag{4.1}$$

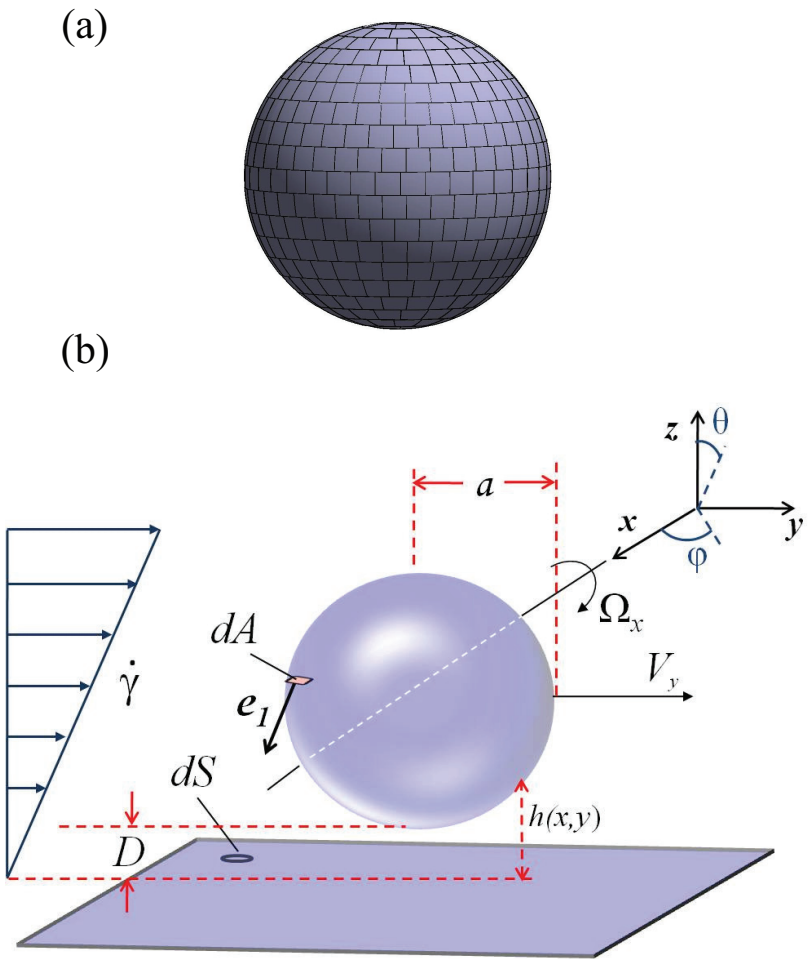

Figure 4.1. (a) Illustration of a sphere discretized into $N_\mathrm{p} = 500$ equal area regions. (b) Schematic diagram of a uniform particle of radius a interacting with a uniform flat collector. The local and minimum particle-collector separation distances are denoted by h and D, respectively. Differential surface elements dA on the particle and dS on the collector are also indicated, as well as the unit vector $\mathbf{e_1}$ that points in the direction of the collector surface element. The rotational and translational velocities are Ω_x and V_y, respectively, and the flow shear rate is $\dot{\gamma}$.

where dA_i is the area of the sphere element i, dS_i is its projected area on the plane, $\mathbf{n}$ is the vector normal to the sphere element and $\mathbf{e}_\perp$ denotes the direction normal to the projection plane. The sum of the elemental projected areas $\sum dS_i$ is within 0.0038% of the exact value of $2S = 2\pi\, a^2$ (for two hemispheres).

4.3 Homogeneous particle-collector systems.

In the GSI technique, the total force or energy of interaction is obtained from a pairwise summation of interactions between differential areal elements on the collector and particle surfaces. In previous work,[14,37–39] the collector surfaces were electrostatically and topographically heterogeneous, while the flowing colloidal particles were smooth, uniformly charged spheres. A discretization scheme of the spherical surface was therefore not needed, and only the heterogeneous collector was partitioned into small areal elements. The accurate modeling of systems of heterogeneous particles, however, does require the discretization of the spherical surfaces. In the results that follow, the use of the GSI technique is extended to the modeling of systems that include heterogeneous colloidal particles by incorporating the EQSP sphere discretization scheme in the computation of DLVO particle-collector interactions.

The case of particles with ordered heterogeneity is considered first. DLVO interactions for the homogeneous system are obtained by implementing the GSI technique, and including the discretization of only *one* interacting surface, which is either the spherical surface or the flat collector. For the case of a discretized, homogeneous spherical particle, all the EQSP-generated differential elements are assigned the same surface properties, which also equal those of the uniformly patterned collector.

Presented in Fig. 4.1(b) is a schematic diagram of an homogeneous particle-collector system. Negatively charged, flowing particles of radius a interact with the flat uniform collector, which is also negatively charged. The local and minimum particle-collector separation distances are denoted by h and D, respectively. Due to

the linear shear flow with shear rate $\dot{\gamma}$, the particle translates in the y-direction with a linear velocity V_y and rotates around an axis parallel to the collector surface with a rotational velocity Ω_x. The origin of the Cartesian coordinate system is the left edge of the collector. For interactions of $2a = 1\mu$m diameter particles, the collector length is $L = 30\,\mu$m, while shorter collectors of length $L = 20\,\mu$m were simulated for interactions of $2a = 500$ nm diameter particles. A spherical coordinate system with origin in the sphere's center, is also defined. The inclination angle is θ, $0 \leq \theta \leq \pi$, and the azimuth angle is ϕ, $0 \leq \phi \leq 2\pi$. The radial direction is normal to the particle surface.

In Fig. 4.2(a), the energy profile of a smooth and uniformly charged $2a = 1\,\mu m$ diameter particle interacting with a flat surface is shown. Colloidal interactions are characterized by the inverse Debye screening length $\kappa^{-1} = 4$ nm and Hamaker constant $A_{\rm H} = 5{\times}10^{-21}$ J. The surface loading Θ, defined as the area of the collector (or particle) patterned with heterogeneity relative to the total collector (or particle) area, is equal to zero for both interacting surfaces, which carry an electrostatic potential $\psi = -25$ mV. The energy profile is thus defined by the repulsive electrostatic double layer (EDL) interactions between the uniformly and equally charged particle and collector surfaces.

The interactions presented in Fig. 4.2(a) are computed by implementing the GSI technique and either including (solid line) or not (dotted line) the EQSP algorithm for the modeling of the uniformly charged, smooth sphere. As in Sec. 4.2, the uniform $2a = 1\,\mu$m diameter particle is discretized into $N_{\rm p} = 25963$ elements, such that the area of each element is $\mathrm{d}A_i \simeq 121$ nm^2. In the case for which the spherical surface is not discretized into differential elements, the collector surface is partitioned instead. The collector grid consists of 91 square elements that represent a length of $2a = 1\,\mu$m, such that the length of each square element is ≈ 11 nm. The spherical and planar discretization schemes are specifically chosen so as to define equal-area

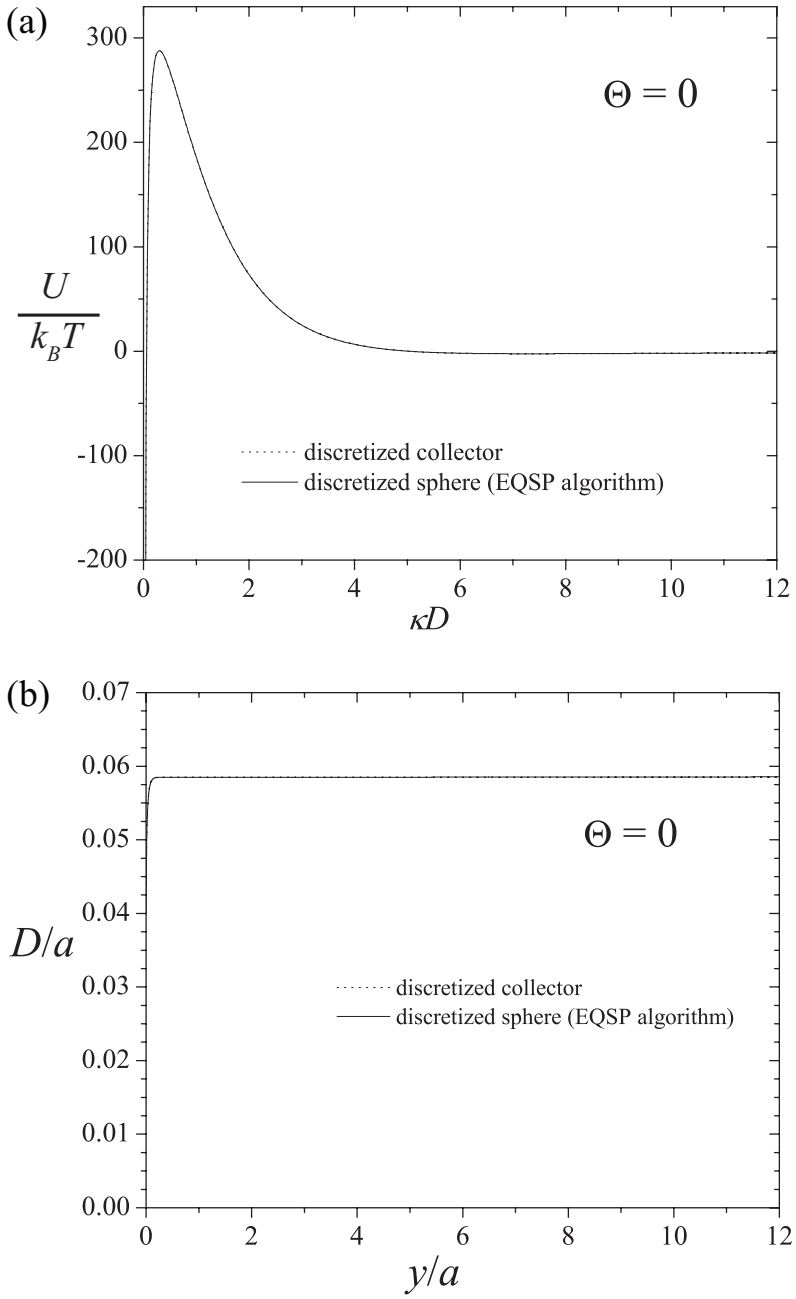

Figure 4.2. Energy-distance profile (a) and particle trajectory (b) for a uniform particle interacting with a uniform collector. The particle's surface is either discretized into equally patterned area elements (with the EQSP algorithm) or treated as a non-discretized uniform surface, in which case the collector surface is discretized instead. In both cases, DLVO interactions are computed with the GSI technique. The simulation parameters are: $2a = 1$ μm, $\dot{\gamma} = 25$ sec^{-1}, $\kappa^{-1} = 4$ nm, $A_{\mathrm{H}} = 5{\times}10^{-21}$ J, $\psi_{\mathrm{collector}} = \psi_{\mathrm{sphere}} =$ -25 mV.

elements, in this case of $dA_i \simeq 121$ nm^2. In heterogeneous systems, the size of one areal element usually equals the surface feature size, and therefore, discretization schemes vary with particle and surface features dimensions. It is seen in Fig. 4.2(a) that both computational techniques yield results that are in perfect agreement. Particle trajectories for the homogeneous system were also calculated with the mobility matrix approach described in Sec. 2.8 and implementing both computational methods, with results shown in Fig. 4.2(b). A comparison with trajectories obtained for uniform non-discretized spheres and sets of different parameters also showed a complete agreement between the GSI and the *GSI-EQSP* techniques, which validates the discretization scheme.

4.4 Interactions with heterogeneous particles: Ordered heterogeneity.

Particle heterogeneity is modeled by partitioning the spherical surface into differential areal elements, each of which can be assigned distinct surface properties. Ordered particle heterogeneity assigned in the form of stripes with a subtended angle of $\pi/6$ radians, located at different polar (or zenith) angles θ from the positive z-axis are shown schematically in Fig. 4.3. The origin of the spherical coordinate system is the center of the particle, as shown in Fig. 4.1(b).

Trajectories of striped particles translating in shear flow over uniformly charged, flat collectors are presented in Fig. 4.4. The spherical surfaces are topographically smooth and electrostatically heterogeneous. In Fig. 4.4(a), the sphere stripes are charged with a surface potential of $\psi_{\text{stripe}} = 50$ mV, while the remaining sphere surface and the flat collector bear an equal potential of $\psi_{\text{sphere}} = \psi_{\text{collector}} = -25$ mV. The attractive stripe-surface interactions dominate the particle's behavior and thus all the striped particles ultimately adhere on the collector surface. Each striped particle adheres at a different horizontal displacement from the origin of the collector,

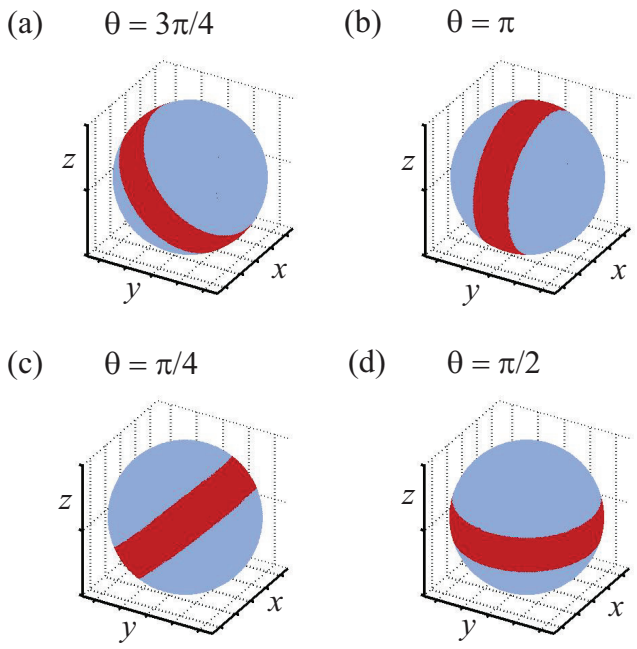

Figure 4.3. Schematic diagram of $2a = 1\mu$m diameter spheres patterned with stripes located at varying polar angles θ. (a) $\theta = 3\pi/4$. (b) $\theta = \pi$. (c) $\theta = \pi/4$. (d) $\theta = \pi/2$.

however, due to the initial angular orientation of the stripe. The distance the particle translates before adhering on the collector increases as $|(\pi/2 - \theta)|$ increases. For the case of $\theta = \pi/4$, however, the traveled distance before adhesion is larger than that for $\theta = 3\pi/4$ due to the clockwise rotation of the particle in the shear flow. For the same sphere-collector system properties, non-adhesive particle behavior is observed with a slightly repulsive stripe electrostatic potential. Particle trajectories computed for a sphere stripe potential of $\psi_{\text{stripe}} = -10$ mV are presented in Fig. 4.4(b). The particles do not adhere on the collector and instead translate in cyclic trajectories that are off-phase, as a result of the different initial angular orientations of the stripes. Colloidal interactions are defined by the Debye length $\kappa^{-1} = 4$ nm and the Hamaker constant $A_{\text{H}} = 5{\times}10^{-21}$ J, chosen to resemble experiments performed for silica-water-silica systems.

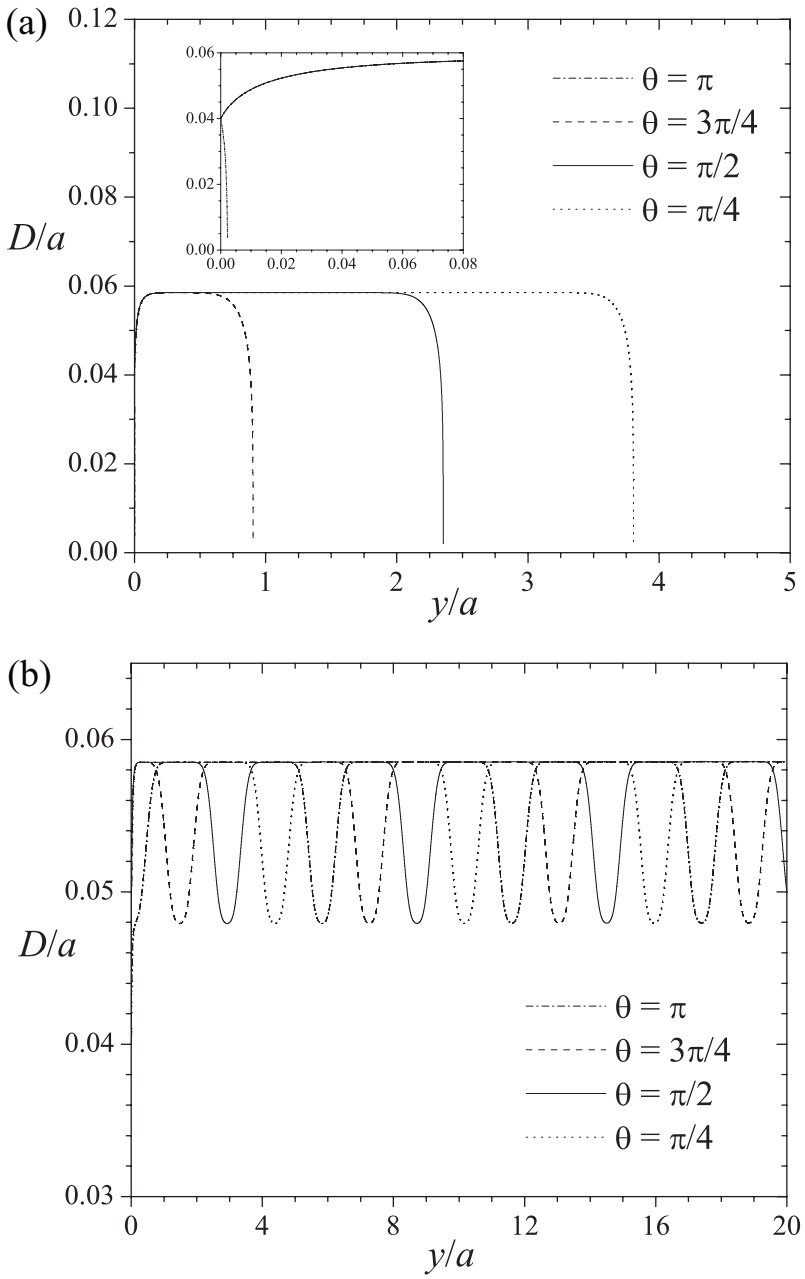

Figure 4.4. Trajectories of $2a = 1\,\mu$m diameter spheres patterned with stripes located at different initial polar locations interacting with uniformly charged, flat collectors. The unpatterned regions of the sphere and the uniform collector are charged with a uniform electrostatic potential of ψ_{uni} = -25 mV. The potential assigned to the sphere stripes varies, to yield attractive or repulsive interactions. (a) Attractive stripe-collector interactions, obtained with a stripe potential $\psi_{\text{stripe}} = 50$ mV. (b) Repulsive stripe-collector interactions, obtained with a stripe potential $\psi_{\text{stripe}} = -10$ mV.

A myriad of particle dynamic behaviors can thus be readily simulated with the EQSP-GSI technique by varying not only the number, angular initial orientation, and width of the stripes, but also the particle and collector surface properties. Parameters that define colloidal interactions, such as the inverse Debye screening length κ^{-1} and the Hamaker constant A_{H}, can also be specifically tailored for each pair of sphere-collector surface elements.

4.5 Interactions with heterogeneous particles: Random heterogeneity.

Particles with randomly distributed heterogeneity can also be constructed by randomly selecting the sphere elements that are assigned the distinct surface properties. In this section, interactions between patchy particles and uniformly charged, flat collectors are studied for different particle sizes and a range of surface loadings and Debye lengths. Detailed comparisons to interactions computed for systems of uniformly charged spheres with patchy collectors are made to quantify differences in the systems' adhesive properties. The patchy particle and patchy collector systems are schematically depicted in Fig.4.5. Patches on either heterogeneous surface are assigned a potential of $\psi_{\mathrm{het}} = 50$ mV, while the other regions of the heterogeneous surface and the homogeneous surface bear a uniform electrostatic potential of $\psi_{\mathrm{uni}} = -25$ mV. The interactions between a patch and the homogeneous surface are therefore attractive, while the interactions between other regions are repulsive. The individual patch area equals that of the surface element ($\mathrm{A}_{\mathrm{patch}} \simeq 121$ nm^2), such that the patches approximately model 11 nm squares. Due to the pseudo-random, Poisson distribution used to locate patches on both heterogeneous surfaces (planar or spherical), there are no regions on either heterogeneous surface where patches are preferably assigned.

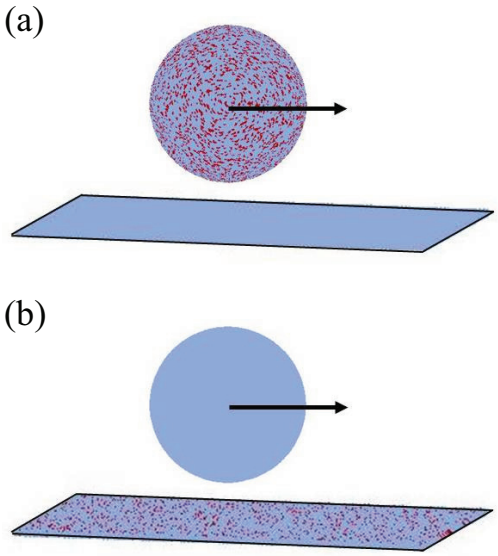

Figure 4.5. Schematic diagrams of particle-collector systems with one heterogeneous surface. (a) Patchy sphere-homogeneous collector. (b) Homogeneous sphere-patchy collector.

For a fixed surface loading of $\Theta = 0.17$, trajectories of patchy particles flowing over uniformly charged collectors and those of uniformly charged particles flowing over patchy collectors are presented in Figs. 4.6(a)-(b) for two particle sizes and Debye lengths. For each case, the ratio of the particle's rotational to translational velocities are plotted as a function of the horizontal displacement in Figs. 4.6(c)-(d).

In Fig. 4.6(a), the upper lines represent trajectories of $2a = 1\mu$m diameter patchy and uniform spheres translating in shear flow above uniform and patchy collectors respectively, for a Debye length of $\kappa^{-1} = 5$ nm. Due to the large Debye length, both particles translate at a relatively large separation distance from the collector, and the particles do not contact or deposit on the collector. The average separation distance for the patchy particle is $D/a = 6.639 \times 10^{-2} \pm 2.075 \times 10^{-3}$ ($D = (33.2 \pm 1.04)$ nm), while that of the uniform particle is $D/a = 6.599 \times 10^{-2} \pm 2.130 \times 10^{-3}$ ($D = (33.0 \pm 1.07)$ nm), in agreement with the secondary minimum in the energy

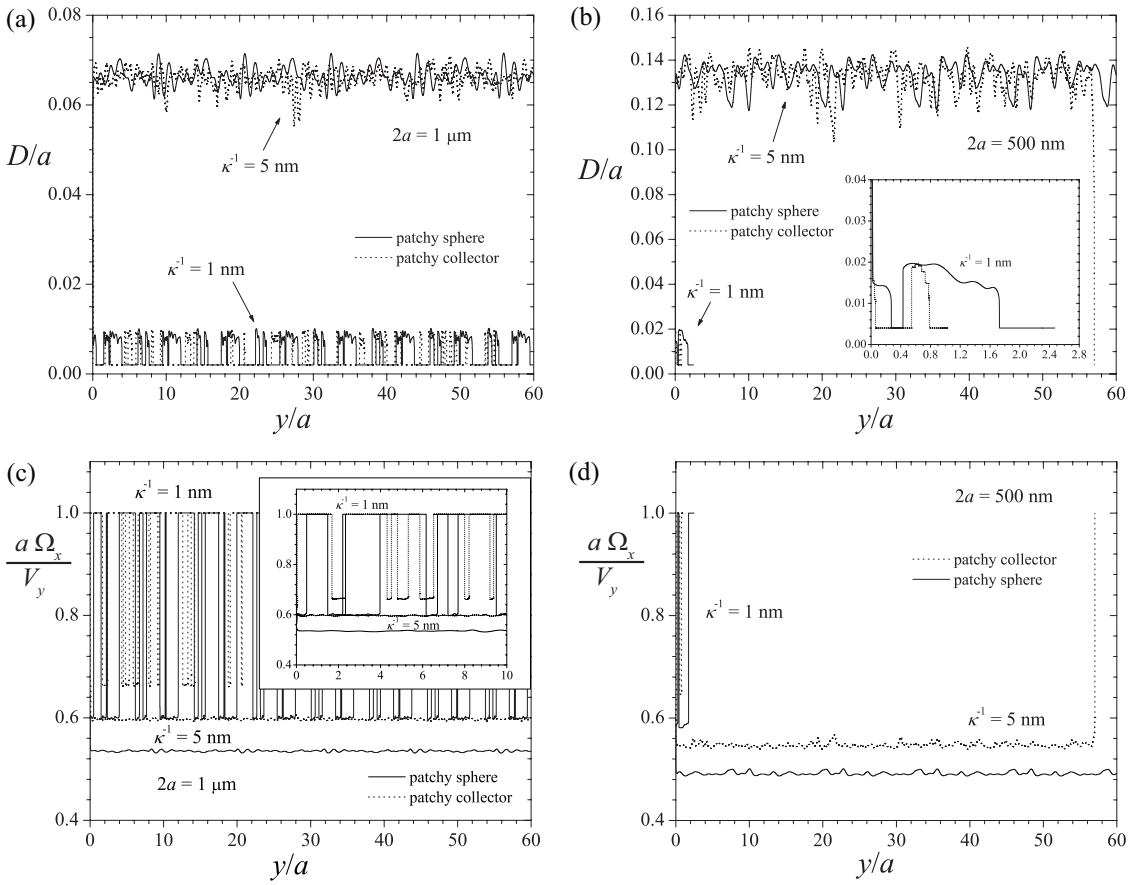

Figure 4.6. Trajectories and velocity ratios for patchy and uniform particles of two different sizes interacting at Debye lengths $\kappa^{-1} = 1, 5$ nm, for a fixed surface loading $\Theta = 0.17$. Rolling friction is computed with a friction coefficient of $\mu_{\mathrm{R}} = 1.3 \times 10^{-4}$.(a)(b) Particle trajectories of patchy and uniform particles, for particle sizes of $2a = 1\mu$m (a) and $2a = 500$ nm (b). (c)(d) Angular to translational velocity ratios of patchy and uniform particles, for particle sizes of $2a = 1\mu$m (c) and $2a = 500$ nm (d). For clarity, all solid lines represent the patchy particle system, while all dotted lines indicate results obtained for the patchy collector system.

profile $D_{\min} = 33.1$ nm, computed with the $\mathrm{GSI_{UA}}$ technique.[14] Although the mean separation distance and its standard deviation are practically the same for the patchy particle and patchy collector, adhesion probabilities are found to be larger in patchy particle systems than in patchy collector systems. This behavior is examined in more detail in Sec. 4.5.1 and linked to patchy residence times in Sec. 4.5.3. In Fig. 4.6(c), the ratio of the rotational and translational velocities for a Debye length $\kappa^{-1} = 5$ nm are shown by the lower solid and dotted lines, which indicate results for the patchy and uniform spheres, respectively. In both cases, the ratios fluctuate around the same values, that are less than unity when the particle is not in contact with the collector, confirming that the particles translate faster than they rotate.

The lower solid and dotted lines in Fig. 4.6(a) show trajectories of $2a = 1\mu$m diameter patchy and uniform particles, respectively, for a Debye length $\kappa^{-1} = 1$ nm. It is seen that both particles frequently contact the collector surface (at an arbitrarily small distance $\delta = 1$ nm taken as representative of surface roughness) to yield a trajectory that is characterized by alternating periods of rolling motion and of free flow in close proximity to the collector. Both particles maintain a separation distance $D < 5$ nm as they flow above the entire simulated collector. Velocity ratios as a function of the horizontal displacement are shown by the upper solid and dotted lines (for patchy and uniform particles respectively) in Fig. 4.6(c). The rolling periods for both particles are identified by velocity ratios that are equal to unity, as it is assumed that the particle does not slip when it contacts the surface, while the translation between those periods corresponds to velocity ratios that fall below unity.

Trajectories of $2a = 500$ nm diameter particles at Debye lengths $\kappa^{-1} = 1, 5$ nm are shown in Fig. 4.6(b). The patchy spheres are discretized into $N_{\mathrm{p}} = 6489$ elements, such that the surface area of each element remains $\mathrm{d}A_i \simeq 121$ nm^2, and the patchy collectors are modeled with a grid consisting of 45 square elements that represent a length of $2a = 500$ nm, such that the length of each square element is ≈ 11 nm. At a

large Debye length of $\kappa^{-1} = 5$ nm, the patchy particle (upper solid line) translates at a separation distance of (33.40 ± 1.45) nm, while the average separation distance of the uniform particle (upper dotted line) is (33.20 ± 1.68) nm, in good agreement with the secondary minimum in the energy profile of $D_{min} = 33.5$ nm, computed with the GSI_{UA} technique.[14] The amount of spatial fluctuations of the uniform particle trajectory is larger, as expected from the larger separation distance standard deviation. More importantly, the uniform particle adheres on the patchy collector, while the patchy particle flows above the entire uniform collector, without adhering. The respective velocity ratios, presented in the lower solid and dotted lines in Fig. 4.6(d) are smaller than 1. Both particles translate fast, with respect to their rotational motion, and, for the uniform particle, the ratio increases to 1 when the particle is arrested on the collector due to a rolling resistance in the direction of flow that retards the particle's motion as a consequence of elastic deformations of the surfaces in contact.

The condition for particle arrest is found from a force balance in the direction of flow and reads[39]

$$F_y + \frac{T_x}{a} - F_{rf} < 0 \tag{4.2}$$

where F_y and T_x are the shear-induced force and torque, respectively, and $F_{rf} = \mu_R F_z^N$ is the rolling resistance, determined by a friction coefficient μ_R and the normal force $F_z^N = -F_{DLVO}$. The particle therefore arrests on the collector once the DLVO forces, multiplied by an appropriate friction coefficient, are sufficiently attractive to overcome the shear-induced effects, or, when

$$F_y + \frac{T_x}{a} + \mu_R F_{DLVO} < 0\,. \tag{4.3}$$

The rolling friction is computed with a friction coefficient of $\mu_R = 1.3 \times 10^{-4}$.

For a Debye length of $\kappa^{-1} = 1$ nm, trajectories of patchy and uniform $2a = 500$ nm diameter particles are shown by the lower solid and dotted lines in Fig. 4.6(b), and

enlarged for clarity in the inset of the same figure. Both particle trajectories exhibit rolling periods that alternate with free flow segments in which the particles translate in close proximity to the collector. Due to friction forces, both particles ultimately adhere on the collector when the DLVO attraction becomes sufficiently large. The velocity profiles, denoted by the upper solid and dotted lines in Fig. 4.6(d), reach a value of unity, thus indicating rolling periods, but fluctuate around values lower than unity in the trajectory segments in which the particles loose contact with the collector.

A more quantitative analysis of the respective rotational and translational motions of the patchy and uniform spheres whose trajectories are presented in Fig. 4.6 is obtained by comparing the average rotational and translational velocities. In each case, the segment of the trajectory over which the average velocities were computed lies between the first local extremum (after the initial location) and the last one (not including the final position of the sphere). To obtain more accurate average values, the mean velocities are not calculated as averages given by

$$\overline{V}\,(\overline{\Omega}) = \frac{1}{N}\sum_{i=1}^{i=N} V_i(\Omega_i)\;, \tag{4.4}$$

but instead, they are computed using the trapezoidal rule, such that

$$\overline{V} = \frac{1}{y_N - y_1}\sum_{i=1}^{i=N-1}\frac{1}{2}(V_i + V_{i+1})(y_{i+1} - y_i) \tag{4.5}$$

and

$$\overline{\Omega} = \frac{1}{y_N - y_1}\sum_{i=1}^{i=N-1}\frac{1}{2}(\Omega_i + \Omega_{i+1})(y_{i+1} - y_i)\,, \tag{4.6}$$

where y_1, y_N are the horizontal locations corresponding to the first and last local extremum points, respectively. The average translational ($\overline{V}$) and rotational ($\overline{\Omega}$) velocities computed with Eqs. (4.5)-(4.6) are presented in Table 4.1. The subscripts "p" and "u" denote patchy and uniform spheres, respectively.

	$2a = 500$ nm		$2a = 1\mu$m	
Debye length [nm]	$\overline{\Omega_{\mathrm{x,\,p}}}/\overline{\Omega_{\mathrm{x,\,u}}}$	$\overline{V_{\mathrm{y,\,p}}}/\overline{V_{\mathrm{y,\,u}}}$	$\overline{\Omega_{\mathrm{x,\,p}}}/\overline{\Omega_{\mathrm{x,\,u}}}$	$\overline{V_{\mathrm{y,\,p}}}/\overline{V_{\mathrm{y,\,u}}}$
1	1.2490	1.5716	1.0328	1.1729
5	1.0007	1.0016	1.0007	1.0013

Table 4.1. Ratios of rotational and translational velocities of 'patchy' (p) and 'uniform' (u) particles, for two particle sizes ($2a = 500$ nm, $2a = 1\mu$m) and two Debye lengths $\kappa^{-1} = 1, 5$ nm. Velocity averages are computed for the trajectories presented in Fig. 4.6.

At a large Debye length, both large and small, patchy and uniform particles rotate and translate at the same velocities, as denoted by the ratios that are equal to unity in the lower row in Table 4.1.

At a small Debye length, however, differences between patchy and uniform particles become noticeable. Though the large patchy particle rotates at roughly the same velocity as the uniform particle, its translation is approximately 17% faster than that of the uniform particle. For smaller particles, however, differences are more significant, as denoted by the rotational velocity ratio of ≈ 1.25 and the translational velocity ratio of ≈ 1.57.

Differences between particle sizes are thus significant only for interactions at small Debye lengths. In particular, the highest rotational and translational velocity ratios, which indicate a more meaningful distinction between patchy and uniform spheres, are obtained for a small particle size of $2a = 500$ nm diameter and a low Debye length of $\kappa^{-1} = 1$ nm.

The radius of the electrostatic zone of influence (ZOI), $R_{\mathrm{ZOI}} \equiv 2\sqrt{\kappa^{-1}a}$, has been introduced in Sec. 1.1 as the lengthscale over which the interaction per unit area is significant, in systems involving particle interactions with patchy collectors.[81,103] The overall character of the interactions is thus determined by the size of the ZOI, which, in turn, is defined as a function of the Debye length κ^{-1} and the particle size a. Differences between trajectories of patchy and uniform spheres are thus expected to

be meaningful for small particles interacting at relatively low Debye lengths, because a smaller ZOI increases the heterogeneous character of the interactions. For the opposite case of large R_{ZOI} values, particle-collector interactions have a more mean-field like character, such that the effect of the heterogeneity is lessened, and a distinction based on the specific heterogeneity location (sphere or collector) is inferred to be much less significant. Results presented in the sections that follow will thus refer to computations performed for a $2a = 500$ nm diameter patchy particle discretized into $N_{\mathrm{p}} = 6489$ elements. Heterogeneous collectors are discretized using a grid consisting of 45 square elements that represent a length of $2a = 500$ nm, such that the length of each square element is ≈ 11 nm.

4.5.1 Collection probability.

Collection probability curves are computed to distinguish further the behavior of the patchy particle and patchy collector systems. Collection probabilities are defined as the ratio of adhered particles (successes) to the total number of simulated particle trajectories (trials).[74] Computations of a large, statistically significant number of particle trajectories are necessary due to the random distribution of heterogeneity on the patchy surfaces, which are either planar or spherical. The collection probability estimate is obtained, as in Sec. 3.2.4, from

$$\hat{\eta} = \frac{N_{\mathrm{D}}}{N_{\mathrm{total}}} \tag{4.7}$$

where N_{D} is the number of particles deposited on the collector and N_{total} is the total number of particle trajectories simulated.

To obtain more statistically relevant predictions, Wilson score intervals[121] that include the *actual* values of the collection probability are constructed based on the estimates given by Eq. (4.7), and following the steps described in Sec. 3.3.3. Collection probability curves presented in Fig. 4.7 are obtained as series of intervals

computed from Eq. (3.22) with a 95% confidence interval ($\alpha = 0.05$), such that $z_{1-\alpha/2} = 1.96$. The sample size is $n = N_{\text{total}}$ and the probability estimate $\hat{p} = \hat{\eta}$ is obtained from Eq. (4.7).

Unlike deposition rate curves, the collection probability curves presented in Fig. 4.7 do not contain any rate information, since they do not depend on the specific location on the collector at which the particle adheres nor on the required computational time. In similar computational studies performed on the basis of the random sequential adsorption (RSA) model described in Sec. 1.1, the particle adsorption kinetics is characterized by plots of the absorbed particle coverage as a function of a dimensionless adsorption time that depends on the adhering particle size and the number of simulated adhesion attempts.[6,8] The RSA approach is thus most relevant when a significant fraction of the surface is covered by adhered particles. Experimental work[71,72,81,103] involving heterogeneous collectors with nanoscale patches has been focused on adhesion thresholds and initial deposition rates (when the fraction of the collector covered by adhered particles is negligible). In the present study, particle trajectories were thus computed sequentially for collectors with no adhered particles. Particle adhesion is determined by its translation and rotation in shear flow subject to the computed DLVO interactions with the heterogeneous surfaces. The collection probability estimate given by Eq. (4.7) is the ratio of successful adhesion attempts to the total number of attempts, and resembles the available surface function (ASF), defined as the normalized particle adsorption probability in the limit $\mathrm{N}_{\text{attempts}} \to \infty$.[8]

In Fig. 4.7, collection probability curves are presented for patchy particles and patchy collectors at Debye lengths $\kappa^{-1} = 2, 4$ nm. The total number of particle trajectories simulated for each point on this plot is $N_{\text{total}} = 1000$. Each of the trajectories computed for patchy particles was performed for a different heterogeneous particle, in which the patches are randomly distributed on the spherical surface. Alternatively, uniformly charged particles were simulated to flow over distinct heterogeneous collec-

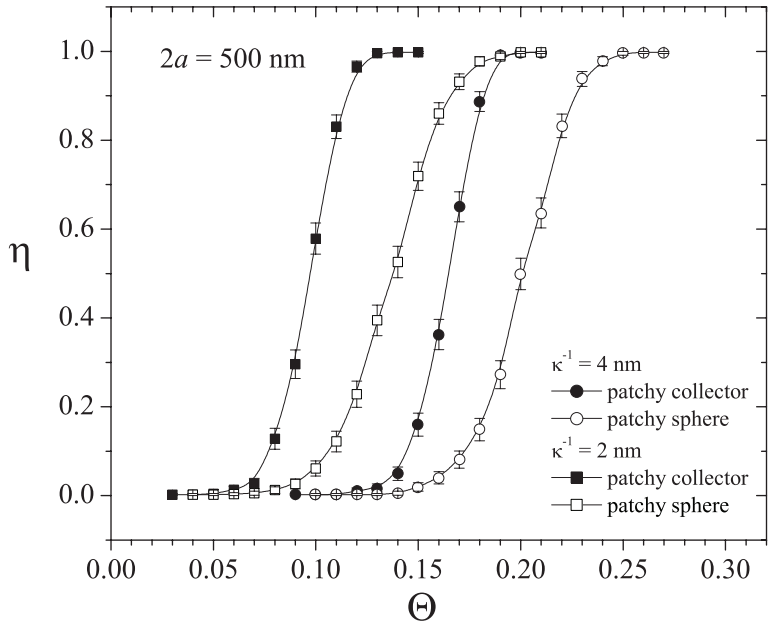

Figure 4.7. Collection probability curves of $2a = 500$ nm diameter, patchy and uniform particles, interacting at Debye lengths $\kappa^{-1} = 2, 4$ nm. Each data point is presented as a Wilson score interval.

tors, each of which was patterned with patches located at randomly chosen locations. Once the sphere or planar surface was discretized into elements with equal area, the algorithm used to choose the location of a patch was identical. For each data point in Fig. 4.7, the number of particles that adhered on the collector was recorded, the respective collection probability estimate $\hat{\eta}$ obtained from Eq. (4.7) and the Wilson score interval computed from Eq. (3.22).

For a given model system and set of parameters, the adhesion threshold is defined as the smallest surface loading for which particles adhere on the collector ($\Theta_c = \min(\Theta) : \eta > 0$). Such thresholds are readily determined from the collection probability curves. It is seen in Fig. 4.7 that adhesion thresholds increase with increasing Debye length for both the patchy and the uniform spheres. At larger Debye lengths, the larger ZOI determines a stronger mean-field character of the interactions, because surface nano-features are effectively smeared over a greater area

of the collector. Thus, at larger Debye lengths, the increasing repulsive character of the interactions leads to larger adhesion thresholds.

Interestingly, the adhesion thresholds for patchy spheres are larger than those of the uniform spheres at both Debye lengths. The higher threshold for the patchy sphere is attributed to its decreased tendency to contact and adhere on the uniform collector, with respect to the uniform sphere flowing over the patchy collector. The lessened adhesive behavior of the patchy particle is due to its larger effective residence time per patch with respect to that of the uniform particle, as described in detail in Sec. 4.5.3.

It is also noted that, with respect to the uniform sphere collection probability curves, those of the patchy particles have, at both Debye lenghts, a larger spread $\Delta\Theta = \Theta_{\mathrm{L}} - \Theta_{\mathrm{c}}$, where Θ_{L} is defined as the minimum surface loading for which all particles adhere on the collector ($\Theta_{\mathrm{L}} = \min(\Theta) : \hat{\eta} = 1$). The patchy sphere thus presents intermediate adhesive behaviors ($0 < \hat{\eta} < 1$) over a larger range of surface loadings Θ. As described in Sec. 4.5.2, the standard deviation of the number of local extrema in the separation distance is significantly larger for the patchy particles than for the uniform particles; in particular, for larger values of the surface loading at which a larger number of particles adhere on the collector. For heterogeneity distributed on spherical surfaces, particle trajectories for the same system parameters are notably different. For heterogeneous planar surfaces, however, only minor changes are visible in the particle trajectories for a fixed set of system parameters. Adhesion probability curves for patchy particles are thus broader than those for the patchy collector system because as the surface loading increases, so does the number of possibly different trajectories of the patchy particle, which, in turn, translates to an adhesion probability that is less than unity. The patchy particle system therefore reaches an unity adhesion probability at a larger surface loading than that for the patchy collector system.

Alternatively, particle collection probabilities can be defined as the ratio of the number of surface elements that yield attractive interactions to the total number of surface elements. Discrete surface elements are considered to yield attractive interactions if their energy profile does not present an energy barrier, that is, if $U_{MAX} < 0$. Computations are identical to those performed to obtain the energy contour plots presented in Figs. 3.22(b)-(c). As described in Sec. 3.3.3, the DLVO energy-distance profile is computed with the GSI technique by placing the particle's center projection at the center of each element of an heterogeneous collector. Due to interactions with different regions of the heterogeneous surface, a distinct energy-distance profile is obtained at each element of the discretized collector. The number of collector elements for which the energy barrier disappears is divided by the total number of collector elements sampled, to yield a newly defined collection probability that is based on DLVO calculations.

Collection probabilities obtained from the trajectory-based approach described previously are compared in Fig. 4.8 to those computed with the newly defined model that stems from DLVO calculations, for a uniform $2a = 500$ nm diameter particle interacting with a heterogeneous collector at Debye lengths $\kappa^{-1} = 2, 4$ nm. The curves with filled markers are those presented in Fig. 4.7 for the case of a patchy collector.

As shown in Fig. 4.8, the adhesion probability curves based on DLVO calculations are broader than those obtained from particle trajectory computations. Heterogeneous surfaces are characterized by distinct local regions that can be either attractive or repulsive, and the transition between such regions is gradual and smooth, as seen in the energy contour plots presented in Figs. 3.22(b)-(c). The probability that for a given surface element the energy barrier is $U_{MAX} < 0$ thus correlates with the respective probability for the neighboring elements. If a specific element is attractive, it is reasonable to expect that elements located within a certain distance from it will

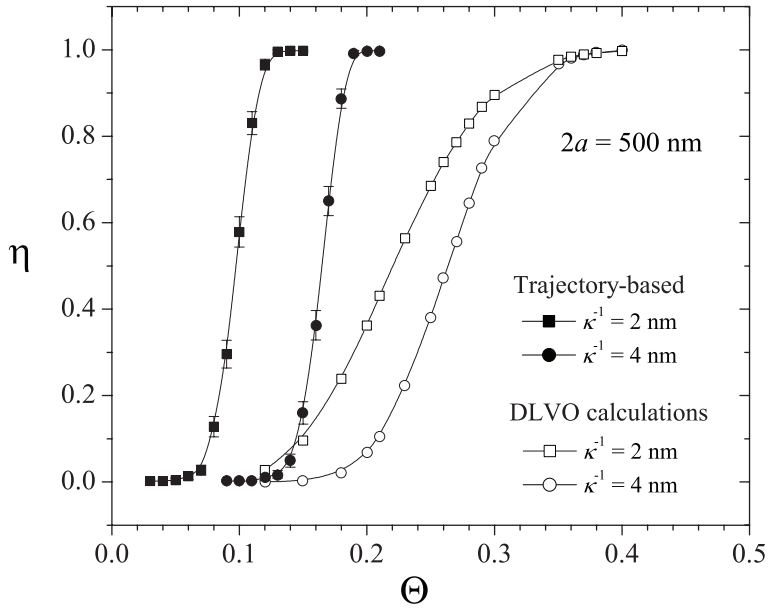

Figure 4.8. Adhesion probability curves based on particle trajectories (filled markers) and DLVO computations (empty markers) for a uniform $2a = 500$ nm diameter particle interacting with patchy collectors at Debye lengths $\kappa^{-1} = 2, 4$ nm.

also be defined as attractive. If, however, an element presents a high energy barrier, it can be assumed that such element belongs to a locally repulsive region, such that closely surrounding elements will also bear a repulsive character. Adhesion probabilities based on trajectory computations define, in contrast, steeper curves. At different simulation attempts, the probability of a particle adhering on a specific heterogeneous collector is uncorrelated to that of a subsequent particle adhering on a different collector. Broader adhesion probability curves obtained from the approach based on DLVO calculations are therefore linked to the probability correlations between surface elements within a locally attractive or repulsive region.

While all trajectory-based probabilities are smaller for the larger Debye length $\kappa^{-1} = 4$ nm, in the case of probabilities defined with DLVO computations, at large surface loadings $\Theta = 0.36 - 0.40$ for which $\eta \to 1$, the computed results for the higher Debye length $\kappa^{-1} = 4$ nm are larger than those obtained for the smaller Debye length

$\kappa^{-1} = 2$ nm. Such "crossing" of the collection probability curves is only minimal, thus not visible in the presented plots, and could be due to computational round off errors. It is reminiscent, however, of the hydrodynamic crossover observed in experiments[37] that is attributed to the shift from heterogeneity-governed interactions at low Debye lengths to mean-field like interactions at high Debye lengths. Adhesion probabilities based on DLVO interactions computed for larger sets of system configurations and parameters could yield a better description of the nature of such crossing.

The parallel-like trajectory-based adhesion probability curves presented for distinct system properties in Figs. 3.14 and 4.7 resemble the cumulative distribution functions (CDFs) of the Poisson distribution, appropriately defined for the heterogeneous systems considered.

In Fig. 4.9, the probability mass function (PMF) of the Poisson distribution obtained from

$$f(k;\lambda) = \frac{\lambda^k\, e^{-\lambda}}{k!}\,, \tag{4.8}$$

is compared to PMF values computed for one specific collector. In Eq. (4.8), k is the number of occurrences and the positive real number λ is the distribution parameter that equals the expected value and the variance of a discrete stochastic variable X. For the heterogeneous systems under consideration, the distribution parameter λ is defined in terms of an arbitrarily chosen collector length L and the surface loading Θ, such that $\lambda = \Theta\, L^2$. The heterogeneous collector is divided into square $L \times L$ regions, and the number of surface features (k) within each region is recorded. The probability $P(X = 15) = 0.02$ indicates, for example, that a region of the collector containing 15 surface heterogeneities can be found with a probability of 2%. The agreement between Poisson PMF values calculated from Eq. 4.8 and those obtained from the collector data is clear, and the distribution of collector heterogeneities indeed follows Poisson statistics. Such agreement, however, would be improved by performing averages over *many* heterogeneous collectors.

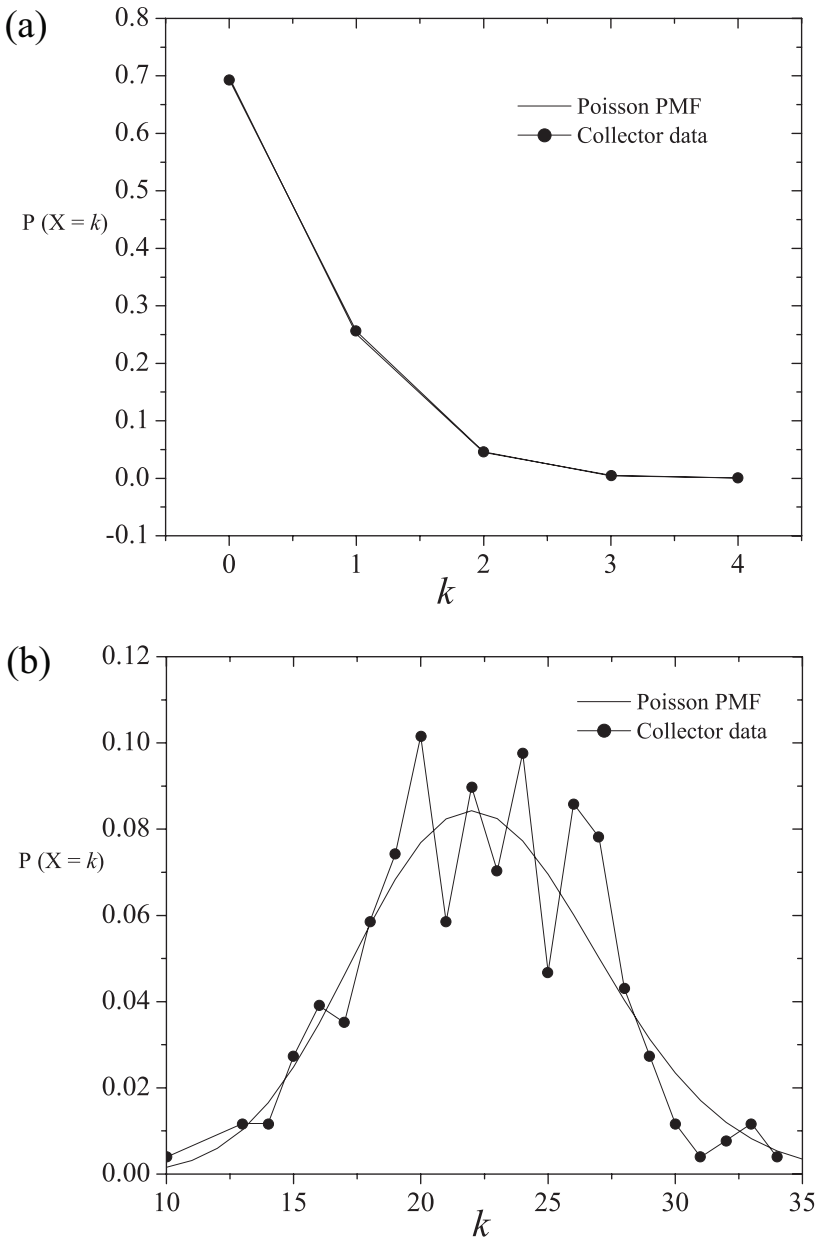

Figure 4.9. Poisson probability mass functions (PMFs) calculated from Eq. (4.8) and obtained with data of one heterogeneous collector for each value of Θ, for varying distribution parameters. (a) $\Theta = 0.01$, $L = 6$ and $\lambda = 0.36$. (b) $\Theta = 0.10$, $L = 15$ and $\lambda = 22.5$.

The cumulative distribution function (CDF) of the Poisson distribution,

$$P(X \leq k) = e^{-\lambda} \sum_{i=0}^{\lfloor k \rfloor} \frac{\lambda^i}{i!} \,, \tag{4.9}$$

is computed for three different values of the surface loading $\Theta = 0.10, 0.15, 0.30$ and presented in Fig. 4.10. For each value of Θ, the parameter L is arbitrarily chosen to yield different values of the distribution parameter λ, each of which determines one CDF curve. As seen in Fig. 4.10, CDF plots at fixed Θ values appear to be parallel. Therefore, such CDF curves could be appropriately scaled to either resemble adhesion probability results presented in Figs. (3.14) and (4.7) or to better model experimental deposition rate curves[37] that are not parallel for varying Debye lengths. The parameter L should depend, for example, on colloidal interaction properties (such as κ^{-1} and A_H).

4.5.2 Number of local extrema in separation distance.

Particle-collector interactions in heterogeneous systems present spatial variations, which are due to the presence of local regions that have a more (or less) attractive character than that predicted by a mean field average of the heterogeneity. The various locally attractive and locally repulsive areas within the heterogeneous surface are clearly identified by the fluctuations observed in particle trajectories, such as those presented in Figs. 4.4 and 4.6.

Trajectories for the patchy particle and patchy collector systems differ in the extent of fluctuations in the particle-collector separation distance. Such differences can be quantified by computing the number of local extrema in the trajectories as a function of the surface loading Θ, for each particle type (patchy or uniform). Due to the inherent random nature of the heterogeneity, the number of extrema for each particle type at each value of Θ is obtained as an average performed over a number of trajectories.

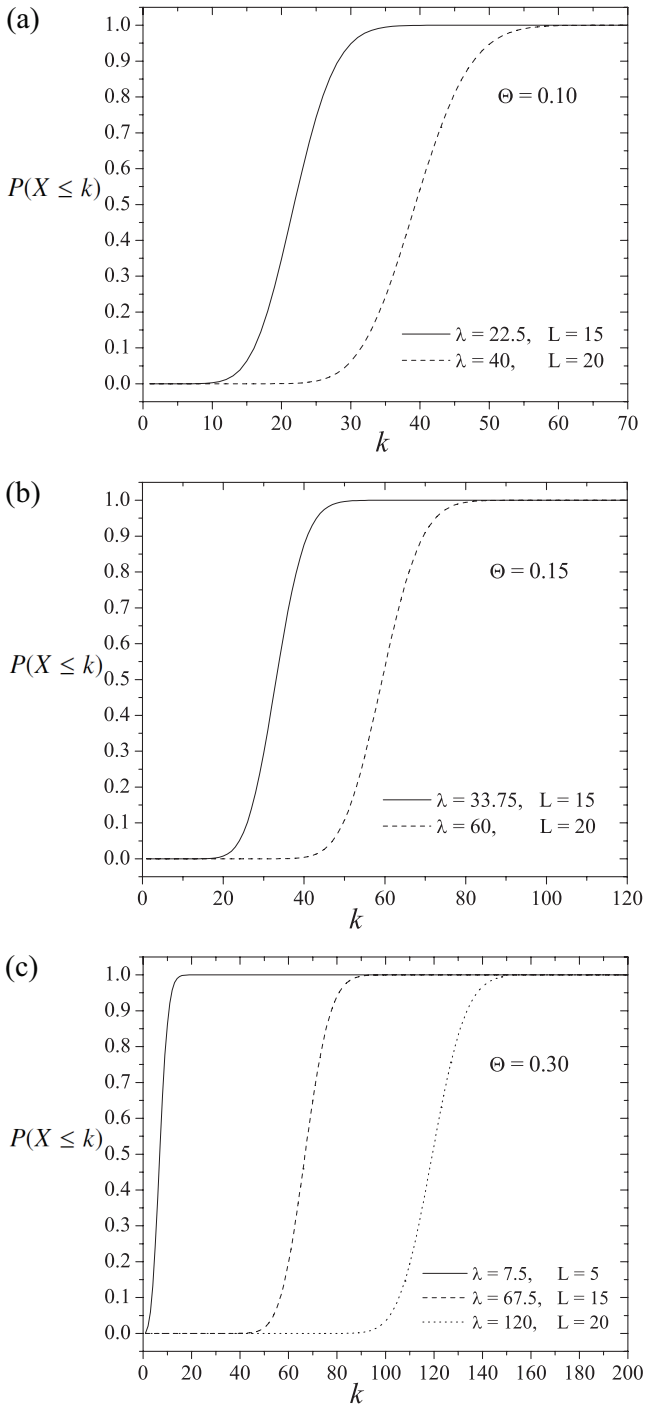

Figure 4.10. Cumulative distribution functions (CDFs) of the Poisson distribution computed with Eq. (4.8) for varying Θ. The parameter L is chosen in each case to yield different values of the distribution parameter λ. (a) $\Theta = 0.10$. (b) $\Theta = 0.15$. (c) $\Theta = 0.30$.

For a fixed value of Θ, the average number of extrema per unit distance in the trajectory of the i-th particle is defined as

$$\overline{N_{\text{ext}\,i}} = \frac{N_i}{y_i} \tag{4.10}$$

where N_i is the number of local extrema observed in the trajectory of particle i and y_i is the horizontal distance (in the plane defined by the collector) between the first and last local extrema.

For N_s trajectories of particles that adhere on the collector, at a fixed surface loading Θ, the average density of extrema is

$$< \overline{N_{\text{ext}}} >_s = \frac{\sum_{i=1}^{i=N_s} \overline{N_{\text{ext}\,i}}}{N_s} \; . \tag{4.11}$$

Similarly, for N_{ns} particles that do not adhere on the collector,

$$< \overline{N_{\text{ext}}} >_{ns} = \frac{\sum_{j=1}^{j=N_{ns}} \overline{N_{\text{ext}\,j}}}{N_{ns}} \; . \tag{4.12}$$

The average density of extrema for a fixed Θ is then obtained as the linear combination

$$< \overline{N_{\text{ext}}} >= p \; < \overline{N_{\text{ext}}} >_s + (1-p) \; < \overline{N_{\text{ext}}} >_{ns} \tag{4.13}$$

where

$$p = \frac{N_D}{N_{\text{total}}} \, , \tag{4.14}$$

N_D is the number of particles deposited on the collector, and $N_{\text{total}} \simeq 200$. Trajectories for which $N_i \leq 1$ were discarded.

The variance of $< \overline{N_{\text{ext}}} >$ is obtained from an error propagation expression derived for Eq. (4.13), assuming that, for the specific case of the trajectories considered in these results, p is a precisely known constant. Thus,

$$\sigma^2_{\text{N}_{\text{ext}}} = p^2 \sigma^2_{\text{N}_{\text{ext, s}}} + (1-p)^2 \sigma^2_{\text{N}_{\text{ext, ns}}} \, . \tag{4.15}$$

For colloidal interactions with $\kappa^{-1} = 4$ nm and $A_H = 5{\times}10^{-21}$ J, the number of extrema is plotted in Fig. 4.11 as a function of the surface loading Θ.

It is seen in Fig. 4.11 for both patchy and uniform particles, that the average number of local extrema remains relatively constant for low values of the surface loading Θ, but increases as the surface loading is further increased. As described in Sec. 4.5, interactions with surface heterogeneity are defined as attractive, regardless of the specific location (spherical or planar) of such heterogeneity. For increasing surface loading, thus, the increasingly stronger attractive interactions decrease the particle-collector separation distance, resulting in a larger number of spatial fluctuations (number of extrema) in the particle trajectories. For both particle types, the average number of extrema starts increasing when the probability of adhesion p (for the particular set of trajectories considered) is $p \simeq 0.37$, occurring at $\Theta \simeq 0.16$ and at $\Theta \simeq 0.20$ for the uniform and patchy particles, respectively. The standard deviation in the number of extrema increases as well, and more significantly than the number of extrema itself, with increasing surface loading Θ. As the number of adhering particles increases, the existence of different adhesion sites on each heterogeneous surface (planar or spherical) multiplies the number of different trajectories that denote particle adhesion, which leads to an increased standard deviation in the number of extrema at larger values of Θ. In particular, the standard deviation increases dramatically when the adhesion probability approaches unity, as seen in Fig. 4.11.

The total number of extrema for the patchy particle is smaller ($N_{\text{tot,p}} \simeq N_{\text{tot,u}}/2$) than that of the uniform particle. As described in detail in Sec. 4.5.3, the larger

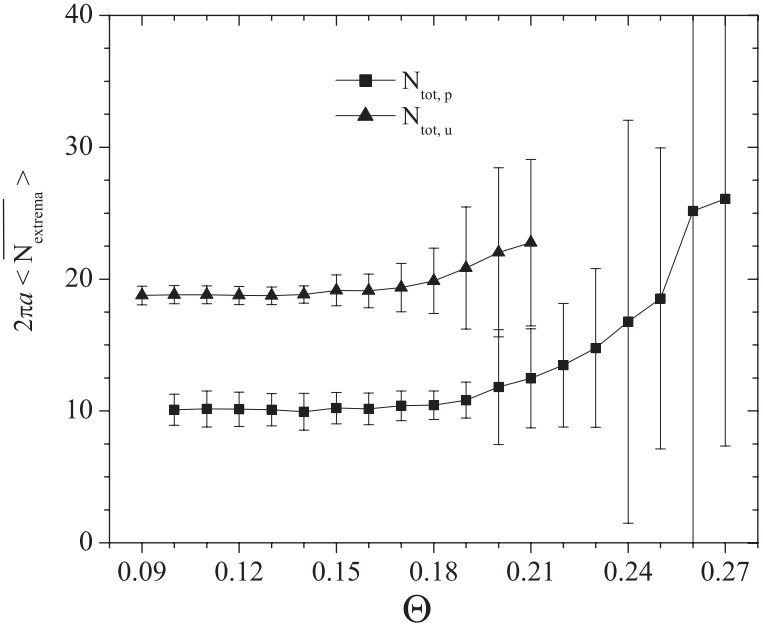

Figure 4.11. Weighted number of extrema as a function of the surface loading, Θ, for patchy and uniform particles and a fixed particle diameter of $2a = 500$ nm averaged over $N_{\mathrm{tot}} \simeq 200$ trajectories.

residence time per patch of the patchy particle partially precludes interactions with other heterogeneity regions, which gives rise to smoother trajectories, or, equivalently, a smaller number of extrema. For each particle type (patchy and uniform), the maximum and minimum number of extrema are also computed and found to be essentially equal, $N_{\mathrm{max,\,p\,(u)}} = N_{\mathrm{min,\,p\,(u)}} = N_{\mathrm{total,\,p\,(u)}}/2$, as expected.

The standard deviation is, however, significantly larger for the patchy particles than for the uniform particles, in particular for larger values of Θ for which a greater number of particles adhere on the collector. The distribution of heterogeneity over a spherical surface yields a broader distribution of trajectories, *i.e.*, trajectories for the same system parameters will be notably different. Heterogeneity distributed over a planar surface, however, does not lead to meaningful differences in particle trajectories, for a fixed set of system parameters, such that the standard deviation

in the number of extrema is expected to be lower than that in the case of the patchy particles.

For the limiting values of the surface loading, that denote an homogeneous repulsive ($\Theta = 0$) or a net-attractive surface (not necessarily entirely covered with heterogeneity, for which $\Theta = 1$), the number of trajectory local extrema is zero. In the case of interactions between two homogeneous equally charged surfaces ($\Theta = 0$), the particle translates without fluctuations at a constant separation distance that corresponds to the secondary minimum in the energy-distance profile. In the case of a net-attractive heterogeneous sphere (collector) interacting with a uniformly charged collector (sphere), the particle trajectory does not present any fluctuations and instead, the separation distance monotonically decreases until the particle contacts the collector at an arbitrarily small separation distance $D = \delta$.

4.5.3 Maximum residence times.

Differences in the trajectories and adhesive behaviors of the systems with patchy particles and patchy collectors can be interpreted based on the effective time period over which one patch influences the electrostatic double layer interaction between a particle and the collector. For simplicity, the maximum residence time is defined as the maximum time a surface element remains in the ZOI. For a patchy collector, this residence time is the time required for the particle to translate a distance of $2R_{\mathrm{ZOI}}$. For a patchy particle, the residence time is the time required for the particle to rotate through the corresponding subtended angle.

A particle in a shear flow in close proximity to a planar surface is shown schematically in Fig. 4.12(a). The particle translates with velocity V_y and rotates at angular velocity Ω_x. For the case in which the heterogeneity is located on the collector, the appropriate maximum residence time depends on the translational velocity V_y, as illustrated in Fig. 4.12(b), and is defined as

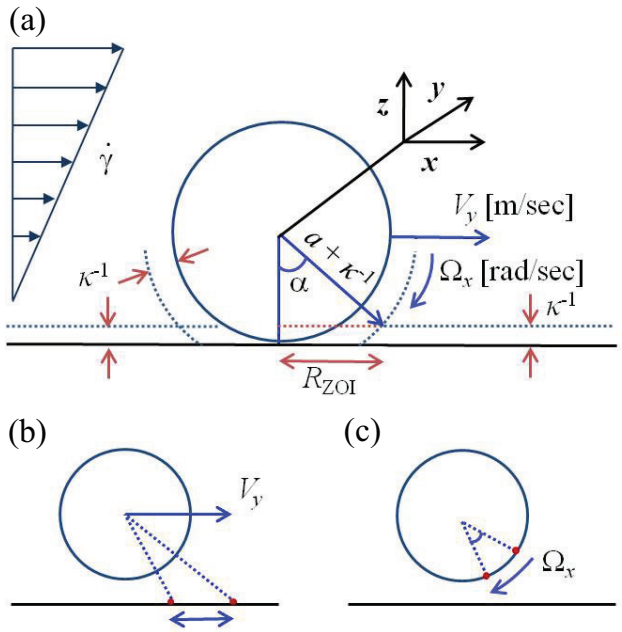

Figure 4.12. (a) Schematic definition of the radius of the Zone of Influence R_{ZOI}. Debye layers of width κ^{-1} around each interacting surface, particle velocities Ω_x and V_y, and the angular displacement α that corresponds to a linear displacement of R_{ZOI}, are also indicated. (b)(c) Schematic diagrams illustrating the appropriate displacements and velocities that define the maximum residence time per (heterogeneous) surface element for patchy collectors and spheres. (b) Linear displacement and linear velocity V_y for the case of a patchy collector. (c) Angular displacement and rotational velocity Ω_x for the case of a patchy particle.

$$\tau_{\rm tr} = \frac{2R_{\rm ZOI}}{V_y}\,. \tag{4.16}$$

If the heterogeneity is located on the spherical surface, as depicted in Fig. 4.12(c), the maximum residence time is a function of the rotational velocity Ω_x,

$$\tau_{\rm rot} = \frac{2\alpha}{\Omega_x}\,, \tag{4.17}$$

where 2α is the angular displacement that corresponds to a linear displacement of $2R_{\rm ZOI}$, and $\sin(\alpha) = R_{\rm ZOI}/(a + \kappa^{-1})$.

The "rotational" residence time defined by Eq. (4.17) is equivalent to a translational residence time for small angular displacements ($\sin(\alpha) \approx \alpha$) defined in terms of an effective translational velocity, $V_y^r \equiv a\Omega_x$,

$$\tau_{\text{rot}} = \frac{2R_{\text{ZOI}}}{(a+\kappa^{-1})\Omega_x} \approx \frac{2R_{\text{ZOI}}}{a\Omega_x} = \frac{2R_{\text{ZOI}}}{V_y^r}\,. \tag{4.18}$$

For particle sizes and Debye lengths frequently chosen in experimental studies, the angular displacements are indeed small. For example, the approximation $\sin(\alpha) \approx \alpha$ presents an error of less than 1% for particle sizes $2a$ = 500 nm - 1 μm and Debye lengths κ^{-1} = 2 - 5 nm. When the particle is not in contact with the collector, it is important to note that $V_y^r < V_y$, as the particle rotates more slowly than it translates.[50,51] It is assumed that the particle rolls without slipping if it contacts the collector, such that $V_y^r = V_y$, as seen in Figs. 4.6(c)-(d). The particle arrests on the collector once the rolling resistance exceeds the shear-induced force and torque, as described in Sec. 4.5.

Computations of maximum residence times are most relevant for particle trajectories at surface loadings for which the adhesion probability is small. Particle trajectories for systems with large surface loadings (either on the spherical or the planar surface) do not exhibit significant segments of particle translation nor rotation, since the strong attraction brings the particles to an immediate arrest, denoted by a short and monotonically decreasing trajectory.

The secondary minimum in the energy-distance profile is chosen as the appropriate separation distance for the computation of the velocities required in Eqs. (4.16)-(4.17) and is computed using the GSI_{UA} technique,[14] described in Sec. 3.1.5. The rotational and translational velocities are obtained from the mobility matrix formulation of the hydrodynamics described in Sec. 2.8, *i.e.*, $\mathbf{U} = \mathbf{MF}$, where $\mathbf{U}$ is the vector of particle velocities, $\mathbf{F}$ is the vector of the externally applied forces and torques, and the 6x6 mobility matrix $\mathbf{M}$ depends on the hydrodynamic functions F_t, F_r, T_t, T_r that model

the fluid's resistance to particle motion. For maximum residence time calculations, the hydrodynamic functions are computed with the functional forms given by Duffadar and Davis,[38] Eqs. (2.46)-(2.49), at a separation distance $h = D_{\text{sec. min.}}$. The particle velocities are given by

$$V_y = \frac{T_r}{6\pi\mu a D_f} F_y - \frac{T_t}{6\pi\mu a^2 D_f} T_x \tag{4.19}$$

and

$$\Omega_x = -\frac{F_r}{8\pi\mu a^2 D_f} F_y + \frac{F_t}{8\pi\mu a^3 D_f} T_x \,, \tag{4.20}$$

where $D_f = T_t\, F_r - F_t\, T_r$, $F_y = F^S$ and $T_x = T^S$ are the shear-induced force and torque, $\dot{\gamma}$ is the shear rate, and $\mu = 1 \times 10^{-3}$ Pa $\cdot$ sec is the water viscosity at $T = 293$ K. The shear force F^S and torque T^S are obtained by rearranging Eq. (2.50), and substituting Eqs. (2.53)-(2.54) in place of the dimensionless correction factors. The velocities given by Eqs. (4.19)-(4.20) are incorporated in Eqs. (4.16)-(4.17) to obtain maximum residence times per element as a function of the surface loading, for varying particle size and Debye length.

For patchy and uniform particles, at varying particle size and Debye length, maximum residence times are plotted in Fig. 4.13 as a function of the surface loading of patches. In all cases, the residence time slightly increases with the surface loading because stronger attractive interactions decrease the particle-collector separation distance, which reduces the particle velocities. Surface loading values considered in residence time calculations are those for which a secondary minimum in the energy-distance profile exists.

For a fixed particle size of $2a = 500$ nm, maximum residence times as a function of surface loading, for both particle types (patchy, uniform), and two Debye lengths $\kappa^{-1} = 2, 4$ nm are presented in Fig. 4.13(a). At a constant Debye length of $\kappa^{-1} = 4$

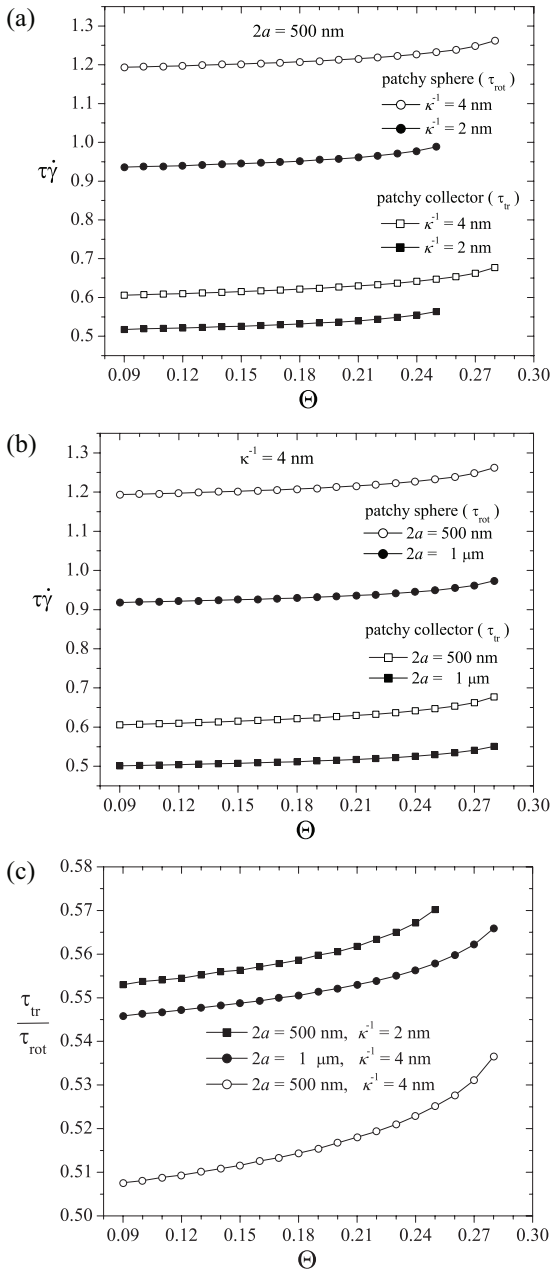

Figure 4.13. Dimensionless maximum residence time per patch vs. surface loading, for patchy and uniform spheres of varying particle sizes and at different Debye lengths. (a) Maximum residence times of patchy and uniform particles, interacting at Debye lengths $\kappa^{-1} = 2, 4$ nm. The particle size is fixed at $2a = 500$ nm diameter. (b) Maximum residence times of patchy and uniform particles, of sizes $2a = 500$ nm and $2a = 1\mu$m diameter. The Debye length is fixed at $\kappa^{-1} = 4$ nm. (c) Ratios of translational to rotational maximum residence times for varying particle sizes and Debye lengths.

nm, the residence times of the patchy particles are significantly larger than those of the uniform spheres (in average, for the presented range of Θ, $\tau_{\text{rot}} \simeq 1.75\,\tau_{\text{tr}}$). The same trend is observed for the lower Debye length $\kappa^{-1} = 2$ nm. The larger residence time per heterogeneous surface element of the patchy particle limits heterogeneous (attractive) interactions, because patchy particles interact with each uniform collector element for longer periods of time. Uniform particles, however, interact with each heterogeneous collector element for shorter periods of time, allowing for an increased number of interactions with multiple patches within the same time period. In agreement with all the results presented in this section, the larger residence time for patches on the particle translates to a smaller number of trajectory fluctuations (number of local extrema), lower adhesion probabilities, and higher adhesion thresholds than those computed for uniform particles flowing over a patchy collector.

For both particle types, it is also shown in Fig. 4.13(a) that, for a fixed particle size, residence times are larger for the larger Debye length. At a constant particle size, a change in the Debye length has two competing effects. An increase in the Debye length corresponds to an increase of $R_{\text{ZOI}} \equiv \sqrt{4\kappa^{-1}a}$, suggesting the maximum residence time should increase at larger values of κ^{-1}. At the same time, however, a larger Debye length moves the secondary minimum farther away from the collector, which increases the particle velocity. At a constant particle size of $2a = 500$ nm, the increase in the size of the ZOI overcomes the increase in the particle velocity, such that the maximum residence times increase with increasing Debye length.

The dependence of the maximum residence time on the surface loading at a constant Debye length of $\kappa^{-1} = 4$ nm is shown in Fig. 4.13(b) for patchy and uniform particles of sizes $2a = 500$ nm and 1 μm. For both particle sizes, the patchy particle residence times are larger than those of the uniform particles because the rotational velocity is significantly smaller than the translational velocity. The effect of particle size on the maximum residence time, at a constant Debye length, is dual, just as the

effect of the Debye length at a constant particle size, previously described. At a fixed Debye length, the larger particle has a larger ZOI, thus, it could be expected that the larger particles will exhibit the larger residence times. It is the smaller particle, however, for which the maximum residence times are larger. The smaller ZOI of the smaller particle defines more localized interactions that also bear a stronger attractive character. Such interactions reduce the flowing particles' velocities, to yield larger maximum residence times.

The ratio of the translational and rotational maximum residence times for the particle sizes and Debye lengths presented in Figs. 4.13(a)-(b) are shown as a function of the surface loading in Fig. 4.13(c). It is readily noted that

$$\frac{\tau_{\rm tr}}{\tau_{\rm rot}} = \frac{2\,R_{\rm ZOI}/V_y}{2\,R_{\rm ZOI}/a\,\Omega_x} = \frac{a\,\Omega_x}{V_y}\,. \tag{4.21}$$

The velocity-, or equivalently, residence time-ratios given by Eq. (4.21) and shown in Fig. 4.13(c) are smaller than 1, and thus indicate that the particle translates faster than it rotates, in agreement with the results presented in Figs. 4.6(c)-(d) for trajectory segments in which the particle does not contact the collector.

In particular, for $2a = 500$ nm patchy and uniform particles interacting with uniform and patchy collectors respectively, at a Debye length $\kappa^{-1} = 4$ nm and surface loading $\Theta = 0.17$, the trajectories and velocity ratios as a function of the horizontal displacement are shown in Figs. 4.14(a)-(b). As seen in Fig. 4.6(b) for interactions at a Debye length $\kappa^{-1} = 5$ nm, the trajectories shown in Fig. 4.14(a) indicate that the uniform particle adheres on the patchy collector, while the patchy particle does not. The average velocity ratio of both particles, computed with Eqs. (4.5)-(4.6) for the trajectory segments between the first and last extrema, is $0.5112 \pm 3.6854 \times 10^{-3}$. This value agrees perfectly with the residence time ratio of 0.5134 presented for the same system parameters ($2a = 500$ nm, $\Theta = 0.17$ and $\kappa^{-1} = 4$ nm) in Fig. 4.13(c).

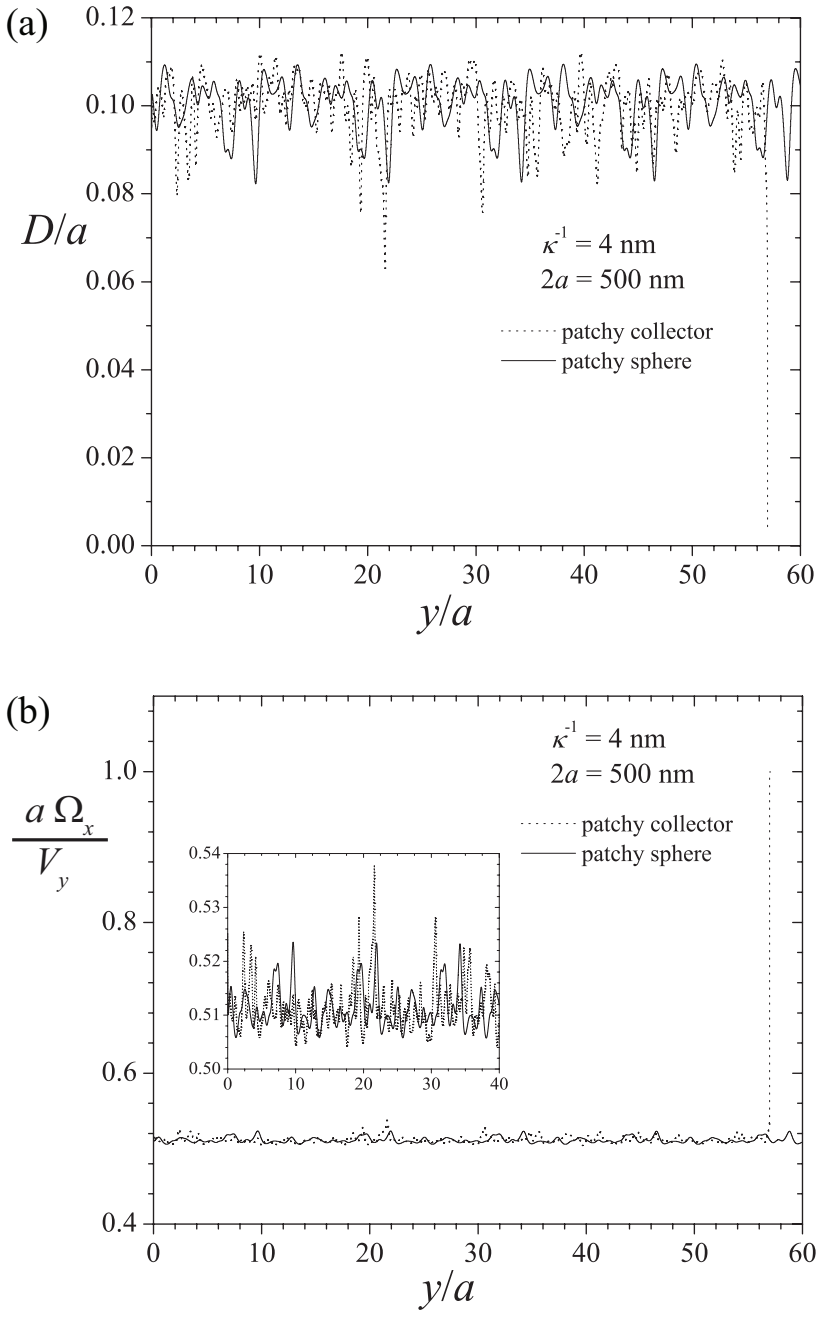

Figure 4.14. Particle trajectories (a) and rotational to translational velocity ratios (b) for patchy particle and patchy collector systems of $2a = 500$ nm particles interacting at a Debye length $\kappa^{-1} = 4$ nm and a surface loading $\Theta = 0.17$.

The ratio of translational to rotational residence times, or, the equivalent angular to translational velocity ratio, given by Eq. (4.21), can be re-written as

$$\frac{a\Omega_x}{V_y} = \frac{(\Omega_x/0.5\dot{\gamma})}{(V_y/h\dot{\gamma})}\,\frac{(a/h)}{2} \tag{4.22}$$

where $\dot{\gamma}$ is the flow shear rate, and $h = D + a$ is the distance between the sphere's center and the flat surface, such that $a/h = [(D/a) + 1]^{-1}$. Following the analysis by Goldman et. al,[51] it is found that

$$\frac{a\Omega_x}{V_y} = \frac{(a/h)}{2}\,\frac{[2(h/a)F^{S*}\,T^t - F^tT^{S*}]}{[(1/2)(a/h)F^rT^{S*} - F^{S*}T^r]}\,. \tag{4.23}$$

The dependence of the angular to translational velocity ratios on the dimensionless separation distance D/a can thus be computed with appropriate sets of expressions that define the hydrodynamic functions F^t, T^t, F^r and T^r, and the dimensionless correction factors of the shear-induced force and torque, F^{S*} and T^{S*}. Velocity ratios computed from two different approaches to the approximation of such functions are compared in Fig. 4.15.

In the first approach, velocity ratios are computed with the asymptotic expressions (2.42)-(2.45) for the hydrodynamic functions and (2.51)-(2.52) for the shear-induced force and torque correction factors, presented by Goldman et al.[50,51] for the limit of large separation distances D/a. The second approach makes use of the functional forms derived by Duffadar and Davis,[38] given by Eqs. (2.46)-(2.49) for the hydrodynamic functions and Eqs. (2.53)-(2.54) for the shear-induced force and torque correction factors. Results obtained from the asymptotic expressions and functional forms are also compared to velocity ratios tabulated by Goldman et al.[50,51] The velocity ratio data is computed, in turn, with tabulated values of the hydrodynamic functions[50] and of the shear force and torque dimensionless factors.[51]

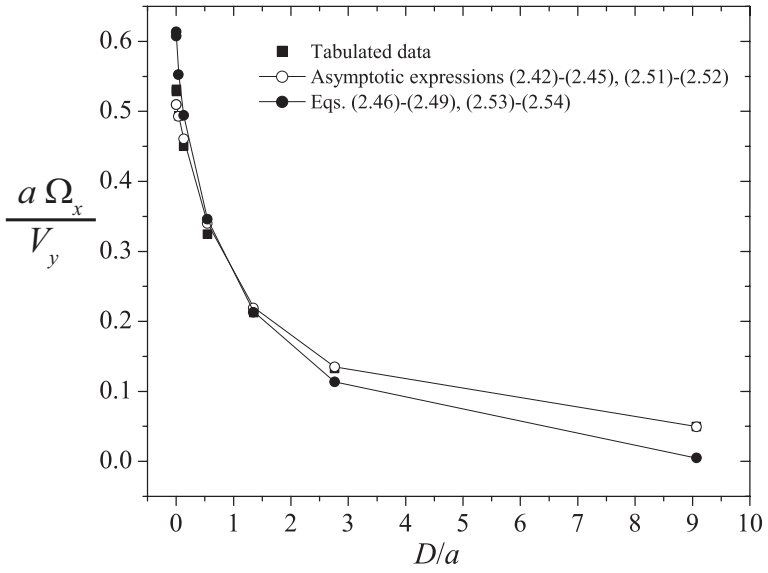

Figure 4.15. Angular to translational velocity ratios as a function of the separation distance D/a computed by Eq. (4.23) furnished by asymptotic expressions or functional forms that approximate the hydrodynamic functions and the shear-induced force and torque correction factors. Tabulated data calculated by Goldman et al.[50,51] is also presented.

As seen in Fig. 4.15, there is good agreement between results obtained from the asymptotic expressions and the functional forms, which also fit well the tabulated data. Moreover, the agreement is perfect for the range of separation distances $0.003202 < D/a < 1$, which is the most relevant to experiments and to the results presented throughout this work.

Angular to translational velocity ratios shown in Fig. 4.15 decrease for larger separation distances D/a. This result coincides with the increase of the residence time ratio for larger surface loadings Θ, shown in Fig. 4.13(c). As the surface loading increases, the more attractive particle-collector interactions reduce the average separation distance, thus increasing the rotational to translational velocity ratio, or, equivalently, the translational to rotational residence time ratio.

The larger maximum residence times per heterogeneity element obtained for patchy particles, at varying Debye lengths and particle sizes, thus leads to their lessened ad-

hesive behavior with respect to that of the uniform particles, as suggested by all the results presented in Sec. 4.5. For both particle types, however, the residence times increase with increasing Debye length at a fixed particle size, and decrease with increasing particle size at a fixed Debye length. Ratios of translational to rotational maximum residence times smaller than 1 indicate that the particle translates faster than it rotates. Such ratios also increase in all cases with surface loading, due to the increase of the respective times with increasing surface loading. Translational to rotational residence time ratios are found to be equivalent to angular to translational velocity ratios, which decrease for larger separation distances. The increase of residence time ratios with surface loading parallels the decrease of the velocity ratios for larger separation distances because stronger attractive interactions draw the particles closer to the collector.

4.5.4 Adhesion regime diagrams.

The dependence of adhesion thresholds for each type of particle on the Debye length can be presented in adhesion regime diagrams that delineate regions in the parameter space in which particle adhesion, defined as irreversible particle arrest, can or cannot be expected. Fig. 4.16 presents adhesion/no adhesion regimes for the patchy and uniform sphere systems considered, for a particle size of $2a = 500$ nm diameter. As expected from the results presented in previous sections, adhesion thresholds are consistently higher for patchy particles than for uniform ones, such that the adhesion regime of the patchy sphere is smaller than that of the uniform sphere.

The differences in thresholds are noticeable at intermediate Debye lengths. At a high Debye length of $\kappa^{-1} = 10$ nm, computations within this work revealed an equal threshold of $\Theta_c = 0.19$ for both particle types. Due to a larger ZOI, the heterogeneity is smeared over a larger (planar or spherical) area and the interactions bear a more

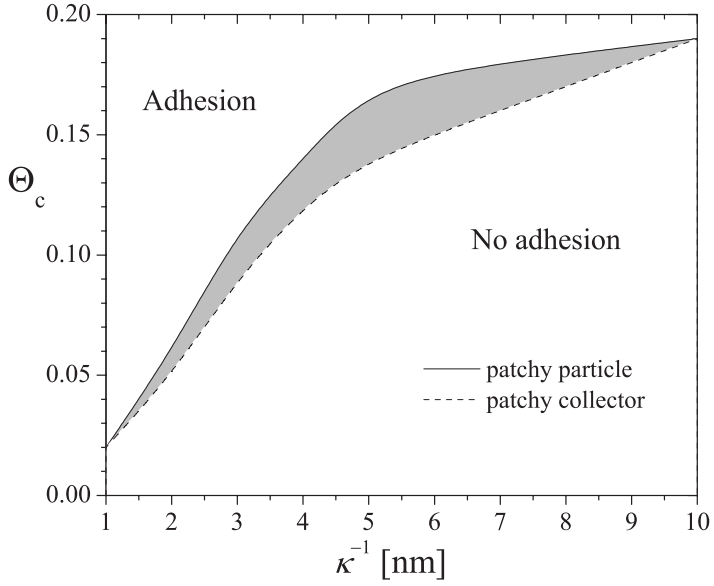

Figure 4.16. Adhesion regime diagram, presented as the dependence of the adhesion thresholds Θ_c on the Debye length κ^{-1}, for $2a = 500$ nm diameter, patchy and uniform particles. For patchy particle and patchy collector systems, the 'Adhesion' and 'No adhesion' regimes are located above and below solid and dashed lines, respectively.

mean-field like character, irrespective of their specific location on the collector or sphere. At a low Debye length of $\kappa^{-1} = 1$ nm, the computed thresholds for patchy particle and patchy collector systems also coincide, and are equal to $\Theta_c = 0.02$. The strongly localized double-layer interactions are significant only over a small area defined by a small ZOI, such that, as in the case of large Debye lengths, the total interactions are not sensitive to the specific location, spherical or planar, of the surface heterogeneities.

It is interesting to note that each of the 'adhesion' and 'no adhesion' regimes can be subdivided to account for rolling/skipping motions and thus distinguish between 4 typical dynamic behaviors, given by the adhesion/no adhesion and surface contact/no surface contact possible combinations. Particles of $2a = 500$ nm diameter, with a Debye length of 5 nm (upper lines in Fig. 4.6(b)) are examples of particles that do not contact the collector and do not adhere on the surface (patchy sphere) and that do

not contact the collector but do adhere on the surface (uniform sphere). Alternatively, at a low Debye length of 1 nm, small patchy and uniform spheres contact the collector and adhere on it (lower lines in Fig. 4.6(b)), while large particles contact the collector but without adhering (lower lines in Fig. 4.6(a)).

4.6 Conclusion.

Particle-collector systems with one heterogeneous surface, which is either the spherical particle or the flat collector, are characterized in detail for different system geometries and a range of varying parameters including particle size, Debye length and electrostatic potentials. DLVO interactions are computed by implementing the GSI technique, and incorporated in a mobility matrix formulation of the dynamics problem that yields particle trajectories as it translates in shear flow above a flat collector.

The patchy collector system, thoroughly studied in previous work, does not require spherical surfaces to be discretized into areal surface elements. To model interactions of systems that include heterogeneous particles, however, the inclusion of such a discretization scheme in the computational model is, in fact, essential. The recursive zonal EQual area Sphere Partitioning (EQSP) algorithm is introduced as an accurate technique that yields the discretization of spherical surfaces into small, equal-area elements. DLVO interactions for patchy particle systems are thus modeled by incorporating EQSP-generated spherical surface elements within the GSI technique. The system's dynamic behavior is also obtained in this case from mobility matrix computations.

Differences in the adhesive and dynamic behaviors of particle-collector heterogeneous systems, in which only *one* surface is patterned with nanoscale features, are quantified by computations of adhesion thresholds and of average numbers of trajec-

tory local extrema. Maximum residence times per heterogeneous surface element are also defined for patchy particles and for patchy collectors.

The lessened tendency of the patchy particle to adhere on a uniform collector, with respect to that of the uniform particle adhering on a patchy collector, is attributed to larger maximum residence times per element for the patchy particle. A larger residence time per element precludes multiple interactions with many heterogeneous surface elements in a given time period, which translates into fewer attractive interactions. Moreover, larger residence times reduce the amount of spatial fluctuations exhibited by patchy particles interacting with uniform collectors, and leads to a smaller number of trajectory local extrema, as shown in the results presented in this chapter. Trajectory spatial variations, in turn, correlate with the extent of interactions with heterogeneous surface elements, and ultimately provides insight into the adhesive character of the system for a given set of parameters. Adhesion thresholds of patchy particles are, indeed, larger than those of uniform particles adhering on patchy collectors.

A new computational approach, that introduces a discretization scheme of spherical surfaces incorporated within GSI computations of DLVO interactions, has been applied to the computation of patchy particle trajectories. The use of this newly developed simulation technique can be extended, for instance, to model particle-collector systems of *two* heterogeneous surfaces, which more accurately represent experimental systems.

CHAPTER 5

CONCLUSIONS AND FUTURE WORK

5.1 Conclusion.

Physical and biological phenomena that are interesting from a practical and theoretical point of view are controlled by particle-collector interactions. Some examples include colloidal adsorption in separation, filtration, coating and cleaning applications, receptor-mediated processes, such as the adhesion and rolling of neutrophils on ligand-coated surfaces, and the development of micro and nano-sensors for "lock and key" devices. A detailed analysis of DLVO interactions and dynamic behaviors of heterogeneous particle-collector systems can also provide a better understanding of the physics underlying such mechanisms, and address questions related to experimental deposition rates that are higher than expected from a classical treatment of the DLVO theory, or, to the specific influence of DLVO interactions on the shear-induced motion of a colloidal sphere above a collector with nanoscale heterogeneity.

Theoretical background on the nature and properties of electrostatic double layer and van der Waals interactions and on the DLVO theory of colloid stability is presented in Chap. 2. Numerical approximation techniques, such as the Derjaguin approximation and the SEI and GSI techniques, developed to approximate DLVO interactions for a number of system configurations, are also described. In particular, the method of choice for all DLVO force and energy computations throughout this work is the GSI technique, that defines the total particle-collector interaction as the result of a pairwise summation of interactions between differential elements on each

surface. A mobility matrix formulation of the hydrodynamic problem, which yields particle velocities required to calculate particle trajectories, is introduced as well.

Systems comprised of smooth uniform particles and topographically and electrostatically heterogeneous collectors are studied in Chap. 3.

In Sec. 3.1, particle interactions with collectors patterned with topographical heterogeneities, modeled as cylindrical pillars, are computed with the GSI technique, previously applied to the computation of interactions with flat collectors only. The versatility of the GSI technique is also illustrated by modeling collectors with chemical and topographical heterogeneity, such as surfaces patterned with pillars *and* patches that are assigned distinct chemical properties. Due to interactions with attractive nano-topography, the potential energy barrier toward particle deposition is found to decrease significantly, even for nano-pillars that protrude a few nanometers from the flat surface.

As well, a novel force- and energy- averaging model is introduced as a simple method to compute the net interaction between a particle and a heterogeneous patchy collector. This technique requires the computation of interactions with two homogeneous surfaces, each of which is uniformly charged. One homogeneous collector bears the electrostatic potential of the patches, while the other is charged with the potential of the underlying surface. It is noted that particle interactions with each homogeneous surface is not restricted to the GSI technique, and instead, such computations could be obtained from SEI computations or Derjaguin approximation predictions. The total particle-patchy collector interactions are then obtained by scaling the homogeneous interactions with the surface loading of patches. Net interactions predicted by the force- and energy-averaging technique are more attractive than expected from a mean-field approach based on an average surface potential, which parallels the zeta potential measured in particle deposition experiments and introduced in many theoretical models. Discrepancies between theoretical predictions and experimental

deposition rates, usually higher than expected, could thus be attributed to the averaging of the heterogeneous surface electrostatic potential. To obtain more attractive interactions, interactions with attractive and repulsive homogeneous surfaces could be averaged instead.

The energy-averaging technique developed in Sec. 3.1 is extended in Sec. 3.2 to define a statistical model that predicts the mean and variance of particle DLVO interactions with heterogeneous collectors. Such predictions are in complete agreement with calculations obtained by performing averages over many randomly heterogeneous patchy and pillared collectors. The statistical model also allows for the computation of adhesion thresholds, defined as the minimum surface loading of patches at which particles begin to adhere from flowing solution. Adhesion thresholds calculated with the computationally inexpensive statistical model coincide with results obtained by simulating large numbers of particle trajectories. Moreover, the statistical technique accurately predicts the increase in the adhesion threshold with the shear rate of the flowing suspension observed in experiments.

In Sec. 3.3, Brownian motion effects on the dynamics of colloidal particles flowing over patchy and pillared collectors are studied by introducing Brownian displacements in particle trajectory calculations.

Brownian motion is expected to be meaningful only for particle-collector systems characterized by a relatively low energy barrier in the energy-distance profile. Energy-distance profiles of large particles interacting with patchy and pillared collectors are shown to be governed by high energy barriers that preclude particle deposition. Inversely, small particles are strongly attracted to pillared collectors, and interactions are dominated by DLVO energies and not by Brownian motion. Small particles interacting with patchy collectors, however, present intermediate, relatively low energy barriers, such that Brownian motion effects are studied in detail for these systems.

It is shown that the addition of Brownian displacements to the particle trajectories introduces significant spatial variations.

A Péclet number that quantifies the relative importance of shear and Brownian effects is also defined, and found to decrease exponentially with particle size. At the low flow shear rates considered, Brownian motion effects are significant only for small particles, with radii of up to $a \simeq 200$ nm. Péclet numbers that evaluate Brownian with respect to colloidal effects calculated for varying particle sizes and for surface loadings for which the average interactions are repulsive, also decrease exponentially with particle size and are smaller than unity for all the parameter ranges considered.

It is thus concluded that Brownian motion has a negligible influence on particle trajectories over collectors patterned with nano-scale heterogeneity, because the non-uniform distribution of such heterogeneity creates locally attractive and repulsive areas within the collector. High energy barriers in strong locally repulsive areas cannot be overcome by Brownian motion, while interactions with strong locally attractive regions are also DLVO-dominated due to the presence of low energy barriers. For small particles in low shear rate flows, Brownian motion effects can be comparable to those of the shear flow. The overall adhesive behavior of the system, however, remains unaffected by the introduction of Brownian effects in the simulations.

In Chap. 4, interactions between patchy particles and collectors are described in detail and a thorough comparison with the extensively studied particle-patchy collector system is presented.

The spherical surface of the patchy particle is discretized into differential elements with the recursive zonal EQual area Sphere Partitioning (EQSP) algorithm, introduced as an accurate technique that yields the partitioning of spherical surfaces into small, equal-area elements. DLVO interactions for patchy particle systems are modeled by incorporating EQSP-generated spherical surface elements within the GSI

technique. The system's dynamic behavior is also obtained in this case from mobility matrix computations.

Differences in the adhesive and dynamic behaviors of patchy particle and patchy collector systems are quantified by computations of adhesion thresholds and of average numbers of trajectory local extrema. For each system, maximum residence times per heterogeneous surface element are also defined. The tendency of the patchy particle to adhere on a uniform collector is found to be smaller than that of the uniform particle adhering on a patchy collector, and attributed to the larger residence time per patch for the patchy particle. Such larger residence times also reduce the amount of spatial fluctuations exhibited by patchy particles and lead to a smaller number of trajectory local extrema. Trajectory spatial variations, in turn, correlate with the extent of interactions with heterogeneous surface elements, and ultimately provide insight into the adhesive character of the system. Adhesion thresholds of patchy particles are, indeed, larger than those of uniform particles adhering on patchy collectors.

A new computational approach, that introduces a discretization scheme of spherical surfaces incorporated within GSI computations of DLVO interactions, has been applied to the computation of patchy particle trajectories. The use of this newly developed simulation technique can be extended, as described in Sec. 5.2, to model particle-collector systems of *two* heterogeneous surfaces, which more accurately represent experimental systems.

5.2 Future Work.

5.2.1 Interactions between heterogeneous particles and heterogeneous collectors.

5.2.1.1 Preliminary results: Discretization of both interacting surfaces and identification of contact areas.

To model more realistic particle-collector systems, heterogeneities should be included in the modeling of both the particle and the collector surfaces. The discretization into differential areal elements of both interacting surfaces is thus required in the simulations, as is the respective synchronization between such partitioning schemes. Chap. 3 described interactions with patchy or pillared collectors, such that in that case it was only the planar or pillared collecting surface that was discretized into differential areal elements. In Chap. 4, inversely, the systems primarily described involved patchy particles, such that in those cases only the spherical surfaces were partitioned into equal-area nano-elements. In this subsection, it is briefly shown that both discretization schemes, planar and spherical, can be seamlessly integrated into a single computational approach that yields the dynamic interactions between heterogeneous particles and collectors.

As a test case, preliminary results of simulations that integrate two discretization schemes into one computational approach are presented for the case of a patchy particle flowing over a uniform flat collector. In particular, the trajectory studied in detail is that of a $2a = 500$ nm diameter particle, patterned with cationic patches at a surface loading of $\Theta = 0.17$, that flows over a uniform flat collector. Colloidal interactions are defined by the Debye length $\kappa^{-1} = 1$ nm and the Hamaker constant $A_H = 5 \times 10^{-21}$ J. These system parameters and particle trajectory correspond exactly to those presented in Sec. 4.5, in the inset in Fig. 4.6(b).

In Fig. 5.1, the particle trajectory is obtained with an integrated computational method that combines discretization schemes for both interacting surfaces. The dis-

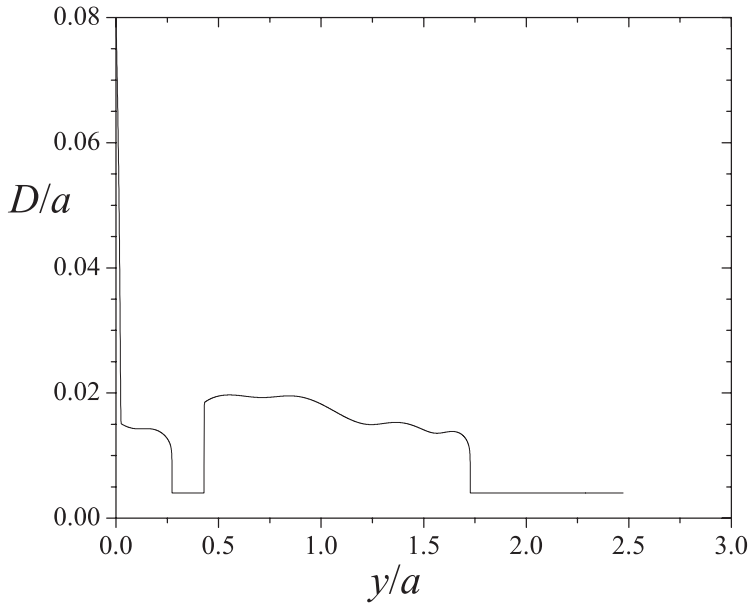

Figure 5.1. Trajectory of a $2a = 500$ nm diameter patchy particle flowing over a uniform flat collector. The particle heterogeneity is defined by the surface loading $\Theta = 0.17$, and other simulation parameters are: $\dot{\gamma} = 25$ sec^{-1}, $\kappa^{-1} = 1$ nm, $A_H = 5 \times 10^{-21}$ J. Compare with the trajectory indicated by the solid line in the inset of Fig. 4.6(b).

cretized collector is, however, electrostatically and topographically homogeneous, such that all the differential areal elements that conform its surface are assigned the same properties. It is clearly seen, by comparison of the trajectories presented in Fig. 5.1 and in the inset of Fig. 4.6 that both computational approaches are in perfect agreement, as expected.

Discretization of both interacting surfaces permits, moreover, to identify the regions in each surface that come into contact, or, at an arbitrarily chosen separation distance. For the test case chosen, the differential elements of the patchy sphere that reach a local separation distance from the planar collector $h < 5$ nm are shown in Fig. 5.2 for a selected times during the simulation. At time $t = 0$ sec, no sphere regions are in proximity to the collector. As the simulation progresses, however, the different areas of the spherical surface for which $h < 5$ nm increase with time, as indicated by

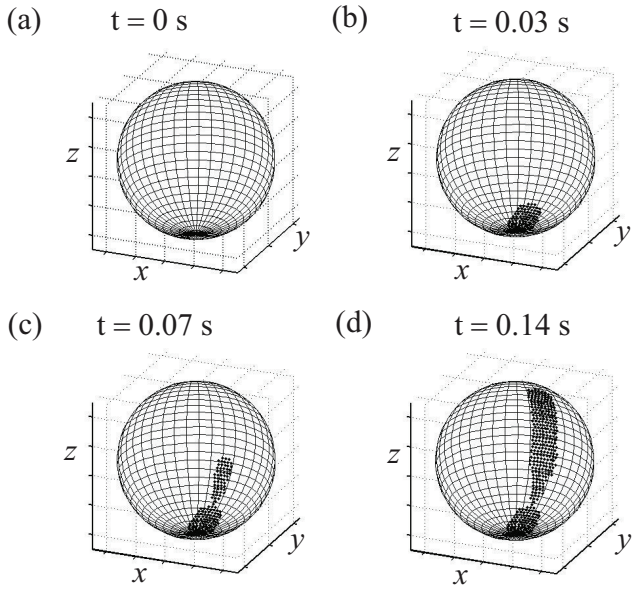

Figure 5.2. Differential elements on the spherical surface that reach a local separation distance from the planar collector $h < 5$ nm, at various times during the simulation. (a) Initial condition of the sphere, $t = 0$ sec. (b) $t = 0.03$ sec. (c) $t = 0.07$ sec. (d) Final position of the sphere, $t = 0.14$ sec.

the increasingly larger quantity of black dots in Figs. 5.2(b)-(d). The time step in the simulations is $dt = 2{\times}10^{-5}$ sec.

The regions of the patchy sphere that at any given simulated time-step reach a local separation distance $h < 5$ nm are also color-scaled according to the frequency in which each surface element meets such "approach" condition.

In Fig. 5.3(a), dark red areas denote spherical regions that approach the collector most frequently (at a local separation distance $h < 5$ nm), while dark blue areas indicate regions that are in close proximity to the collector the least frequently. The increasing frequency of approaches is thus indicated by the continuous progression of the figure colors from dark blue, to light blue, green, yellow, and red. Another representation of the spherical "approach" areas is shown in Fig. 5.3(b). The spherical elements for which at any given time $h < 5$ nm are marked in blue, if a cationic patch is not assigned to that location, or in red, in the opposite case in which there is a patch

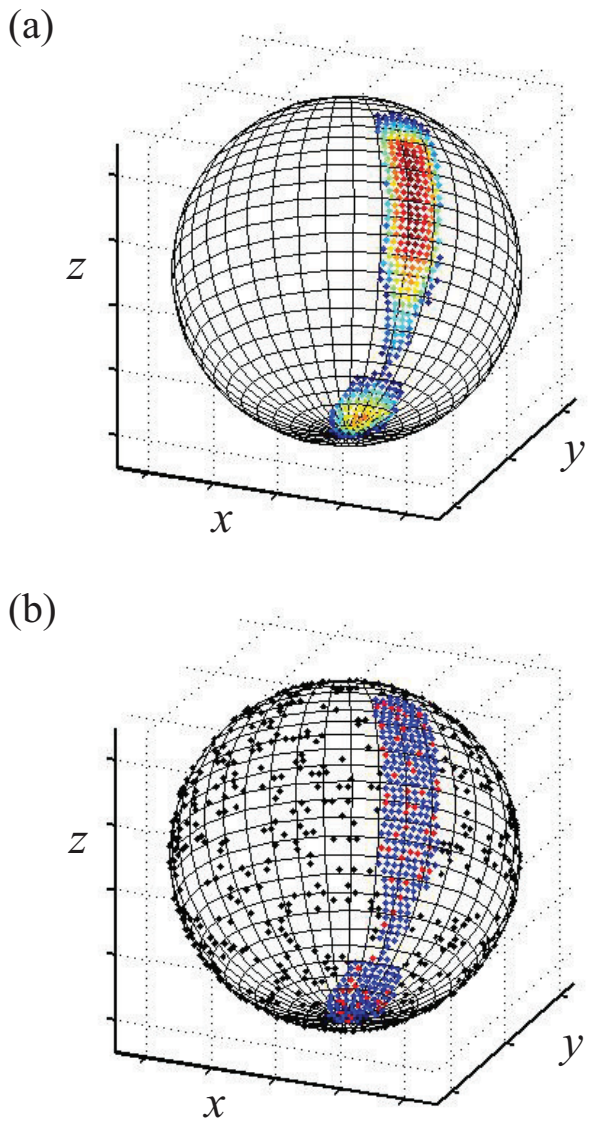

Figure 5.3. (a) A color-scale image of the final position of the sphere, in which the differential elements that reach a local separation distance from the collector $h < 5$ nm are colored based on the frequency of close approach instances. Areas in dark blue denote the least frequently approached regions, and elements for which most frequently $h < 5$ nm are marked in dark red. (b) A colored representation of the sphere-collector close approach regions in which each sphere element is marked in red if a patch is assigned to that sphere element, or, in blue, otherwise. Other sphere elements patterned with heterogeneity, and which do not approach the collector at a separation distance $h < 5$ nm are indicated by black markers.

that patterns such surface element. The black points denote all other cationic patches distributed on the sphere's surface, on areal elements for which the local separation distance at all times is $h > 5$ nm. It is noted that within the closest approach areas only a few surface elements are patterned with cationic patches, which are not isolated, but mostly form small groups of a few units. As mentioned previously, locally favorable regions or "hot spots" can induce attractive interactions that prevail over interactions with surrounding electrostatically repulsive elements.

Projections of the spherical surface on the collector at the same time steps as those featured in Fig. 5.2(a)-(d) are indicated in Fig. 5.4(a) by circles that are progressively centered at larger y/a values, and that are also marked in varying colors. The path that the sphere *draws* on the collector, namely, the projections on the collector of the sphere locations for which $h < 5$ nm at any given time step during the simulation, is marked in black. In Fig. 5.4(b), the sphere's path is color-scaled, such that the highest frequencies of approach instances are marked in yellow and red, while the smallest number of approach opportunities are marked in blue, according to the shown color-scale. The light violet background denotes regions in the collector for which the local separation distance with the sphere is $h > 5$ nm at all simulation time-steps.

The trajectory paths depicted in Figs. 5.2-5.4 is in excellent agreement with the computed trajectory presented in Fig. 5.1. The calculated trajectory in Fig. 5.1 indicates one brief rolling period around $y/a \simeq 0.3$, after which the particle detaches from the surface, before it contacts the surface again (in rolling motion) until it adheres due to friction forces. Both rolling periods, as well as the "detachment" period in between, can be clearly identified in Figs. 5.2-5.4. The horizontal displacement of $y/a \simeq 2.5$ at which the particle is arrested on the collector, as shown in Fig. 5.1, is also seen in Figs. 5.4(a)-(b).

Future work will therefore focus on the further extension of this integrated computational approach to include collector heterogeneities. Though the introduction of

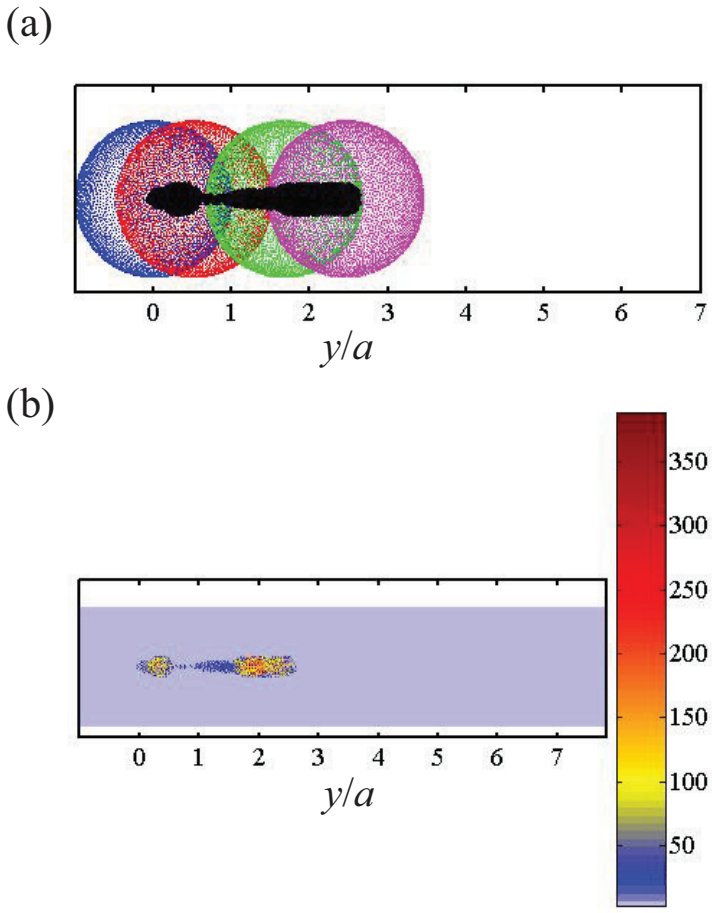

Figure 5.4. (a) Sphere projections on the collector at simulation times $t = 0$ sec (blue circle), $t = 0.03$ sec (red circle), $t = 0.07$ sec (green circle), and $t = 0.14$ sec (pink circle). The sphere's path on the collector's surface, defined by projections of the sphere elements that closely approach the collector, is denoted by the black pattern. (b) A color-scaled image of the sphere's path on the collector's surface, based on the number of instances in which $h < 5$ nm for each sphere element.

collector heterogeneities is relatively simple, the definition of the specific interaction types on a given heterogeneous system might require careful considerations. If each of both interacting surfaces is patterned with only one type of heterogeneity, the system will be characterized by 4 kinds of possible interactions given by the plausible (sphere element)-(collector element) combinations, since each element can be patterned, or not, with a heterogeneity. Each type of interaction can, in turn, be specifically tailored to model different system behaviors.

For example, patches can be chosen to be transferred from the collector to the sphere; namely, if a sphere element contacts a patterned collector element, interactions can be defined such that the sphere "collects" that heterogeneity, removing it from the collector. Alternatively, the collector can be designated as the heterogeneity-removing agent. Cleaning and filtering applications, as well as reversible adsorption processes, could thus be modeled with the proposed integrated computational technique.

Moreover, surface heterogeneities, located at one or both interacting surfaces, can be assumed to be rigid and non-removable. Interactions between them, however, could induce chemical and morphological changes in one or both interacting surfaces, to modify the system's overall behavior. Such computational model would resemble the mechanisms underlying, for instance, lock-and-key devices and protein recognition applications. With appropriate modifications, the proposed computational technique that includes surface discretization schemes for both interacting surfaces can be adapted to model multiple other systems that rely on interfacial interactions, such as those used in surface scribbing and in soft lithography experiments.

5.2.1.2 Surfaces patterned with multiple types of nano-features.

5.2.1.2.1 Adhesive Dynamic Simulations. Hammer et al.[57] developed Adhesive Dynamic simulations to recreate the entire range of adhesive phenomena of cells. The model generates statistical measures of adhesion, such as mean and variance in

velocity, rate constants for cell attachment and detachment, and the frequency of adhesion. The cell is assumed to behave as a hard sphere, covered by rigid microvilli randomly distributed on the cell's surface. Cell receptors, modeled as springs, are also randomly distributed on the cell's surface and on the tips of the microvilli. The microvilli are much longer than the cell receptors, such that only those receptors located on the microvilli tips will yield meaningful contributions to the total cell-substrate interactions.

The formation and breakage of cell to surface bonds is assumed to be a reversible stochastic chemical process,[33] in which the forward and reverse reaction rates depend on the separation distance between the microvillus tip and the ligand-coated substrate, the bond length, spring constants and the thermal energy. Probabilities for bond formation and breakage are obtained from the respective reaction rate expressions, and at each simulated time step, bond formation or breakage is established from the comparison of the corresponding probability with a pseudo-random number.

All the bond-induced forces and torques acting on the cell, along with the hydrodynamic and colloidal forces, are computed at each time step and the translational and rotational velocities of the cell are calculated using the mobility tensor approach[21,50,51,69] previously described.

Adhesive dynamics simulations[57] allowed for the calculation of five distinct types of adhesion behavior. These are: unbound (I), rolling at constant speed (II), tumbling (III), which suggests a largely rolling motion with very brief periods of adhesion, transient adhesion (IV), which suggests significant periods of adhesion during which the cell remains motionless, followed by tumbling or rolling, and adhesion (V), observed sometimes immediately after contact with the surface, and where the cell is motionless for long periods of time.

The method was also extended to the study of different aspects of rolling adhesion, such as the interplay of two receptor systems[16] or the effect of catch bonds.[23]

Recently, Korn and Schwarz[80] developed a new variant of this algorithm, in which the spatial positions of the receptors on the sphere and the ligands on the wall are fully resolved. This model[80] is based on a Langevin equation that accounts for hydrodynamic interactions, thermal fluctuations and adhesive interactions. Also in this case, five different dynamic states of motion of the cell are identified and the transitions between these states are mapped in a dynamic state diagram as a function of the rates for bond formation and rupture.

5.2.1.2.2 Steric interactions and polymer bridging. Aggregation and deposition phenomena can be influenced by attractive or repulsive interactions between adsorbed layers of polymers, that enable bonds with spring-like structures.

Polymers that have some affinity for the surface but adsorb such that some segments of their chains extend from the surface into the surrounding solution are usually referred to as stabilizers, since they form layers that provide the coated surface with stability against aggregation.[41] The close approach of two adsorbed layers results in a strong repulsion between the polymer-coated surfaces, as a consequence of the overlap of the hydrophilic chains. Attractive vdW forces also act between the polymer chains, but their effect is too weak to outweigh the dominant steric repulsion. The thickness of the adsorbed polymer layer with respect to the particle size significantly influences the particle's steric stabilization, such that larger particles would require thicker layers than smaller particles to achieve the same degree of stabilization.

Adsorbed polymer chains can, inversely, enhance particle aggregation and deposition through the formation of polymer bridges. Equally charged particles or surfaces can develop attractive interactions due to bridges formed by long chain polymers that attach to particle surfaces such that the chain is either curled on the surfaces or close to them, instead of extending toward the surrounding medium.[41] In this way, an individual chain can be attached to two or more particles, thus bridging them together. Effective flocculation requires, however, a polymer dosage that is large enough to

allow for the formation of strong bridge-bonds, while at the same time sufficiently low, such that the polymer does not saturate the particle surfaces and allows polymer segments due to the bridging to easily adsorb.

5.2.1.2.3 Colloidal and receptor-ligand particle-surface interactions. The computational technique described in Sec. 5.2.1.1 can be appropriately modified in order to study the dynamic states of particles flowing over surfaces patterned with multiple types of nano-constructs (to parallel biological systems, in which cells have multiple classes of receptors involved in adhesion[43]).

The particles, modeled as rigid spheres, and the heterogeneous substrate or collector can both be patterned not only with flat or protruding electrostatically heterogeneous nano-features, but also with spring-like structures that resemble cellular ligands or receptors, polymer brushes or polyelectrolyte chains. Specific receptor-ligand and long range colloidal interactions between areal elements on each surface can all be incorporated in a mobility matrix approach within the computational model described in Sec. 5.2.1.1 to yield the heterogeneous particle's (cell) velocities as it translates over the heterogeneous collector (substrate).

Receptor-ligand, colloidal, shear and Brownian interactions between particles and collectors could all be ultimately combined in a relatively simple model, to predict not only the energy profile of the system but also its dynamic and adhesive behavior. In theory, this model could also account for the interacting surfaces' and heterogeneities' elasticity. Simulation data contained within adhesive regime diagrams constructed for the systems described could aid in the formulation of lab experiments, as well as in the understanding of the underlying physical processes.

5.2.2 Spatial distribution of adhered particles on collectors. The saturation coverage.

In all previous work, it has been assumed that particles are suspended in dilute solutions, and only one interacting particle is modeled in each energy or trajectory computation. Such particle is subject to DLVO interactions, in the presence or absence of shear flow, due to its proximity to a collector (uniform or heterogeneous) on which no other colloidal particles are previously adhered.

A model that could more realistically resemble the experimental particle deposition process, should include the effects of previously adhered particles. Particle solutions can still be assumed to be dilute, if one particle is released at each simulation attempt. If the particle adheres on the collector, however, it should not be removed, and instead, the adhered particle can be modeled just as a spherical asperity that patterns the collector. In each following simulation attempt, interactions are thus computed between the flowing particle and the newly patterned collector, that is covered not only by nano-scale features but also by previously adhered colloidal particles. Total energies and forces of interactions are comprised, therefore, of attractive and repulsive interactions between the flowing particle and the surface elements of the heterogeneous collector, and, as well, of repulsive interactions between the flowing particle and those adhered on the collector. Sphere-sphere DLVO interactions between adhered particles on the collector can also be computed, for example, by implementing the GSI technique or from an analytical expression, and added to the flowing particle-collector interactions to obtain the total DLVO force or energy of the system.

Ultimately, it will be interesting to gain insight into the distribution of the adhered particles on the collector and to determine the saturation coverage (by adhered particles) beyond which no more newly released particles will deposit on the collec-

tor. The continuous adhesion of particles on the initially bare collector will eventually hinder, or block, particle adhesion in the following simulated attempts.

Particle deposition morphologies have been previously studied with the statistically-based Random Sequential Adsorption (RSA) model, in which the adhesion of randomly sampled particles is based, solely, on whether or not such particle contacts the collection site without overlapping with previously adhered particles. If the arrest conditions are met, the particle is considered to be irreversibly adhered, and the computations proceed with new adhesion attempts. The computational approach presented in this section thus resembles the RSA technique. In the proposed model, however, particle deposition is determined by DLVO interactions and by the system's dynamic behavior in shear flow, and not by random sampling of particles' locations.

In contrast to collection or adhesion probabilities presented in Chaps. 3-4, collection efficiencies could also be defined on the basis of deposited particle distributions for given sets of system parameters. Newly defined collection efficiencies can, in turn, possibly translate into particle deposition rates that are typically measured in experiments.

5.2.3 Lateral Forces.

In particle-collector systems with nano-scale heterogeneity described in this work, the effect of lateral forces was not included in the simulations. The random distribution of the surface features, which are small with respect to the electrostatic zone of influence (ZOI), suggest that lateral forces are not significant. If, moreover, the particles translate in shear flow, the lateral forces' effect is diminished even further because the heterogeneity is sampled more evenly.

Lateral forces could have a meaningful effect, however, if the modeled system is characterized by clearly defined heterogeneous regions, such as stripes, patches that are comparable in size to the interacting particle, or other types of surface features

arranged in an ordered fashion. Interactions at the edges of those distinct regions will most likely be driven by lateral forces, in particular under conditions of no net flow.

Kemps and Bhattacharjee[73] calculated lateral forces acting on a nano-particle located at fixed separation distances from a heterogeneous collector that was modeled as an array of much smaller spherical subunits. The total DLVO particle-collector interaction was computed as the sum of the interactions between the nano-particle and each of the subunits that comprised the collector. Each of this pairwise (nano-sphere)-(spherical subunit) interaction was obtained from analytical expressions derived for sphere-sphere system geometries. The total DLVO energy of interaction was then differentiated with respect to each coordinate, in a cartesian coordinate system, to obtain the respective forces in each direction, namely, F_x, F_y, and F_z. The lateral force was defined as $F_L = \sqrt{F_x^2 + F_y^2}$, where x and y are the coordinates that define the plane of the substrate (and z is the coordinate orthogonal to them). The computation of DLVO interactions with analytical expressions derived for sphere-sphere systems poses some limitations on the model's validity, since those interactions are based on centre-to-centre separation distances between the spheres. The spherical subunits, however, protrude by a distance equal to its radius above the point at which the interactions are computed. As has been extensively shown in previous and current work, even a relatively small asperity protruding only slightly above the collector can have a meaningful effect on the overall energy profile of the system, by reducing, for example, the height of the energy barrier.

Alternatively, Czarnecki[30] calculated tangential forces resulting from surface roughness by numerically differentiating the system's total energy of interaction. A number of small spheres of randomly chosen radii were positioned at randomly selected locations on a smooth flat surface. A larger spherical particle is placed above such collector and the total DLVO energy of the system is obtained as the sum of the sphere-sphere interactions between the large particle and the small spheres that pattern the collec-

tor. Sphere-sphere interactions are computed with analytical expressions that depend on the centre-to centre separation distance. Sphere-plate interactions, in the collector regions in between the spherical asperities, were neglected, because the analytical expressions for this case only describe interactions in the normal direction and do not depend on the coordinate tangential to the collector. Along a line parallel to the collector, the large particle was moved in small distance intervals and the total energy of interaction of the system was computed at multiple points along the line. Tangential forces were obtained as the difference of interaction energies at two neighboring points divided by the distance between such points.

A numerical differentiation approach similar to that described by Czarnecki,[30] can be developed for the particle-collector systems described within this work, in which both interacting surfaces are discretized into differential areal elements. One major limitation of this approach, however, is imposed by the size of the surfaces discrete elements, which would be naturally chosen as the numerical integration step. If the element size is too large, of about 10 nm length, the obtained approximation could be of little or no use. If, instead, a fraction of a surface element is chosen as the integration time step, the resulting numerical scheme could be too cumbersome and impractical.

Another possible approach toward the computation of lateral or tangential forces is based on the GSI technique implemented for two discretized interacting surfaces. For a given differential surface element on the spherical particle, interactions can be computed between that element and each of the collector differential elements. Such computation will then be repeated for all and each spherical surface element. The obtained DLVO forces can then be decomposed into contributions that are parallel and normal to the collector. DLVO forces and energies can be computed, for example, with expressions derived for plate-plate systems, because the most significant interactions are expected for sphere-collector differential elements that are *almost* parallel to each

other. At intermediate lateral separation distances between sphere and collector areal elements, the assumption of parallel plate interactions remains valid, and, at the same time, the magnitude of lateral forces could be found to be meaningful with respect to that of other forces acting on the system.

APPENDIX

BROWNIAN FORCES

An alternative approach to the inclusion of Brownian motion effects on particle trajectory computations consists on introducing *Brownian forces*[24,91] directly in the mobility matrix formulation that yields the particle's velocity. The Brownian forces model appears to have been derived from the definition of a specific Péclet number[24] and not from a strict theoretical basis. Even though the Brownian displacements approach, described in Sec. 3.3, has been more frequently implemented, Brownian motion effects have also been modeled by incorporating Brownian forces.[24,91]

In this Appendix, trajectories of particles flowing over heterogeneous collectors are computed by incorporating *Brownian forces*, and a brief comparison of results obtained with the *Brownian displacements* model is also presented.

Brownian forces in the normal and flow directions are computed from the same stochastic expression[91] presented in Sec. 3.2.2 (Eq. (3.6)),

$$F_{\mathrm{Br}} = \frac{k_{\mathrm{B}}T}{a}\,\hat{\eta}\ ,$$

where k_{B} is the Boltzmann constant, $T = 298.15K$ is the absolute temperature, and $\hat{\eta}$ is a random number of the normal standard distribution. These forces are incorporated directly in the appropriate components of the force vector within the mobility matrix computations, such that

$$F_x = F_{\mathrm{shear}} + F_{\mathrm{Br}_x} \ \text{ and } \ F_y = F_{\mathrm{DLVO}} + F_{\mathrm{Br}_y}\ , \tag{A.1}$$

where F_{Br_x} and F_{Br_y} are the Brownian forces in the flow and normal directions respectively, computed from Eq. (3.6) with different random numbers for each direction. The last term in the rhs in Eq. (3.16) is, therefore, $\mathbf{R}_{\mathrm{Br}} = 0$.

Trajectories of particles flowing heterogeneous patchy or pillared collectors patterned with a surface charge of $\Theta = 0.12$ are shown in Fig. A.1. The computations are performed by either neglecting Brownian motion effects or by incorporating them as *Brownian forces*. It is seen that, in all cases, depicted for large and small particles interacting with patchy and pillared collectors, the Brownian forces model yields trajectories that are almost indistinguishable from those obtained when Brownian effects are not included in the computational results.

To investigate further the effects of Brownian forces on particle motion over nanoscale heterogeneous collectors, and in order to parallel the results presented in Sec. 3.3, a histogram of the horizontal displacements of adhering particles is presented in Fig. A.2. In contrast to respective results predicted with the Brownian displacements approach (shown in Fig. 3.23), computations that include Brownian forces predict that the adhering particles will be all located within the same local "hot spot" in the collector. The locations of adhered particles obtained by modeling Brownian effects as Brownian forces follow a normal distribution, with an average of $x/a = 394.54$ and variance $\sigma^2 = 0.37$.

For the present case of Brownian motion effects modeled as Brownian forces, a new Péclet number that quantifies the relative importance of Brownian and shear forces is defined as

$$\mathrm{Pe}_{(\mathrm{B/S}),\,\mathrm{BrF}} = F_{\mathrm{Br}}/F_{\mathrm{shear}}, \tag{A.2}$$

where F_{Br} is computed from Eq. (3.6) and F_{shear} is given by the general form in Eq. (2.50) with the dimensionless correction factor given by Eq. (2.53).

Péclet numbers $\mathrm{Pe}_{\mathrm{B/S}}$ defined for both the Brownian forces and Brownian displacements models are shown as a function of particle size in Fig. A.3. Péclet numbers

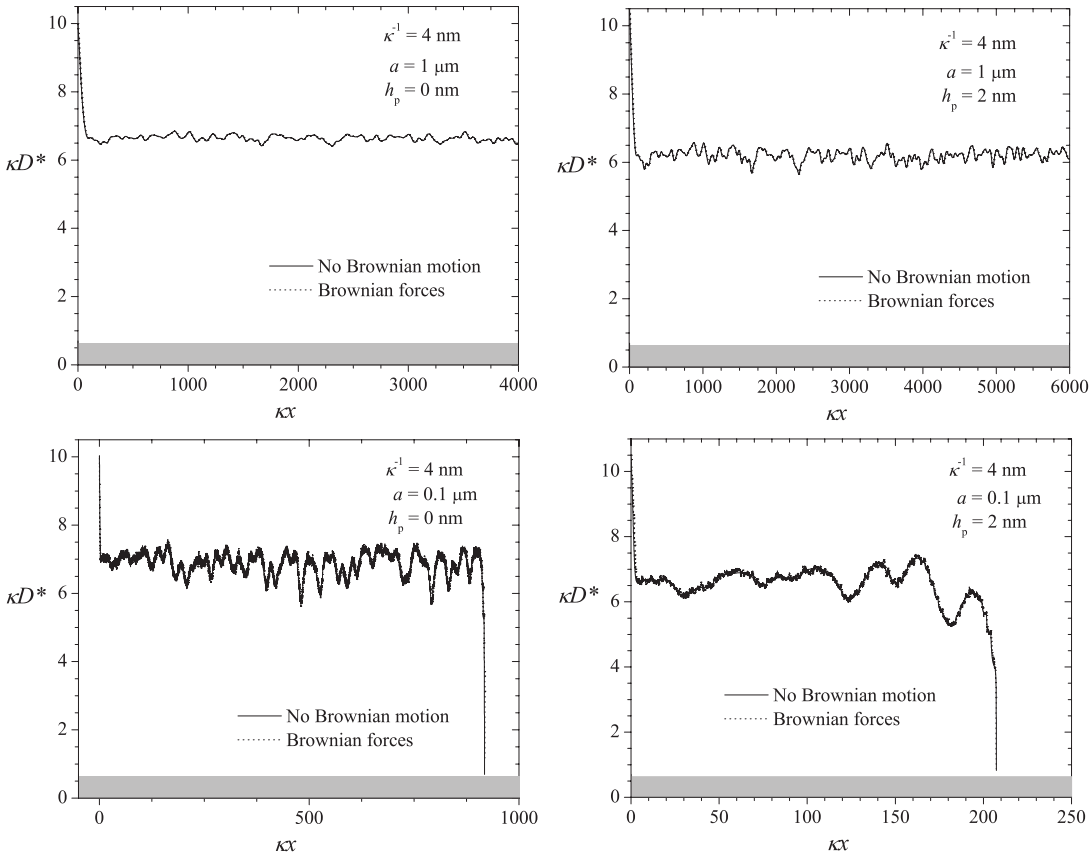

Figure A.1. Trajectories of particles interacting in shear flow with surfaces patterned with randomly located flat patches or cylindrical pillars with a surface area coverage of $\Theta = 0.12$. Other simulation parameters are the same as those in Fig. 3.21. In each plot, trajectories are obtained by either neglecting Brownian motion effects or by incorporating them in the computations as Brownian forces. (a) $a = 1\,\mu$m particles interacting with patchy surfaces ($h_p = 0$ nm). (b) $a = 1\,\mu$m particles interacting with pillared surfaces ($h_p = 2$ nm). (c) $a = 0.1\,\mu$m particles interacting with patchy surfaces ($h_p = 0$ nm). (d) $a = 0.1\,\mu$m particles interacting with pillared surfaces ($h_p = 2$ nm).

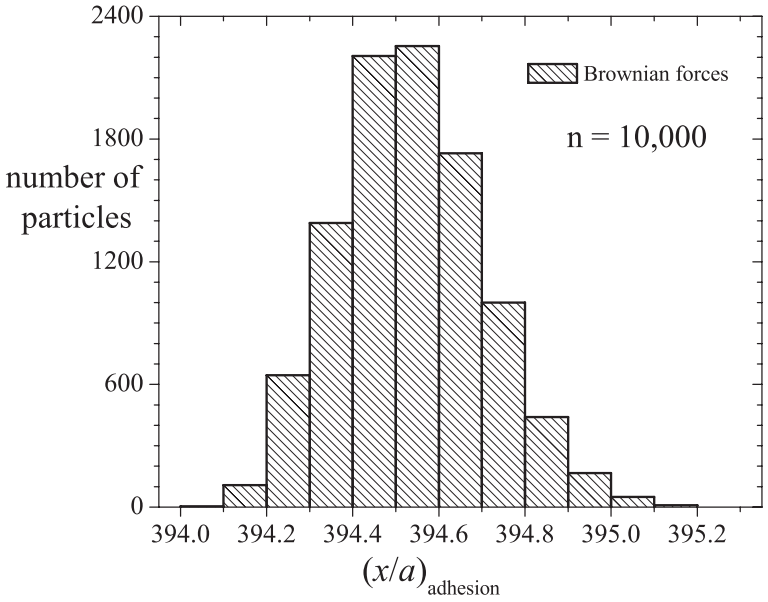

Figure A.2. Statistical distribution of the locations of adhered particles obtained from simulations of particle trajectories in which Brownian motion is computed as Brownian forces, for a collector patterned with a heterogeneity coverage of $\Theta = 0.15$. Other simulation parameters are the same as in Fig. 3.23.

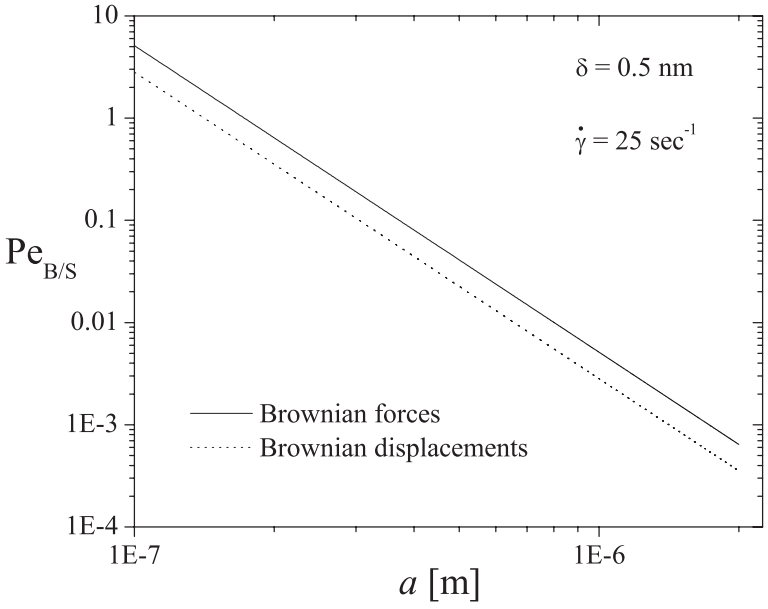

Figure A.3. $Pe_{B/S}$ numbers, defined for the Brownian forces and Brownian displacements models, as a function of the particle size.

obtained for the Brownian forces model were computed by substituting the separation distances $h = D + a$ in Eq. (2.50) and D in Eq. (2.53) with $D = \delta$. No meaningful differences are observed between both Péclet numbers, and, indeed, the Brownian forces model also predicts an exponential decrease of $\mathrm{Pe}_{\mathrm{B/S}}$ with increasing particle size. Computations of Brownian effects modeled as Brownian forces also suggest, therefore, that Brownian motion is significant with respect to shear motion for small particles in low shear flows only.

As seen from the results presented in Figs. A.1-A.3 and in Sec. 3.3, a comparison between the Brownian displacements and Brownian forces models suggests that Brownian displacements predict a slightly greater influence of Brownian motion on the behavior of the systems considered. Brownian displacements are, indeed, incorporated directly in the Langevin-type particle trajectory equation. Brownian forces are introduced, in contrast, in the force vector component of the mobility matrix calculations and their magnitude added to colloidal and shear forces. It is suggested that, for the systems considered, Brownian forces are smaller, possibly by an order of magnitude, than colloidal and/or shear forces, resulting in meaningfully lessened Brownian motion effects.

For a range of system parameters, a detailed quantitative comparison of the various forces acting on particles flowing over nanoscale heterogeneous collectors should be performed to investigate further the observed differences between both models. Limiting cases for which both approaches agree perfectly should also be identified to provide a theoretical foundation of the Brownian forces model, such that Brownian forces would parallel the fundamentally-defined, mean squared displacements of a Brownian particle.

BIBLIOGRAPHY

[1] Adamczyk, Z., and de Ven, T. G. M. Van. Deposition of Particles under External Forces in Laminar Flow through Parallel-Plate and Cylindrical Channels. *J. Colloid Interface Sci. 80* (1981), 340–356.

[2] Adamczyk, Z., Jaszczólt, K., Michna, A., Siwek, B., Szyk-Warszyńska, L., and Zembala, M. Irreversible adsorption of particles on heterogeneous surfaces. *Adv. Colloid Interface Sci. 118* (2005), 25–42.

[3] Adamczyk, Z., Nattich, M., and Barbasz, J. Deposition of colloid particles at heterogeneous and patterned surfaces. *Adv. Colloid Interface Sci. 147-148* (2009), 2–17.

[4] Adamczyk, Z., Siwek, B., and Musial, E. Kinetics of Colloid Particle Adsorption at Heterogeneous Surfaces. *Langmuir 17* (2001), 4529–4533.

[5] Adamczyk, Z., Siwek, B., and Szyk, L. Flow-Induced Surface Blocking Effects in Adsorption of Colloid Particles. *J. Colloid. Interface Sci. 174* (1995), 130–141.

[6] Adamczyk, Z., and Weroński, P. Random sequential adsorption on partially covered surfaces. *J. Chem. Phys. 108*, 23 (1998), 9851–9858.

[7] Adamczyk, Z., and Weroński, P. Application of the DLVO theory for particle deposition problems. *Adv. Colloid Interface Sci. 83* (1999), 137–226.

[8] Adamczyk, Z., Weroński, P., and Musial, E. Colloid Particle Adsorption at Random Site (Heterogeneous) Surfaces. *J. Colloid Interface Sci. 248* (2002), 67–75.

[9] Adamczyk, Z., Zembala, M., and Michna, A. Polyelectrolyte adsorption layers studied by streaming potential and particle deposition. *J. Colloid Interface Sci. 303* (2006), 353–364.

[10] Ahmadi, T. S., Wang, Z. L., Green, T. C., Henglein, A., and El-Sayed, M. A. Shape-controlled synthesis of colloidal platinum nanoparticles. *Science 272* (1996), 1924–1926.

[11] Alexeev, A., Uspal, W. E., and Balazs, A. C. Harnessing Janus nanoparticles to create controllable pores in membranes. *ACS Nano 2(6)* (2008), 1117–1122.

[12] Ansell, G. C., and Dickinson, E. Sediment formation by Brownian dynamics simulation: Effect of colloidal and hydrodynamic interactions on the sediment structure. *J. Chem. Phys. 85(7)* (1986), 4079–4086.

[13] Bell, G. M., Levine, S., and McCartney, L. N. Approximate methods of determining the double-layer free energy of interaction between two charged colloidal spheres. *J. Colloid Interface Sci. 33(3)* (1970), 335–359.

[14] Bendersky, M., and Davis, J. M. DLVO interaction of colloidal particles with topographically and chemically heterogeneous surfaces. *J. Colloid Interface Sci. 353* (2011), 87–97.

[15] Bessiere, Y., Fletcher, D. F., and Bacchin, P. Numerical simulation of colloid dead-end filtration: Effect of membrane characteristics and operating conditions on matter accumulation. *J. Membr. Sci. 313* (2008), 52–59.

[16] Bhatia, S. K., King, M. R., and Hammer, D. A. The State Diagram for Cell Adhesion Mediated by Two Receptors. *Biophys. J. 84* (2003).

[17] Bhattacharjee, S., and Elimelech, M. Surface element integration: A novel technique for evaluation of DLVO interaction between a particle and a flat plate. *J. Colloid Interface Sci. 193* (1997), 273–285.

[18] Bhattacharjee, S., Ko, C. H., and Elimelech, M. DLVO interaction between rough surfaces. *Langmuir 14* (1998), 3365–3375.

[19] Blaaderen, Ruel, R., and Wiltzius, P. Template-directed colloidal crystallization. *Nature 385* (1997), 321–324.

[20] Brant, J. A., and Childress, A. E. Membrane-Colloid Interactions: Comparison of Extended DLVO Predictions with AFM Force Measurements. *Environ. Eng. Sci. 19(6)* (2002), 413–427.

[21] Brenner, H. The slow motion of a sphere through a viscous fluid towards a plane surface. *Chem. Eng. Sci. 16* (1961), 242–251.

[22] Brenner, H. The stokes resistance of an arbitrary particle - II: An extension. *Chem. Eng. Sci. 19*, 9 (1964), 599–629.

[23] Caputo, K. E., Lee, D., King, M. R., and Hammer, D. A. Adhesive Dynamics Simulations of the Shear Threshold Effect for Leukocytes. *Biophys. J. 92* (2007).

[24] Carpen, I. C., and Brady, J. F. Microrheology of colloidal dispersions by Brownian dynamics simulations. *J. Rheol. 49(6)* (2005), 1483–1502.

[25] Cayre, O., Paunov, V. N., and Velev, O. D. Fabrication of asymmetrically coated colloid particles by microcontact printing techniques. *J. Mater. Chem. 13* (2003), 2445–2450.

[26] Chang, K, and Hammer, D. A. Influence of Direction and Type of Applied Force on the Detachment of Macromolecularly-Bound Particles from Surfaces. *Langmuir 12(9)* (1996), 2271–2282.

[27] Chapman, D. L. A contribution to the theory of electroencapillarity. *Phil. Mag. 25(6)* (1913), 475–481.

[28] Charrier, A., Candoni, N., and Thibaudau, F. DNA detection method based on the two-dimensional aggregation and selective desorption of nanoparticle probes. *J. Phys. Chem. B 110* (2006), 12896–12900.

[29] Chatterjee, R., Mitra, S. K., and Bhattacharjee, S. Particle deposition onto Janus and patchy spherical collectors. *Langmuir 27* (2011), 8787–8797.

[30] Czarnecki, J. The effects of surface inhomogeneities on the interactions in colloidal systems and colloid stability. *Adv. Colloid Interface Sci. 24* (1986), 283–319.

[31] Dague, E., Duval, J., Jorand, F., Thomas, F., and Gaboriaud, F. Probing surface structures of Shewanella spp. by microelectrophoresis. *Biophys. J. 90* (2006).

[32] Dean, W. R., and O'Neill, M. E. A slow motion of viscous liquid caused by the rotation of a solid sphere. *Mathematika 10*, 1 (1963), 13–24.

[33] Dembo, M., Torney, D. C., Saxman, K., and Hammer, D. The reaction-limited kinetics of membrane-to-surface adhesion and detachment. *Proc. R. Soc. Lond. B 234* (1988), 55–83.

[34] Derjaguin, B. V. Analysis of friction and adhesion, IV. The theory of the adhesion of small particles. *Kolloid Z. 69* (1934), 155–164.

[35] Derjaguin, B. V., and Landau, L. D. Theory of the stability of strongly charged lyophobic sols and of the adhesion of strongly charged particles in solution of electrolytes. *Acta Physicochim. URSS 14* (1941), 733–762.

[36] Drechsler, A., Petong, N., Zhang, J., Kwok, D. Y., and Grundke, K. Force measurements between teflon AF and colloidal silica particles in electrolyte solutions. *Colloids Surf. A 250* (2004), 357–366.

[37] Duffadar, R., Kalasin, S., Davis, J. M., and Santore, M. M. The impact of nanoscale chemical features on micron-scale adhesion: Crossover from heterogeneity-dominated to mean field behavior. *J. Colloid Interface Sci. 337* (2009), 396–407.

[38] Duffadar, R. D., and Davis, J. M. Interaction of micrometer-scale particles with nanotextured surfaces in shear flow. *J. Colloid Interface Sci. 308* (2007), 20–29.

[39] Duffadar, R. D., and Davis, J. M. Dynamic adhesion behavior of micrometer-scale particles flowing over patchy surfaces with nanoscale electrostatic heterogeneity. *J. Colloid Interface Sci. 326* (2008), 18–27.

[40] Elimelech, M., Chen, J. Y., and Kuznar, Z. A. Particle Deposition onto Solid Surfaces with Micropatterned Charge Heterogeneity: The Hydrodynamic Bump Effect. *Langmuir 19* (2003), 6594–6597.

[41] Elimelech, M., Gregory, J., Jia, X., and Williams, R. A. *Particle Deposition and Aggregation: measurement, modelling and simulation*. Colloid and surface engineering series. Butterworth-Heinemann Ltd., 1995.

[42] Elimelech, M., and O'Melia, C. R. Effect of Particle Size on Collision Efficiency in the Deposition of Brownian Particles with Electrostatic Energy Barriers. *Langmuir 6* (1990), 1153–1163.

[43] Eniola, A. O., Willcox, P. J., and Hammer, D. A. Interplay between Rolling and Firm Adhesion Elucidated with a Cell-Free System Engineered with Two Distinct Receptor-Ligand Pairs. *Biophys. J. 85* (2003), 2720–2731.

[44] Ermak, D. L., and McCammon, J. A. Brownian dynamics with hydrodynamic interactions. *J. Chem. Phys. 69* (1978), 1352–1360.

[45] Fantoni, R., Gazzillo, D., Giacometti, A., Miller, M. A., and Pastore, G. Patchy sticky hard spheres: Analytical study and Monte Carlo simulations. *J. Chem. Phys. 127* (2007), 234507.

[46] Faxén, H. Die bewegung einer starren kugel längs der achse eines mit zaher flüsigkeit gefüllten rohres. *Arkiv. Mat. Astron. Fys. 17*, 27 (1923), 1–28.

[47] Forsten, K. E., Kozack, R. E., Lauffenburger, D. A., and Subramaniam, S. Numerical solution of the nonlinear Poisson-Boltzmann equation for a membrane-electrolyte system. *J. Phys. Chem 98* (1994), 5580–5586.

[48] Glotzer, S. C., and Solomon, M. J. Anisotropy of building blocks and their assembly into complex structures. *Nature Mater. 6* (2007), 557–562.

[49] Goldman, A. J. *Investigations in Low Reynolds Number Fluid-Particle Dynamics*. PhD thesis, New York University, 1966.

[50] Goldman, A. J., Cox, R. G., and Brenner, H. Slow viscous motion of a sphere parallel to a plane wall - I Motion through a quiescent fluid. *Chem. Eng. Sci. 22* (1967), 637–651.

[51] Goldman, A. J., Cox, R. G., and Brenner, H. Slow viscous motion of a sphere parallel to a plane wall - II Couette flow. *Chem. Eng. Sci. 22* (1967), 653–660.

[52] Gon, S., Bendersky, M., Ross, J. L., and Santore, M. M. Manipulating Protein Adsorption using a Patchy Protein-Resistant Brush. *Langmuir 26(14)* (2010), 12147–12154.

[53] Gou, L., and Murphy, C. J. Solution-phase synthesis of Cu$_2$O nanocubes. *Nano Lett. 3(2)* (2003), 231–234.

[54] Gouy, G. Sur la constitution de la charge électrique à la surface d'un électrolyte. *J. Phys. Radium 9* (1910), 457–468.

[55] Guggenheim, E. A. The accurate numerical solution of the Poisson-Boltzmann equation. *Trans. Faraday Soc. 55* (1959), 1714–1724.

[56] Hamaker, H. C. The London-van der Waals attraction between spherical particles. *Physica 4* (1937), 1058–1072.

[57] Hammer, D. A., and Apte, S. M. Simulation of cell rolling and adhesion on surfaces in shear flow: general results and analysis of selectin-mediated neutrophil adhesion. *Biophys. J. 63* (1992), 35–57.

[58] Hernandez, C. J., and Mason, T. G. Colloidal alphabet soup: Monodisperse dispersions of shape-designed LithoParticles. *J. Phys. Chem. C. 111(12)* (2007), 4477–4480.

[59] Hoek, E. M. V., and Agarwal, G. K. Extended DLVO interactions between spherical particles and rough surfaces. *J. Colloid Interface Sci. 298* (2006), 50–58.

[60] Hoek, E. M. V., Bhattacharjee, S., and Elimelech, M. Effect of membrane surface roughness on colloid-membrane DLVO interactions. *Langmuir 19* (2003), 4836–4847.

[61] Hogg, R., Healy, T. W., and Fuerstenau, D. W. Mutual coagulation of colloidal dispersions. *Trans. Faraday Soc. 62* (1966), 1638–1651.

[62] Holst, M., Kozack, R. E., Saied, F., and Subramaniam, S. Treatment of electrostatic effects in proteins: Multigrid-based Newton iterative method for solution of the full nonlinear Poisson-Boltzmann equation. *Proteins: Structure, Function, and Bioinformatics 18(3)* (1994), 231–245.

[63] Holst, M. J., and Saied, F. Numerical solution of the nonlinear Poisson-Boltzmann equation: Developing more robust and efficient methods. *Journal of Computational Chemistry 16(3)* (1995), 337–364.

[64] Hull, M., and Kitchener, J. A. Interaction of Spherical Colloidal Particles with Planar Surfaces. *Trans. Faraday Soc. 65* (1969), 3093–3104.

[65] Iacovella, C. R., and Glotzer, S. C. Complex Crystal Structures Formed by the Self-Assembly of Ditethered Nanospheres. *Nano Lett. 9(3)* (2009), 1206–1211.

[66] Israelachvili, J. N. *Intermolecular and Surface Forces: With Applications to Colloidal and Biological Systems.* Academic Press Inc. (London) Ltd., 1985.

[67] Ivanova, E. P., Truong, V. K., Wang, J. Y., Berndt, C. C., Jones, R. B., Yusuf, I. I., Peake, I., Schmidt, H. W., Fluke, C., Barnes, D., and Crawford, R. J. Impact of Nanoscale Roughness of Titanium Thin Film Surfaces on Bacterial Retention. *Langmuir 26(3)* (2010).

[68] Jana, N. R., Gearheart, L., and Murphy, C. J. Wet Chemical Synthesis of High Aspect Ratio Cylindrical Gold Nanorods. *J. Phys. Chem. B 105* (2001), 4065–4067.

[69] Jeffery, G. B. On the steady rotation of a solid of revolution in a viscous fluid. *Proc. Lond. Math. Soc. 14* (1915), 327–338.

[70] Johnson, P. R., Sun, N., and Elimelech, M. Colloid Transport in Geochemically Heterogeneous Porous Media: Modeling and Measurements. *Environ. Sci. Technol. 30* (1996), 3284–3293.

[71] Kalasin, S., and Santore, M. M. Hydrodynamic crossover in dynamic microparticle adhesion on surfaces of controlled nanoscale heterogeneity. *Langmuir 24* (2008), 4435–4438.

[72] Kalasin, S., and Santore, M. M. Sustained Rolling of Microparticles in Shear Flow over an Electrostatically Patchy Surface. *Langmuir 26*, 4 (2010), 2317–2324.

[73] Kemps, J. A. L., and Bhattacharjee, S. Interactions between a Solid Spherical Particle and a Chemically Heterogeneous Planar Substrate. *Langmuir 21* (2005), 11710–11721.

[74] Kemps, J. A. L., and Bhattacharjee, S. Particle Tracking Model for Colloid Transport near Planar Surfaces Covered with Spherical Asperities. *Langmuir 25(12)* (2009), 6887–6897.

[75] King, M. R., Sumagin, R., Green, C. E., and Simon, S. I. Rolling dynamics of a neutrophil with redistributed L-selectin. *Math. Biosci. 194* (2005).

[76] Kokkoli, E., and Zukoski, C. F. Surface Pattern Recognition by a Colloidal Particle. *Langmuir 17* (2001), 369–376.

[77] König, P. M., Roth, R., and Dietrich, S. Lock and key model system. *Europhys. Lett. 84* (2008), 68006.

[78] Koopal, L. K., and Dukhin, S. S. Modelling of the double layer and electrosorption of a patchwise heterogeneous surface on the basis off its homogeneous analogue 1. Non-interacting patches. *Colloids Surf. A 73* (1993), 201–209.

[79] Koopal, L. K., and Van Riemsdijk, W. H. Electrosorption on random and patchwise heterogeneous surfaces: electrical double-layer effects. *J. Colloid Interface Sci. 128*, 1 (1989), 188–200.

[80] Korn, C. B., and Schwarz, U. S. Dynamic states of cells adhering in shear flow: From slipping to rolling. *Phys. Rev. E 77(041904)* (2008).

[81] Kozlova, N., and Santore, M. M. Manipulation of Micrometer-Scale Adhesion by Tuning Nanometer-Scale Surface Features. *Langmuir 22* (2006), 1135–1142.

[82] Leopardi, P. A partition of the unit sphere into regions of equal area and small diameter. *Electronic Transactions on Numerical Analysis 25* (2006), 309–327.

[83] Lifshitz, E. M. Theory of molecular attractive forces. *Soviet Phys. JEPT 2* (1956), 73–83.

[84] Likos, C. N., Blaak, R., and Wynveen, A. Computer simulations of polyelectrolyte stars and brushes. *J. Phys.: Condens. Matter 20* (2008), 494221.

[85] Lin, S., and Wiesner, M. R. Exact Analytical Expressions for the Potential of Electrical Double Layer Interactions for a Sphere-Plate System. *Langmuir 26(22)* (2010), 16638–16641.

[86] Malikova, N., Pastoriza-Santos, I., Schierhorn, M., Kotov, N. A., and Liz-Marzán, L. M. Layer-by-Layer Assembled Mixed Spherical and Planar Gold Nanoparticles: Control of Interparticle Interactions. *Langmuir 18* (2002), 3694–3697.

[87] Marshall, J. K., and Kitchener, J. A. The deposition of colloidal particles on smooth solids. *J. Colloid Interface Sci. 22* (1966), 342–351.

[88] Martines, E., Csaderova, L., Morgan, H., Curtis, A. S. G., and Riehle, M. O. DLVO interaction energy between a sphere and a nano-patterned plate. *Colloids Surf, A. 318* (2008), 45–52.

[89] Maude, A. D. The movement of a sphere in front of a plane at low Reynolds number. *Brit. J. Appl. Phys. 14* (1963), 894–898.

[90] McCartney, L. N., and Levine, S. An improvement on Derjaguin's expression at small potentials for the double layer interaction energy of two spherical colloidal particles. *J. Colloid Interface Sci. 30* (1969), 345–354.

[91] Mody, N. A., and King, M. R. Influence of Brownian Motion on Blood Platelet Flow Behavior and Adhesive Dynamics near a Planar Wall. *Langmuir 23* (2007), 6321–6328.

[92] Nelson, K. E., and Ginn, T. R. Colloid Filtration Theory and the Happel Sphere-in-Cell Model Revisited with Direct Numerical Simulation of Colloids. *Langmuir 21* (2005), 2173–2184.

[93] O'Neill, M. E. A slow motion of viscous liquid caused by a slowly moving solid sphere. *Mathematika 11*, 1 (1964), 67–74.

[94] Pawar, A. B., and Kretzschmar, I. Self-assembly of T-structures in molecular fluids. *J. Phys. Chem. B 111* (2007), 2081–2089.

[95] Pawar, A. B., and Kretzschmar, I. Fabrication, Assembly, and Application of Patchy Particles. *Macromol. Rapid Commun. 31* (2010), 150–168.

[96] Qi, D., Lu, N., Xu, H., Yang, B., Huang, C., Xu, M., Gao, L., Wang, Z., and Chi, L. Simple Approach to Wafer-Scale Self-Cleaning Antireflective Silicon Surfaces. *Langmuir 25* (2009).

[97] Ranade. Adhesion and Removal of Fine Particles on Surfaces. *Aerosol Sci. Technol. 7* (1987), 161–176.

[98] Richmond, P. Electrical Forces between Particles with Discrete Periodic Surface Charge Distributions in Ionic Solution. *J. Chem. Soc., Faraday Trans. II 71* (1975), 1154–1163.

[99] Rolland, J. P., Maynor, B. W., Euliss, L. E., Exner, A. E., Denison, G. M., and DeSimone, J. M. Direct Fabrication and Harvesting of Monodisperse, Shape-Specific Nanobiomaterials. *J. Am. Chem. Soc. 127* (2005), 10096–10100.

[100] Russel, W. B., Saville, D. A., and Schowalter, W. R. *Colloidal Dispersions.* Cambridge University Press, 1989.

[101] Russo, J., Tartaglia, P., and Sciortino, F. Reversible gels of patchy particles: Role of the valence. *J. Chem. Phys. 131* (2009), 014504.

[102] Salerno, M. B., Rothstein, S., Nwachukwu, C., Shelbi, H., Velegol, D., and Logan, B. E. Differences between Chemisorbed and Physisorbed Biomolecules on Particle Deposition to Hydrophobic Surfaces. *Environ. Sci. Technol. 39* (2005), 6371–6377.

[103] Santore, M. M., and Kozlova, N. Micrometer Scale Adhesion on Nanometer-Scale Patchy Surfaces: Adhesion Rates, Adhesion Thresholds, and Curvature-Based Selectivity. *Langmuir 23* (2007), 4782–4791.

[104] Schuhmann, D., and D'Epenoux, B. The Effect of Electrical Nonhomogeneities of Particles on Mean Surface Potential. *J. Colloid Interface Sci. 116* (1987), 159–167.

[105] Sear, R. P. Phase behavior of a simple model of globular proteins. *J. Chem. Phys. 111(10)* (1999), 4800–4806.

[106] Song, L., and Elimelech, M. Transient Deposition of Colloidal Particles in Heterogeneous Porous Media. *J. Colloid Interface Sci. 167* (1994), 301–313.

[107] Song, L., Johnson, P. R., and Elimelech, M. Kinetics of Colloid Deposition onto Heterogeneously Charged Surfaces in Porous Media. *Environ. Sci. Technol. 28* (1994), 1164–1171.

[108] Sun, N., and Walz, J. Y. A Model for Calculating Electrostatic Interactions between Colloidal Particles of Arbitrary Surface Topology. *J. Colloid Interface Sci. 234* (2001), 90–105.

[109] Sun, Y., and Xia, Y. Shape-Controlled Synthesis of Gold and Silver Nanoparticles. *Science 298* (2002), 2176–2179.

[110] Suresh, L., and Walz, J. Y. Effect of Surface Roughness on the Interaction Energy between a Colloidal Sphere and a Flat Plate. *J. Colloid Interface Sci. 183* (1996), 199–213.

[111] Suresh, L., and Walz, J. Y. Direct Measurement of the Effect of Surface Roughness on the Colloidal Forces between a Particle and Flat Plate. *J. Colloid Interface Sci. 196* (1997), 177–190.

[112] Tavares, J. M., Teixeira, P. I. C., and da Gama, M. M. Telo. Criticality of colloids with distinct interaction patches: The limits of linear chains, hyperbranched polymers, and dimers. *Phys. Rev. E 80* (2009), 021506.

[113] Tobiason, J. E. Chemical effects on the deposition of non-Brownian particles. *Colloids Surf. 39*, 1 (1989), 53–75.

[114] Unni, H. N., and Yang, C. Brownian dynamics simulation and experimental study of colloidal particle deposition in a microchannel flow. *J. Colloid Interface Sci. 291* (2005), 28–36.

[115] Velegol, D., Feick, J. D., and Collins, L. R. Electrophoresis of spherical particles with a random distribution of zeta potential or surface charge. *J. Colloid Interface Sci. 230* (2000), 114–121.

[116] Velegol, D., and Thwar, P. K. Analytical model for the effect of surface charge nonuniformity on colloidal interactions. *Langmuir 17* (2001), 7687–7693.

[117] Verwey, E. J. W., and Overbeek, J. T. G. *Theory of the Stability of Lyophobic Colloids*. Elsevier, Amsterdam, 1948.

[118] Walz, J. Y. The effect of surface heterogeneities on colloidal forces. *Adv. Colloid Interface Sci. 74* (1998), 119–168.

[119] Warszyński, P. Coupling of hydrodynamic and electric interactions in adsorption of colloidal particles. *Adv. Colloid Interface Sci. 84* (2000), 47–142.

[120] White, L. R. On the Deryaguin approximation for the interaction of macrobodies. *J. Colloid Interface Sci. 95(1)* (1983), 286–288.

[121] Wilson, E. B. Probable Inference, the Law of Succession, and Statistical Inference. *Journal of the American Statistical Association 22(158)* (1927), 209–212.

[122] Yeh, K, Cho, K, and Chen, L. Preparation of Superhydrophobic Surfaces of Hierarchical Structure of Hybrid from Nanoparticles and Regular Pillar-Like Pattern. *Langmuir DOI: 10.1021/la9015492* (2009).

[123] Yoshida, M., and Lahann, J. Smart Nanomaterials. *ACS Nano 2(6)* (2008), 1101–1107.

[124] Zeng, H., Pesika, N., Tian, Y., Zhao, B., Chen, Y., Tirrell, M., Turner, K. L., and Israelachvili, J. N. Frictional Adhesion of Patterned Surfaces and Implications for Gecko and Biomimetic Systems. *Langmuir 25* (2009).

[125] Zhang, H., Nunes, J. K., Gratton, S. E. A., Herlihy, K. P., Pohlhaus, P. D., and DeSimone, J. M. Fabrication of multiphasic and regio-specifically functionalized PRINT® particles of controlled size and shape. *New J. Phys. 11* (2009), 075018.

[126] Zhang, J., Srivastava, S., Duffadar, R., Davis, J. M., Rotello, V. M., and Santore, M. M. Manipulating Microparticles with Single Surface-Immobilized Nanoparticles. *Langmuir 24* (2008), 6404–6408.

[127] Zhang, Z., and Glotzer, S. C. Self-Assembly of Patchy Particles. *Nano Lett. 4(8)* (2004), 1407–1413.

[128] Zypman, F. R. Exact expressions for colloidal plane-particle interaction forces and energies with applications to atomic force microscopy. *J. Phys.: Condens. Matter 18* (2006).